

Washington University in St. Louis

Washington University Open Scholarship

All Theses and Dissertations (ETDs)

5-24-2012

Adaptive MIMO Radar for Target Detection, Estimation, and Tracking

Sandeep Gogineni

Washington University in St. Louis

Follow this and additional works at: <https://openscholarship.wustl.edu/etd>

Recommended Citation

Gogineni, Sandeep, "Adaptive MIMO Radar for Target Detection, Estimation, and Tracking" (2012). *All Theses and Dissertations (ETDs)*. 692.

<https://openscholarship.wustl.edu/etd/692>

This Dissertation is brought to you for free and open access by Washington University Open Scholarship. It has been accepted for inclusion in All Theses and Dissertations (ETDs) by an authorized administrator of Washington University Open Scholarship. For more information, please contact digital@wumail.wustl.edu.

WASHINGTON UNIVERSITY IN ST. LOUIS

School of Engineering and Applied Science

Preston M. Green Department of Electrical & Systems Engineering

Thesis Examination Committee:

Dr. Arye Nehorai, Chair

Dr. R. Martin Arthur

Dr. Nan Lin

Dr. Hiro Mukai

Dr. Carlos H. Muravchik

Dr. Jung-Tsung Shen

Adaptive MIMO Radar for Target Detection, Estimation, and Tracking

by

Sandeep Gogineni

A dissertation presented to the Graduate School of Arts & Sciences
of Washington University in partial fulfillment of the
requirements for the degree of

DOCTOR OF PHILOSOPHY

May 2012

Saint Louis, Missouri

copyright by
Sandeep Gogineni
2012

ABSTRACT OF THE THESIS

Adaptive MIMO Radar for Target Detection, Estimation, and Tracking

by

Sandeep Gogineni

Doctor of Philosophy in Electrical Engineering

Washington University in St. Louis, 2012

Research Advisor: Dr. Arye Nehorai

We develop and analyze signal processing algorithms to detect, estimate, and track targets using multiple-input multiple-output (MIMO) radar systems. MIMO radar systems have attracted much attention in the recent past due to the additional degrees of freedom they offer. They are commonly used in two different antenna configurations: widely-separated (distributed) and colocated. Distributed MIMO radar exploits spatial diversity by utilizing multiple uncorrelated looks at the target. Colocated MIMO radar systems offer performance improvement by exploiting waveform diversity. Each antenna has the freedom to transmit a waveform that is different from the waveforms of the other transmitters.

First, we propose a radar system that combines the advantages of distributed MIMO radar and fully polarimetric radar. We develop the signal model for this system and analyze the performance of the optimal Neyman-Pearson detector by obtaining approximate expressions for the probabilities of detection and false alarm. Using these

expressions, we adaptively design the transmit waveform polarizations that optimize the target detection performance.

Conventional radar design approaches do not consider the goal of the target itself, which always tries to reduce its detectability. We propose to incorporate this knowledge about the goal of the target while solving the polarimetric MIMO radar design problem by formulating it as a game between the target and the radar design engineer. Unlike conventional methods, this game-theoretic design does not require target parameter estimation from large amounts of training data. Our approach is generic and can be applied to other radar design problems also.

Next, we propose a distributed MIMO radar system that employs monopulse processing, and develop an algorithm for tracking a moving target using this system. We electronically generate two beams at each receiver and use them for computing the local estimates. Later, we efficiently combine the information present in these local estimates, using the instantaneous signal energies at each receiver to keep track of the target.

Finally, we develop multiple-target estimation algorithms for both distributed and colocated MIMO radar by exploiting the inherent sparsity on the delay-Doppler plane. We propose a new performance metric that naturally fits into this multiple target scenario and develop an adaptive optimal energy allocation mechanism. We employ compressive sensing to perform accurate estimation from far fewer samples than the Nyquist rate. For colocated MIMO radar, we transmit frequency-hopping codes to exploit the frequency diversity. We derive an analytical expression for the block coherence measure of the dictionary matrix and design an optimal code matrix using

this expression. Additionally, we also transmit ultra wideband noise waveforms that improve the system resolution and provide a low probability of intercept (LPI).

Acknowledgments

My sincere thanks go to my advisor Dr. Arye Nehorai for his support and guidance which have been immensely helpful throughout my doctoral studies. He has provided me with the opportunity to work on hot research areas that are of great interest to me.

I wish to thank my dissertation committee members Dr. R. Martin Arthur, Dr. Nan Lin, Dr. Hiro Mukai, Dr. Carlos H. Muravchik, and Dr. Jung-Tsung Shen for their insightful comments on my research and suggestions to improve my dissertation.

I am extremely grateful to my family, including my parents, my grandparents, my wife, and my sister for their invaluable love and emotional support. My grandparents Dr. G. Hari Prasad Rao and Dr. D. L. N. Prasad have been a great source of inspiration for me throughout my life. This dissertation is dedicated to them.

Sandeep Gogineni

Washington University in Saint Louis
May 2012

To my grandparents.

Contents

Abstract	ii
Acknowledgments	v
List of Tables	x
List of Figures	xi
1 Introduction	1
1.1 Background	1
1.2 Our Contributions	2
2 Polarimetric MIMO Radar with Distributed Antennas for Target Detection	5
2.1 Introduction	5
2.2 Signal Model	6
2.3 Problem Formulation	11
2.4 Detector	12
2.4.1 Test Statistic	12
2.4.2 Estimation of Covariance Matrices	13
2.4.3 Performance Analysis	13
2.4.4 Optimal Design	17
2.5 Scalar Measurement Model	18
2.6 Numerical Results	20
2.7 Summary	27
3 Game Theoretic Design for Polarimetric MIMO Radar Target Detection	29
3.1 Introduction	29
3.2 Game Theory Background	30
3.3 Polarimetric Design	33
3.3.1 Problem Formulation	33
3.3.2 Solution	39
3.4 Numerical Simulations	40
3.5 Summary	50
4 Monopulse MIMO Radar for Target Tracking	52

4.1	Introduction	52
4.2	System Description	53
4.3	Signal Model	56
4.3.1	Transmitted Waveforms	56
4.3.2	Target and Received Signals	57
4.3.3	Beamforming	59
4.4	Tracking Algorithm	62
4.4.1	Initialization	62
4.4.2	Monopulse Processing: Local Angular Estimates	63
4.4.3	Fusion Center: Global Location Estimate	64
4.4.4	Multiple Targets	67
4.5	Numerical Results	68
4.5.1	Simulated Scenario	68
4.5.2	Spatial Diversity	70
4.5.3	Rapidly Maneuvering Airborne Target	73
4.5.4	Effect of a Jamming Signal	73
4.5.5	Sequential vs Simultaneous Lobing	75
4.5.6	Maneuvering Ground Target	76
4.6	Summary	77
5	Target Estimation Using Sparse Modeling for Distributed MIMO Radar	79
5.1	Introduction	79
5.2	Signal Model	80
5.3	Sparse Support Recovery	86
5.3.1	Basis Pursuit (BP)	86
5.3.2	Block-Matching Pursuit (BMP)	87
5.4	Optimal Adaptive Energy Allocation	89
5.5	Compressive Sensing	93
5.6	Numerical Results	94
5.7	Summary	104
6	Frequency-hopping Code Design for MIMO Radar Estimation Using Sparse Modeling	107
6.1	Introduction	107
6.2	Signal Model	108
6.3	Sparse Representation	112
6.4	Block Coherence Measure	115
6.5	Optimal Hopping-Frequency Design	116
6.5.1	Problem Formulation	117
6.5.2	Correlation Matrix Entries	117
6.5.3	Correlation Matrix Structure	122
6.5.4	Optimal Code Matrix Selection	124

6.5.5	Iterative Exhaustive Search Algorithm for Code Selection . . .	127
6.6	Sparse Reconstruction	129
6.7	Adaptive Waveform Amplitude Design	131
6.7.1	Design	131
6.7.2	Metric	133
6.8	Compressive Sensing	134
6.9	Numerical Simulations	135
6.9.1	Code Matrix Design	136
6.9.2	Sparse Support Recovery	138
6.9.3	Adaptive Waveform Amplitude Design	140
6.9.4	Compressive Sensing	145
6.10	Summary	146
7	Sparsity-based MIMO Noise Radar for Multiple Target Estimation	148
7.1	Introduction	148
7.2	Signal Model	149
7.3	Sparse Representation	152
7.4	Sparse Reconstruction	153
7.5	Numerical Simulations	154
7.6	Summary	157
8	Conclusions	158
8.1	Summary	158
8.2	Future Work	160
	References	162
	Vita	170

List of Tables

3.1	Game corresponding to transmitter 1.	44
3.2	Game corresponding to transmitter 2.	44
3.3	Game corresponding to transmitter 1 after removing player 2 dominated strategies.	45
3.4	Game corresponding to transmitter 2 after removing player 2 dominated strategies.	45
3.5	Modified game corresponding to transmitter 1.	48
4.1	Tracking algorithm	66

List of Figures

2.1	MIMO radar system with widely separated antennas.	7
2.2	Cumulative distribution function of the test statistic for the chosen example under the null hypothesis: (a) Sample cdf, (b) Gamma approximation.	22
2.3	ROC curves demonstrating the improvement offered by the optimal choice of polarizations when $\sigma^2 = 0.2$	23
2.4	Probability of detection (P_D) as a function of the complex noise variance when $P_{FA} = 0.02$	24
2.5	ROC curves demonstrating the improvement offered by employing multiple widely separated antennas compared with single input single output systems when $\sigma^2 = 0.2$	25
2.6	Comparison of performance between systems with scalar measurements and those with 2D vector measurements as a function of the probability of false alarm when $\sigma^2 = 0.1$	26
2.7	Comparison of performance between systems with scalar measurements and those with 2D vector measurements as a function of the noise variance when $P_{FA} = 0.02$	27
3.1	ROC curves when the complex noise variance $\sigma^2 = 0.2$	47
3.2	Probability of detection as a function of the noise variance when $P_{FA} = 0.02$	48
3.3	ROC curves demonstrating the improvement due to the mixed strategy solution.	50
3.4	Probability of detection as a function of the noise variance when $P_{FA} = 0.02$	51
4.1	Our proposed monopulse MIMO radar system.	54
4.2	Overlapping monopulse beams at one of the receivers.	55
4.3	Monopulse MIMO radar receivers.	55
4.4	Spatial beamformer at the receiver.	59
4.5	Responses of the two spatial filters as a function of the angle.	61
4.6	Monopulse ratio as a function of the angle.	64
4.7	Polygon formed by the points of intersection of the boresight axes of three receivers.	65
4.8	Simulated radar-target scenario.	68

4.9	Comparing the angle error of SISO and MIMO monopulse radars as a function of the pulse index for $\sigma^2 = 0.1$.	71
4.10	Comparing the average angle error of SISO and MIMO monopulse radars as a function of the complex noise variance σ^2 .	72
4.11	Comparing the average distance errors of 2x3 MIMO and conventional radars as a function of the complex noise variance σ^2 .	73
4.12	Monopulse MIMO tracker for a rapidly maneuvering airborne target for $\sigma^2 = 0.1$.	74
4.13	Monopulse MIMO tracker for a rapidly maneuvering airborne target in the presence of a jammer for $\sigma^2 = 0.1$.	75
4.14	Monopulse MIMO tracker for a rapidly maneuvering airborne target using sequential lobing in the presence of a jammer for $\sigma^2 = 0.1$.	76
4.15	Monopulse MIMO tracker for a maneuvering ground target for $\sigma^2 = 0.1$.	77
5.1	Block coherence measure as a function of the distance between adjacent grid points.	90
5.2	Reconstructed vectors using basis pursuit de-noising at SNR=3.7dB, (a) position estimates, (b) velocity estimates.	95
5.3	Reconstructed vectors using block-matching pursuit at SNR=3.7dB, (a) position estimates, (b) velocity estimates.	96
5.4	Performance metric Δ for basis pursuit de-noising and block-matching pursuit as a function of SNR.	97
5.5	Reconstructed vectors with optimal energy allocation at SNR=3.7dB, (a) position estimates, (b) velocity estimates.	98
5.6	Performance metric Δ with and without adaptive energy allocation.	99
5.7	Performance metric Δ for MIMO and SISO systems as a function of the noise level σ .	100
5.8	Performance metric Δ for different percentages of samples.	101
5.9	Performance metric Δ with and without adaptive energy allocation with 25% of samples.	102
5.10	Reconstructed vectors with optimal energy allocation at SNR=3.7dB using 25% of the samples, (a) position estimates, (b) velocity estimates.	103
5.11	Reconstructed vectors with optimal energy allocation at SNR=3.7dB with 20% modeling errors in all the targets, (a) position estimates, (b) velocity estimates.	104
5.12	Reconstructed vectors with optimal energy allocation at SNR=3.7dB with 95% modeling errors in one of the targets in one dimension, (a) position estimates, (b) velocity estimates.	105
6.1	Example of a frequency hopping waveform with three hopping intervals.	108
6.2	Transmit/Receive antenna array.	109
6.3	Flowchart of code selection algorithm.	129
6.4	$\beta(\mathbf{C})$ as a function of the number of hopping intervals.	137

6.5	Target estimates using BMP at an SNR of 2.6574dB.	139
6.6	Amplitudes of waveforms from $M_T = 3$ transmitters.	140
6.7	Curves demonstrating the improvement in performance due to adaptive amplitude design.	142
6.8	Curves demonstrating the improvement in performance due to adaptive amplitude design in the low SNR region.	143
6.9	Target estimates using BMP at an SNR of -21 dB.	143
6.10	Target estimates using BMP at an SNR of -21 dB while employing adaptive amplitude design.	144
6.11	Target estimates using BMP at an SNR of 2.6574dB with $\delta = 20\%$	145
6.12	Performance metric Δ as a function of SNR for different levels of compression.	146
6.13	Curves demonstrating the improvement in performance due to adaptive amplitude design when $\delta = 10\%$	147
7.1	Transmit/Receive antenna array used in monostatic configuration.	149
7.2	ℓ_2 norms of the target returns as a function of the Walsh code index.	155
7.3	ℓ_2 norm of the minimum target returns as a function of the Walsh code index.	155
7.4	Reconstructed sparse vector using optimal Walsh codes.	156

Chapter 1

Introduction

1.1 Background

Multiple Input Multiple Output (MIMO) radar has attracted much attention recently due to the additional degrees of freedom and improvement in performance it offers over conventional single antenna systems [1]. MIMO radar is typically used in two antenna configurations, namely distributed and colocated. In distributed MIMO radar [1], [2] the antennas are widely separated. This enables viewing the target from different angles. Hence, if the target returns between a particular transmitter and receiver are weak, then it is highly likely that they will be compensated for by the returns between other antenna pairs. While distributed MIMO radar exploits spatial diversity, colocated MIMO radar [3], [4] exploits waveform diversity. In a colocated configuration, all the antennas are closely spaced, and hence the target Radar Cross Section (RCS) values are the same for all transmitter-receiver pairs. RCS denotes the transformation undergone by the transmitted signal during reflection from the surface of the target. This is contrary to the distributed antenna configuration, where each pair has a different RCS value. In this dissertation, we develop and analyze signal

processing algorithms to detect, estimate, and track targets using both colocated and distributed MIMO radar.

1.2 Our Contributions

We proposed a radar system that combines the advantages of distributed MIMO radar and polarimetric MIMO radar in order to detect a point-like stationary target. The proposed system employs two-dimensional vector sensors at the receivers, each of which separately measures the horizontal and vertical components of the received electric field. We designed the optimal Neyman-Pearson detector for such systems and derived approximate analytical expressions for the probability of false alarm and probability of detection. Using numerical simulations, we demonstrated that optimal design of the antenna polarizations provides improved performance over MIMO systems that transmit waveforms of fixed polarizations over all the antennas. We also demonstrated that having multiple widely separated antennas gives improved performance over SISO polarimetric radar. Further, we showed that separately processing the vector measurements at each receiver gives improved performance over systems that linearly combine both the received signals to give scalar measurements.

Using a game theoretic framework, we formulated the selection of transmit polarizations for distributed MIMO radar as a game between the opponent and the radar design engineer by examining the impact of all possible transmit schemes on the different available target profiles. This approach does not require accurate estimation of target properties from measured data, unlike conventional approaches that are very sensitive to the accuracy of these estimates. Hence it can be implemented in practice without much cost. Further, this design approach utilizes knowledge about the goals

of both the target and the radar, unlike conventional approaches that ignore knowledge about the goal of the target. This game theoretic framework is very general and can be applied to other radar waveform design problems also.

We developed a MIMO radar system with widely separated antennas that employs monopulse processing at each of the receivers. We used Capon beamforming to generate the two beams required for the monopulse processing. We also proposed an algorithm for tracking a moving target using this system. This algorithm is simple and practical to implement. It efficiently combines the information present in the local estimates of the receivers. Since most modern tracking radars already use monopulse processing at the receiver, the proposed system does not need much additional hardware to be put to use. We simulated a realistic radar-target scenario to demonstrate that the spatial diversity offered by the use of multiple widely separated antennas gives significant improvement in performance when compared to conventional SISO monopulse radar systems. We also showed that the proposed algorithm keeps track of rapidly maneuvering airborne and ground targets under hostile conditions such as jamming.

We proposed a novel approach to accurately estimate properties (position, velocity) of multiple moving targets using distributed MIMO radar by employing sparse modeling. We also introduced a new realistic metric to analyze the performance of the radar system. This metric is generic and can be applied to other multiple target estimation problems also. Further, we proposed an adaptive mechanism for optimal energy allocation at the different transmit antennas. This adaptive energy allocation mechanism significantly improves the performance over MIMO radar systems that transmit fixed equal energy across all the antennas. We also demonstrated accurate reconstruction from very few samples by using compressive sensing at the receivers.

We considered the problem of multiple target estimation using a colocated MIMO radar system. We employed sparse modeling to estimate the unknown target parameters (delay, Doppler) using a MIMO radar system that transmits frequency-hopping waveforms. We formulated the measurement model using a block sparse representation and adaptively designed the transmit waveform parameters (frequencies, amplitudes) to achieve improved estimation performance. First, we derived analytical expressions for the correlations between the different blocks of columns of the sensing matrix. Using these expressions, we computed the block coherence measure of the dictionary. We used this measure to optimally design the sensing matrix by selecting the hopping frequencies for all the transmitters. Second, we adaptively designed the amplitudes of the transmitted waveforms during each hopping interval to improve the estimation performance. Using numerical simulations, we demonstrated the performance improvement due to the optimal design of waveform parameters. Further, we employed compressive sensing to perform accurate estimation from far fewer samples than the Nyquist rate.

Finally, we considered that each antenna of a colocated MIMO radar array transmits noise waveforms to achieve high resolution. These waveforms are further covered by codes that are inspired from code division multiple access (CDMA) to exploit code diversity. We formulated the measurement model using a sparse representation in an appropriate basis to estimate the unknown target parameters (delays, Dopplers) using support recovery algorithms. We demonstrated the performance of this system using numerical simulations.

Chapter 2

Polarimetric MIMO Radar with Distributed Antennas for Target Detection¹

2.1 Introduction

The polarization properties of any electro-magnetic wave are usually altered when the wave reflects from the surface of a target. The target scattering matrix determines the change in polarization of the transmitted signal [5], [6]. Therefore, knowledge about the target in terms of its scattering matrix helps us design the optimal transmit waveform polarizations for performance improvement over systems transmitting waveforms with fixed polarizations over all the antennas. In [7], [8], [9], [10], [11], polarimetric design is suggested for use in conventional single antenna radar systems for problems such as detection, estimation and tracking. In [12], radar polarimetry is

¹Based on S. Gogineni and A. Nehorai, "Polarimetric MIMO radar with distributed antennas for target detection," *IEEE Trans. Signal Process.*, vol. 58, no. 3, pp. 1689-1697, Mar. 2010. ©[2010] IEEE.

also used in multiple antenna systems with colocated antennas. In this chapter, we propose a radar system that combines the advantages of distributed-antenna MIMO systems with the advantages offered by optimally choosing the transmit waveform polarizations (see also [13], [14]). We examine the problem of target detection for stationary point targets.

2.2 Signal Model

Before we develop the mathematical model, we describe the target and the radar system. We assume that the target is stationary and is present in the illuminated space. The target is further assumed to be point-like with a scattering matrix that depends on the angle of view. We consider a radar system that has M transmit antennas and N receive antennas with all the antennas widely spaced as shown in Figure 2.1. Each of the receive antennas employs a two-dimensional vector sensor that measures both the horizontal and vertical components of the received polarized signal separately. Polarimetric models exist for describing the signals received in single-antenna systems [5], [6]. We extend these models to distributed antenna systems in this section.

We begin by describing the signals on the transmitter side. Define the polarization vector for the i^{th} transmitter to be $\mathbf{t}^i = [t_h^i, t_v^i]^T$, where each of the entries of the polarization vectors is a complex number and $[\cdot]^T$ represents the transpose of $[\cdot]$. We further assume that $\|\mathbf{t}^i\| = 1, \forall i = 1, \dots, M$. The complex pulse wave shape transmitted from the i^{th} transmit antenna is defined as $w^i(t)$. We assume that all these transmit waveforms are orthonormal to each other for all mutual delays between them [1], [2]. In other words, we assume that the cross correlation among these different

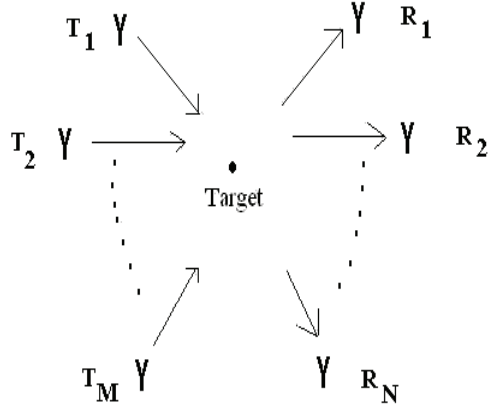


Figure 2.1: MIMO radar system with widely separated antennas.

waveforms is negligible for different lags. At the receiver side, this condition helps us differentiate between the signals transmitted from different transmit antennas.

After transmission, the polarized waveforms will travel in space and reflect off the surface of the target towards the receivers with altered polarimetric properties. We now consider the measurements on the receiver side. The polarized signal reaching the j^{th} receive antenna is a combination of all the signals reflecting from the surface of the target towards the j^{th} receiver. Let $\mathbf{y}^j(t)$ be the complex envelope of the signal received by the j^{th} receive antenna. Note that $\mathbf{y}^j(t)$ is a 2-dimensional column vector consisting of the horizontal and the vertical components of the received signal, and it is expressed using a formulation similar to that presented in [15], [16], [17]:

$$\mathbf{y}^j(t) = \sum_{i=1}^M a^{ij} \mathbf{S}^{ij} \mathbf{t}^i w^i(t - \tau^{ij}) + \mathbf{e}^j(t), \quad (2.1)$$

where $\mathbf{e}^j(t)$ is the 2-dimensional additive noise, τ^{ij} is the time delay because of propagation and the attenuation is divided into two factors a^{ij} and \mathbf{S}^{ij} . a^{ij} is that part of attenuation which depends on the properties of the medium, distance between

the target and radar, etc. We assume that the coefficients $\{a^{ij}\}$ are known because the radar has an idea about the region which it is illuminating and the properties of the medium. \mathbf{S}^{ij} represents the scattering matrix of the target, which completely describes the change in the polarimetric properties of the signal transmitted from the i^{th} transmit antenna to the j^{th} receive antenna. This represents the unknown part of the attenuation. It has four complex components and is given as

$$\mathbf{S}^{ij} = \begin{bmatrix} s_{hh}^{ij} & s_{hv}^{ij} \\ s_{vh}^{ij} & s_{vv}^{ij} \end{bmatrix}. \quad (2.2)$$

In order to separate the signals coming from different transmit antennas, the received signal is processed using a series of M matched filters at each receiver. At each receiver, the i^{th} matched filter corresponds to a matching with the i^{th} transmit waveform. We derive the mathematical model for the proposed MIMO radar system by using an approach similar to that presented for the single antenna system in [15]. The signals at the output of the matched filters are normalized by dividing by a^{ij} . Note that normalization changes the variances of the normalized noise term, and hence these variances need not be the same for all transmitter–receiver pairs. The normalized vector output of the i^{th} matched filter at the j^{th} receiver is expressed as

$$\mathbf{y}^{ij} = \mathbf{S}^{ij}\mathbf{t}^i + \mathbf{e}^{ij}, \quad (2.3)$$

where the column vector $\mathbf{y}^{ij} = [y_h^{ij}, y_v^{ij}]^T$ consists of the horizontal and vertical components, respectively. We have now obtained the expressions for the measurements at each of the antennas on the receiver side. Next we perform some simple operations to express all these measurements using a linear model.

Stacking the elements of the scattering matrix \mathbf{S}^{ij} into a vector, we define $\mathbf{s}^{ij} = [s_{\text{hh}}^{ij}, s_{\text{hv}}^{ij}, s_{\text{vh}}^{ij}, s_{\text{vv}}^{ij}]^T$. There are MN such vectors, and arranging them into a single vector gives us a $4MN \times 1$ dimensional column vector:

$$\mathbf{s} = [(\mathbf{s}^{11})^T, \dots, (\mathbf{s}^{1N})^T, \dots, (\mathbf{s}^{M1})^T, \dots, (\mathbf{s}^{MN})^T]^T. \quad (2.4)$$

Similarly, stacking the normalized outputs of the matched filters and also the corresponding additive noise components into column vectors, we define

$$\mathbf{y} = [(\mathbf{y}^{11})^T, \dots, (\mathbf{y}^{1N})^T, \dots, (\mathbf{y}^{M1})^T, \dots, (\mathbf{y}^{MN})^T]^T, \quad (2.5)$$

$$\mathbf{e} = [(\mathbf{e}^{11})^T, \dots, (\mathbf{e}^{1N})^T, \dots, (\mathbf{e}^{M1})^T, \dots, (\mathbf{e}^{MN})^T]^T. \quad (2.6)$$

Define a set of matrices

$$\mathbf{P}^i = \begin{bmatrix} t_{\text{h}}^i & t_{\text{v}}^i & 0 & 0 \\ 0 & 0 & t_{\text{h}}^i & t_{\text{v}}^i \end{bmatrix}, \quad (2.7)$$

$\forall i = 1, \dots, M$, each corresponding to a particular transmit antenna.

Using the above definitions, we express the measurement vector \mathbf{y} using the following mathematical model:

$$\mathbf{y} = \mathbf{H}\mathbf{s} + \mathbf{e}, \quad (2.8)$$

where

$$\mathbf{H} = \begin{bmatrix} \mathbf{P}^1 & \dots & \mathbf{0} & \dots & \mathbf{0} & \dots & \mathbf{0} \\ \vdots & \ddots & \vdots & \vdots & \vdots & \vdots & \vdots \\ \mathbf{0} & \dots & \mathbf{P}^1 & \dots & \mathbf{0} & \dots & \mathbf{0} \\ \vdots & \vdots & \vdots & \ddots & \vdots & \vdots & \vdots \\ \mathbf{0} & \dots & \mathbf{0} & \dots & \mathbf{P}^M & \dots & \mathbf{0} \\ \vdots & \vdots & \vdots & \vdots & \vdots & \ddots & \vdots \\ \mathbf{0} & \dots & \mathbf{0} & \dots & \mathbf{0} & \dots & \mathbf{P}^M \end{bmatrix}. \quad (2.9)$$

$\mathbf{0}$ is a zero matrix of dimensions 2×4 . Terms \mathbf{y} and \mathbf{e} are $2MN \times 1$ dimensional observation and noise vectors respectively. Thus, we have reduced our mathematical model to the well-known linear form. We now look at the statistical assumptions made on these terms.

We assume that the noise terms present in \mathbf{e} are uncorrelated and that \mathbf{e} follows proper complex Gaussian distribution. A complex random vector $\boldsymbol{\varsigma} = \boldsymbol{\varsigma}_R + j\boldsymbol{\varsigma}_I$ is said to be proper if $\text{Cov}(\boldsymbol{\varsigma}_R, \boldsymbol{\varsigma}_R) = \text{Cov}(\boldsymbol{\varsigma}_I, \boldsymbol{\varsigma}_I)$ and $\text{Cov}(\boldsymbol{\varsigma}_R, \boldsymbol{\varsigma}_I) = -\text{Cov}(\boldsymbol{\varsigma}_I, \boldsymbol{\varsigma}_R)$. Hence, the covariance matrix of \mathbf{e} will be diagonal. This diagonal assumption states that the noise components at the outputs of the matched filters across the various widely separated receivers over both the polarizations are statistically independent for any given time snapshot. This assumption is reasonable given the wide separation between the antennas [2]. The diagonal entries of the covariance matrix of \mathbf{e} need not be the same because of the normalization performed at the output of each of the matched filters, as mentioned earlier. Define this covariance matrix as $\boldsymbol{\Sigma}_e$ and assume that it is known. The matrix \mathbf{H} is a $2MN \times 4MN$ dimensional design matrix whose constituent elements depend on the transmit waveform polarizations. We assume that the vector \mathbf{s} , which contains elements from all the scattering matrices, is a random

vector following proper complex Gaussian distribution with a $4MN \times 4MN$ covariance matrix given by Σ_s . We further assume that Σ_s is known. If the random matrices \mathbf{S}^{ij} are statistically independent, then Σ_s will have a block diagonal structure. However, we do not impose any such structural constraint on Σ_s . Furthermore, we assume that \mathbf{s} and \mathbf{e} are independent. Since we have described all the terms in our measurement model, we shall formally state the detection problem in the next section.

2.3 Problem Formulation

The above mathematical model gives an expression for the observation vector when the target is present in the illuminated space. When the target is absent, the observations will consist of only the receiver noise vector \mathbf{e} . Hence, the problem of detecting the target reduces to the following binary hypothesis testing problem:

$$H_0 : \mathbf{y} = \mathbf{e}, \quad (2.10)$$

$$H_1 : \mathbf{y} = \mathbf{H}\mathbf{s} + \mathbf{e}. \quad (2.11)$$

Therefore, under the null hypothesis, \mathbf{y} will have complex Gaussian distribution with zero mean and covariance matrix Σ_e . Under the alternative hypothesis, the independence of \mathbf{s} and \mathbf{e} implies that \mathbf{y} will follow complex Gaussian distribution with zero mean and covariance matrix given by $\mathbf{C} + \Sigma_e$, where $\mathbf{C} = \mathbf{H}\Sigma_s\mathbf{H}^H$ denotes the covariance matrix of $\mathbf{H}\mathbf{s}$. This result is an application of the well-known properties of Gaussian random vectors [18]. Next we describe the Neyman-Pearson detector for this problem.

2.4 Detector

2.4.1 Test Statistic

Under the above-mentioned hypotheses, the probability density functions of the observation vector are given as

$$f(\mathbf{y}|H_0) \propto \frac{1}{|\boldsymbol{\Sigma}_e|} e^{-\mathbf{y}^H \boldsymbol{\Sigma}_e^{-1} \mathbf{y}}, \quad (2.12)$$

$$f(\mathbf{y}|H_1) \propto \frac{1}{|\boldsymbol{\Sigma}_e + \mathbf{C}|} e^{-\mathbf{y}^H (\boldsymbol{\Sigma}_e + \mathbf{C})^{-1} \mathbf{y}}. \quad (2.13)$$

The Neyman-Pearson lemma states that the likelihood ratio test is the most powerful test for any given size [19]. The likelihood ratio is given as

$$\frac{f(\mathbf{y}|H_0)}{f(\mathbf{y}|H_1)} = \frac{|\boldsymbol{\Sigma}_e + \mathbf{C}|}{|\boldsymbol{\Sigma}_e|} e^{-\mathbf{y}^H (\boldsymbol{\Sigma}_e^{-1} - (\boldsymbol{\Sigma}_e + \mathbf{C})^{-1}) \mathbf{y}}. \quad (2.14)$$

Computing the logarithm of the above expression and ignoring the known constants, we clearly see that $\mathbf{y}^H (\boldsymbol{\Sigma}_e^{-1} - (\boldsymbol{\Sigma}_e + \mathbf{C})^{-1}) \mathbf{y}$ is our test statistic and we compare it with a threshold before selecting a hypothesis:

$$\mathbf{y}^H (\boldsymbol{\Sigma}_e^{-1} - (\boldsymbol{\Sigma}_e + \mathbf{C})^{-1}) \mathbf{y} \underset{H_0}{\overset{H_1}{\geq}} k, \quad (2.15)$$

where the threshold k is chosen based on the size specified for the test.

2.4.2 Estimation of Covariance Matrices

In practice, the covariance matrices needed for implementing the detector may not be known in advance. In such a scenario, the maximum likelihood estimates (MLE) of these matrices can be substituted to perform the test. Since the observations follow Gaussian distribution under both the hypotheses, the MLE of the covariance matrices are given by the corresponding sample covariance matrices [19], [20]. The sample covariance matrices are easy to compute in practice. The variance of noise at each receiver is calculated before the detector starts functioning by evaluating the sample variance using a large set of training data. The covariance matrix under the alternative hypothesis is estimated by evaluating the sample covariance matrix using all the samples of observations in a particular window of time when the detector is in use. These two estimated matrices are sufficient for implementing the detector. If there is no target in the illuminated space, then these two estimated matrices will be close to each other, thereby causing the test statistic to fall below the threshold.

2.4.3 Performance Analysis

In order to analyze the performance of the above-mentioned detector, we need to know the distribution of the test statistic under both hypotheses. The test statistic is a quadratic form of the complex Gaussian random vector \mathbf{y} . It is well known in statistics that a quadratic form $\mathbf{z}^T \mathbf{U} \mathbf{z}$ of a real Gaussian random vector \mathbf{z} with covariance matrix \mathbf{B} will follow Chi-square distribution if and only if the matrix $\mathbf{U} \mathbf{B}$ is idempotent [21]. Using this result, we infer that our test statistic does not necessarily follow Chi-square distribution for all feasible choices of Σ_e and \mathbf{C} because we did not impose any constraint on Σ_s . Hence, it is difficult to find the exact probability

density function (pdf) for it. In order to study the pdf of our test statistic, we first begin with an assumption that \mathbf{C} is diagonal. Later, we will extend this approach to the non-diagonal case by applying proper diagonalization.

Define the l^{th} diagonal element of \mathbf{C} as c^l and that of Σ_e as v^l . Then, the test statistic reduces to

$$\sum_{i=1}^M \sum_{j=1}^N \left(\left(\frac{1}{v^{(2(i-1)N+2j-1)}} - \frac{1}{v^{(2(i-1)N+2j-1)} + c^{(2(i-1)N+2j-1)}} \right) |y_{\text{h}}^{ij}|^2 \right) + \sum_{i=1}^M \sum_{j=1}^N \left(\left(\frac{1}{v^{(2(i-1)N+2j)}} - \frac{1}{v^{(2(i-1)N+2j)} + c^{(2(i-1)N+2j)}} \right) |y_{\text{v}}^{ij}|^2 \right),$$

where $y_{\text{h}}^{ij}, y_{\text{v}}^{ij}$ are always independent Gaussian random variables under both hypotheses for all transmitter–receiver pairs because of the diagonal assumption of Σ_e and \mathbf{C} . Therefore, the test statistic is a weighted sum of independent Chi-square random variables and it does not necessarily follow the Chi-square distribution. Its actual distribution depends on the weights. The pdf of a sum of independent random variables is obtained by performing multiple convolutions among the constituent pdfs. However, in this case, it is difficult to find the exact solution. Hence, we shall look for approximations to the actual pdf.

In [22], the distribution of the weighted sum of Chi squares is studied. If π_q are real positive constants and N_q are independent standard normal random variables $\forall q = 1, \dots, K$, then the pdf of the Gamma approximation of $R = \sum_{q=1}^K \pi_q N_q^2$ is given as

$$f_R(r, \alpha, \beta) = r^{\alpha-1} \frac{e^{-\frac{r}{\beta}}}{\beta^\alpha \Gamma(\alpha)}, \quad (2.16)$$

where the parameters α and β are given as

$$\alpha = \frac{1}{2} \left(\frac{\left(\sum_{q=1}^K \pi_q \right)^2}{\sum_{q=1}^K \pi_q^2} \right), \quad (2.17)$$

$$\beta = \left(\frac{1}{2} \left(\frac{\sum_{q=1}^K \pi_q}{\sum_{q=1}^K \pi_q^2} \right) \right)^{-1}. \quad (2.18)$$

Γ is the gamma function defined as $\Gamma(\alpha) = \int_0^\infty t^{\alpha-1} e^{-t} dt$.

Under the null hypothesis, y_h^{ij} and y_v^{ij} have zero mean and variances $v^{(2(i-1)N+2j-1)}$ and $v^{(2(i-1)N+2j)}$, respectively. Hence, applying the above approximation with appropriate weights, the parameters of the Gamma distribution are

$$\alpha_{H_0} = \left(\frac{\left(\sum_{l=1}^{2MN} \frac{c^l}{v^l + c^l} \right)^2}{\sum_{l=1}^{2MN} \left(\frac{c^l}{v^l + c^l} \right)^2} \right), \quad (2.19)$$

$$\beta_{H_0} = \left(\frac{\sum_{l=1}^{2MN} \frac{c^l}{v^l + c^l}}{\sum_{l=1}^{2MN} \left(\frac{c^l}{v^l + c^l} \right)^2} \right)^{-1}. \quad (2.20)$$

Under the alternative hypothesis, y_h^{ij} and y_v^{ij} have zero mean and variances $v^{(2(i-1)N+2j-1)} + c^{(2(i-1)N+2j-1)}$ and $v^{(2(i-1)N+2j)} + c^{(2(i-1)N+2j)}$, respectively. The parameters of the Gamma approximation are

$$\alpha_{H_1} = \left(\frac{\left(\sum_{l=1}^{2MN} \frac{c^l}{v^l} \right)^2}{\sum_{l=1}^{2MN} \left(\frac{c^l}{v^l} \right)^2} \right), \quad (2.21)$$

$$\beta_{H_1} = \left(\frac{\sum_{l=1}^{2MN} \frac{c^l}{v^l}}{\sum_{l=1}^{2MN} \left(\frac{c^l}{v^l}\right)^2} \right)^{-1}. \quad (2.22)$$

Note that so far we have assumed a diagonal structure for matrix \mathbf{C} in the above discussion. However, we still need to find expressions for the pdf of the test statistic when \mathbf{C} is not diagonal. Diagonalization will be used to extend the analysis even for the case of non-diagonal matrices [23]. Since Σ_e and \mathbf{C} are covariance matrices, $(\Sigma_e^{-1} - (\Sigma_e + \mathbf{C})^{-1})$ will be a Hermitian matrix, which therefore decomposes into $\mathbf{D}^H \mathbf{\Lambda} \mathbf{D}$, where $\mathbf{\Lambda}$ is a diagonal matrix consisting of eigenvalues as the diagonal elements and \mathbf{D} contains the corresponding orthonormal eigenvectors. The test statistic now becomes $(\mathbf{D}\mathbf{y})^H \mathbf{\Lambda} (\mathbf{D}\mathbf{y})$. If we show that $\mathbf{D}\mathbf{y}$ has a diagonal covariance matrix under both hypotheses, then our analysis extends to the case in which \mathbf{C} is not diagonal also, with appropriate adjustments made to the parameters of the Gamma approximation. Under H_0 , $\mathbf{D}\mathbf{y}$ is a complex Gaussian random vector with a covariance matrix $\text{Cov}_{H_0}(\mathbf{D}\mathbf{y}) = \mathbf{D}\Sigma_e\mathbf{D}^H$, which is diagonal because Σ_e is diagonal and \mathbf{D} has orthonormal vectors. Similarly, under H_1 , $\mathbf{D}\mathbf{y}$ is a complex normal random vector with covariance matrix

$$\text{Cov}_{H_1}(\mathbf{D}\mathbf{y}) = \mathbf{D}(\Sigma_e + \mathbf{C})\mathbf{D}^H, \quad (2.23)$$

$$= (\mathbf{D}(\Sigma_e + \mathbf{C})^{-1}\mathbf{D}^H)^{-1}, \quad (2.24)$$

$$= (\mathbf{D}((\Sigma_e + \mathbf{C})^{-1} - \Sigma_e^{-1} + \Sigma_e^{-1})\mathbf{D}^H)^{-1}, \quad (2.25)$$

$$= (\mathbf{D}\Sigma_e^{-1}\mathbf{D}^H - \mathbf{\Lambda})^{-1}, \quad (2.26)$$

which is diagonal. Hence, under both hypotheses, the test statistic is a weighted sum of Chi square random variables even when matrix \mathbf{C} is not diagonal. The only

difference is that the weights will now be different, and they are defined by the diagonalization process.

After approximating the pdf using the Gamma density, the probability of detection (P_D) and the probability of false alarm (P_{FA}) are defined as follows:

$$P_D = \int_k^\infty t^{\alpha_{H_1}-1} \frac{e^{-\frac{t}{\beta_{H_1}}}}{\beta_{H_1}^{\alpha_{H_1}} \Gamma(\alpha_{H_1})} dt, \quad (2.27)$$

$$P_{FA} = \int_k^\infty t^{\alpha_{H_0}-1} \frac{e^{-\frac{t}{\beta_{H_0}}}}{\beta_{H_0}^{\alpha_{H_0}} \Gamma(\alpha_{H_0})} dt, \quad (2.28)$$

where the parameters α_{H_0} , β_{H_0} , α_{H_1} , and β_{H_1} are as mentioned earlier. For a given value of P_{FA} , the value of the threshold k is calculated easily using the above expression because functions for evaluating the above expressions exist in MATLAB. After finding the threshold, P_D is calculated accordingly. Note that the value of the threshold and P_D depends on matrix \mathbf{C} , which in turn depends on the polarizations of the transmitted waveforms. Hence, the performance of the detector is related to the transmit waveform polarizations.

2.4.4 Optimal Design

In order to find the optimal design, we perform a grid search over the possible waveform polarizations across all the transmit antennas with the help of the above expressions for P_D and P_{FA} . The optimal design corresponds to the transmit polarizations that give the maximum P_D for a given P_{FA} . Later, we will plot the ROC curves to visualize the improvement in performance because of the optimal design.

2.5 Scalar Measurement Model

Most of the conventional polarimetric radar systems combine the two received signals linearly and coherently at each receiver to give only a scalar measurement that depends on the receive polarization vector. For such systems, the output at each receive antenna is modeled as an inner product of the received signal and the receive antenna polarization [6], [15]. This receive polarization vector is optimally chosen along with the transmit waveform polarizations in order to achieve improved performance. We now use a similar approach to that used earlier in this chapter in order to obtain the signal model for such systems. From now on, we refer to this model as the scalar measurement model.

Let $\mathbf{r}^j = [r_h^j, r_v^j]^T$ be the polarization vector of the j^{th} receiver, where each of the entries is a complex number. We further assume that $\|\mathbf{r}^j\| = 1, \forall j = 1, \dots, N$. The rest of the variables remain the same as defined earlier, except that the measurement and the noise at each receiver according to this model will be complex scalars. The scalar observation at the j^{th} receiver $y^j(t)$ is now expressed as follows [15], [16], [17]:

$$y^j(t) = \sum_{i=1}^M a^{ij} \mathbf{r}^{jT} \mathbf{S}^{ij} \mathbf{t}^i w^i(t - \tau^{ij}) + e^j(t). \quad (2.29)$$

This signal is now passed through a series of matched filters whose outputs are appropriately normalized to move the effect of a^{ij} into the noise term. Finally, the normalized output of the i^{th} matched filter at the j^{th} receiver is given as

$$y^{ij} = \mathbf{r}^{jT} \mathbf{S}^{ij} \mathbf{t}^i + e^{ij}. \quad (2.30)$$

Stacking all the observations and the noise components into column vectors, we obtain $MN \times 1$ dimensional vectors \mathbf{y} and \mathbf{e} , respectively. Vector \mathbf{s} remains the same as defined earlier. However, matrix \mathbf{H} changes and now contains the elements of the receive polarization vectors also. Let us define a set of vectors

$$\boldsymbol{\eta}^{ij} = [(\mathbf{r}_h^j \mathbf{t}_h^i), (\mathbf{r}_h^j \mathbf{t}_v^i), (\mathbf{r}_v^j \mathbf{t}_h^i), (\mathbf{r}_v^j \mathbf{t}_v^i)], \quad (2.31)$$

$\forall i = 1, \dots, M$, each of which corresponds to a particular transmitter–receiver pair. Under this definition, the observation vector is expressed as

$$\mathbf{y} = \mathbf{H}\mathbf{s} + \mathbf{e}, \quad (2.32)$$

where \mathbf{H} is a $MN \times 4MN$ dimensional matrix given by

$$\mathbf{H} = \begin{bmatrix} \boldsymbol{\eta}^{11} & \dots & \mathbf{0} & \dots & \mathbf{0} & \dots & \mathbf{0} \\ \vdots & \ddots & \vdots & \vdots & \vdots & \vdots & \vdots \\ \mathbf{0} & \dots & \boldsymbol{\eta}^{1N} & \dots & \mathbf{0} & \dots & \mathbf{0} \\ \vdots & \vdots & \vdots & \ddots & \vdots & \vdots & \vdots \\ \mathbf{0} & \dots & \mathbf{0} & \dots & \boldsymbol{\eta}^{M1} & \dots & \mathbf{0} \\ \vdots & \vdots & \vdots & \vdots & \vdots & \ddots & \vdots \\ \mathbf{0} & \dots & \mathbf{0} & \dots & \mathbf{0} & \dots & \boldsymbol{\eta}^{MN} \end{bmatrix}. \quad (2.33)$$

Therefore, we obtain a similar linear model even for the systems with scalar measurements. The only difference lies in the dimensionality of some of the vectors in the model and also the constituent elements of the matrix \mathbf{H} . The optimal design for such a system will not only include optimization over the transmit polarizations \mathbf{t}^i but will also include the optimal selection of the receive polarization vectors \mathbf{r}^j . The

problem formulation and analysis of the detector remains the same as for the earlier model because the basic structure of the model is still the same. Hence, the analysis performed in Section 2.4 is applicable even to this model. We use this analysis in the next section to demonstrate the advantage of retaining the vector measurements at each receiver without combining them.

2.6 Numerical Results

We consider a system with two transmit antennas and two receive antennas under the same target detection scenario as described so far. Hence, there are 16 complex elements in the random vector \mathbf{s} . We choose the covariance matrix of this vector to be of the following form:

$$\Sigma_{\mathbf{s}} = \begin{bmatrix} \Sigma_{\mathbf{s}}^{11} & \mathbf{0} & \mathbf{0} & \mathbf{0} \\ \mathbf{0} & \Sigma_{\mathbf{s}}^{12} & \mathbf{0} & \mathbf{0} \\ \mathbf{0} & \mathbf{0} & \Sigma_{\mathbf{s}}^{21} & \mathbf{0} \\ \mathbf{0} & \mathbf{0} & \mathbf{0} & \Sigma_{\mathbf{s}}^{22} \end{bmatrix}, \quad (2.34)$$

where $\Sigma_{\mathbf{s}}^{ij}$ represents the covariance matrix of the random vector \mathbf{s}^{ij} and $\mathbf{0}$ is a 4x4 dimensional zero matrix. Each of these matrices were chosen as follows:

$$\Sigma_{\mathbf{s}}^{11} = \begin{bmatrix} 0.3 & 0.1\epsilon & 0.1\epsilon & 0.1\epsilon \\ 0.1\epsilon^* & 0.2 & 0.1\epsilon & 0.1\epsilon \\ 0.1\epsilon^* & 0.1\epsilon^* & 0.4 & 0.1\epsilon \\ 0.1\epsilon^* & 0.1\epsilon^* & 0.1\epsilon^* & 0.5 \end{bmatrix}, \quad (2.35)$$

$$\Sigma_{\mathbf{s}}^{12} = \begin{bmatrix} 0.5 & 0.05\epsilon & 0.05\epsilon & 0.05\epsilon \\ 0.05\epsilon^* & 0.3 & 0.05\epsilon & 0.05\epsilon \\ 0.05\epsilon^* & 0.05\epsilon^* & 0.4 & 0.05\epsilon \\ 0.05\epsilon^* & 0.05\epsilon^* & 0.05\epsilon^* & 0.3 \end{bmatrix}, \quad (2.36)$$

$$\Sigma_{\mathbf{s}}^{21} = \begin{bmatrix} 0.4 & 0.1\epsilon & 0.1\epsilon & 0.1\epsilon \\ 0.1\epsilon^* & 0.3 & 0.1\epsilon & 0.1\epsilon \\ 0.1\epsilon^* & 0.1\epsilon^* & 0.2 & 0.1\epsilon \\ 0.1\epsilon^* & 0.1\epsilon^* & 0.1\epsilon^* & 0.4 \end{bmatrix}, \quad (2.37)$$

$$\Sigma_{\mathbf{s}}^{22} = \begin{bmatrix} 0.4 & 0.05\epsilon & 0.05\epsilon & 0.05\epsilon \\ 0.05\epsilon^* & 0.4 & 0.05\epsilon & 0.05\epsilon \\ 0.05\epsilon^* & 0.05\epsilon^* & 0.2 & 0.05\epsilon \\ 0.05\epsilon^* & 0.05\epsilon^* & 0.05\epsilon^* & 0.5 \end{bmatrix}, \quad (2.38)$$

where $\epsilon = 1 + \sqrt{-1}$. The complex elements of the noise vector \mathbf{e} are assumed to be uncorrelated, with the variance of each equal to $\sigma^2 = 0.2$. Before we use the Gamma approximation to obtain the optimal design, we first check if the approximation is reasonable, in our case by plotting the cumulative distribution function (cdf) of the approximate Gamma distribution and comparing it with that formed by generating random samples from the constituent Chi squares. This comparison assumes all the antennas are horizontally polarized.

In this scenario, we have the following information available:

$$\mathbf{t}^1 = [1, 0], \quad (2.39)$$

$$\mathbf{t}^2 = [1, 0]. \quad (2.40)$$

Therefore, the matrices \mathbf{P}^1 and \mathbf{P}^2 become $\mathbf{P}^1 = \mathbf{P}^2 = \begin{bmatrix} 1 & 0 & 0 & 0 \\ 0 & 0 & 1 & 0 \end{bmatrix}$. The matrix \mathbf{C} turns out to be non-diagonal for this example. Hence, after performing the appropriate diagonalization and calculating the weights, the coefficients of the Gamma approximation under the null hypothesis turn out to be $\alpha_{H_0} = 7.6833$ and $\beta_{H_0} = 0.6283$. Figure 2.2(b) shows the cdf of this approximated Gamma distribution with the above-mentioned parameters. In order to check if this is indeed a good approximation, we generated random samples of the observation vector \mathbf{y} under the null hypothesis. We evaluated the test statistic $\mathbf{y}^H (\boldsymbol{\Sigma}_e^{-1} - (\boldsymbol{\Sigma}_e + \mathbf{C})^{-1}) \mathbf{y}$ for each of these random samples and generated the sample cumulative distribution function, which is plotted in Figure 2.2(a). It is clear from both figures that the Gamma approximation we made is indeed very accurate and close to the sample distribution. This finding is consistent with the results presented in [22]. The sample cdf takes values 0.5827 and 0.9233 whereas the cdf of the Gamma approximation takes values 0.5863 and 0.9242 for argument values of 5 and 7.5 respectively. This shows that the values taken by these two curves differ only at the third decimal point.

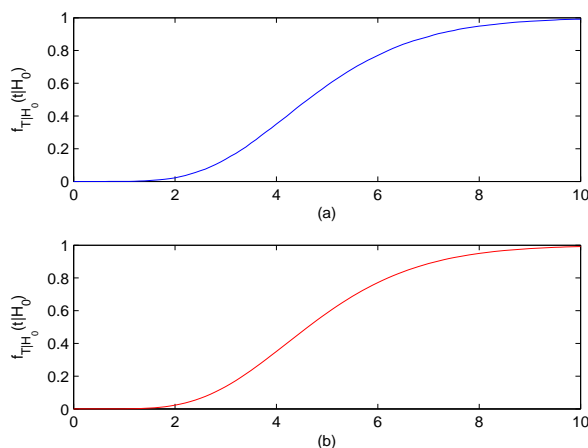


Figure 2.2: Cumulative distribution function of the test statistic for the chosen example under the null hypothesis: (a) Sample cdf, (b) Gamma approximation.

Now that we have a good enough approximation to the distribution of our test statistic, we look at how the optimal choice of polarizations improves the performance of the detector. We fix the complex noise variance to $\sigma^2 = 0.2$ and vary the value of P_{FA} . This method enables us to plot the optimal ROC curve by performing a grid search using the analytical results derived earlier in the chapter. Next, we obtain the reference curves for our results by computing the ROC curves assuming that all the transmit antennas are horizontally or vertically polarized. These plots are presented in Figure 2.3, and a significant improvement in performance is clearly visible while using the optimal waveform polarizations.

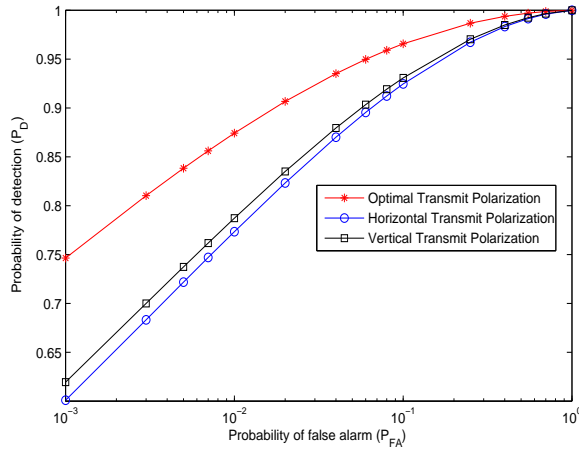


Figure 2.3: ROC curves demonstrating the improvement offered by the optimal choice of polarizations when $\sigma^2 = 0.2$.

We proceed with our analysis for this numerical example. First, we fix P_{FA} to be equal to 0.02. For this value of P_{FA} , we wish to check the improvement offered by the optimal design for different values of the noise variance. We plot the optimal P_D as a function of σ^2 . We also plot P_D as a function of σ^2 for the case in which only horizontal or vertical polarizations are used. The improvement in performance offered by the optimal design is clear from Figure 2.4.

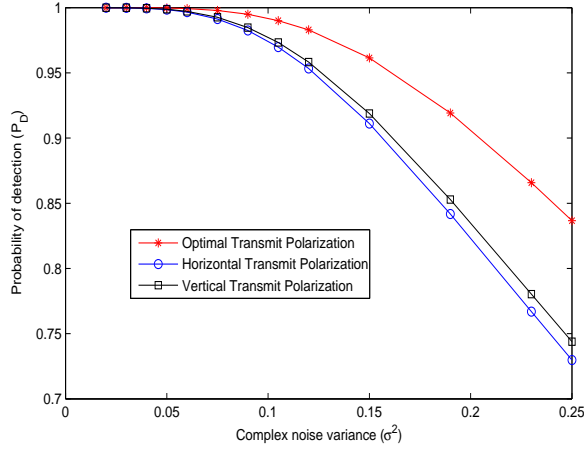


Figure 2.4: Probability of detection (P_D) as a function of the complex noise variance when $P_{FA} = 0.02$.

So far, we have demonstrated that by optimally selecting the transmit polarizations, we get performance improvement over conventional MIMO systems with fixed polarizations. Now, we plot the ROC curves for SISO radar with optimal transmit polarizations to show the gain in performance because of the multiple widely separated antennas. For the SISO system, we consider only the first transmit and receive antennas in our above mentioned example. Therefore, the covariance matrix of the scattering vector \mathbf{s} becomes $\Sigma_{\mathbf{s}} = \Sigma_{\mathbf{s}}^{11}$. In order to make a fair comparison, we transmit more power than the power transmitted per antenna while using MIMO radar. It is clear from Figure 2.5 that 2X2 polarimetric MIMO radar system significantly outperforms its SISO counterpart even when the SISO system uses four times the transmit power used by each antenna in the 2X2 system.

The complexity of the grid search for optimization using our proposed system model does not increase much with the increase in the number of receivers, because the number of variables over which the optimization is performed depends only on the number of transmit antennas. However, with the scalar measurement model, the

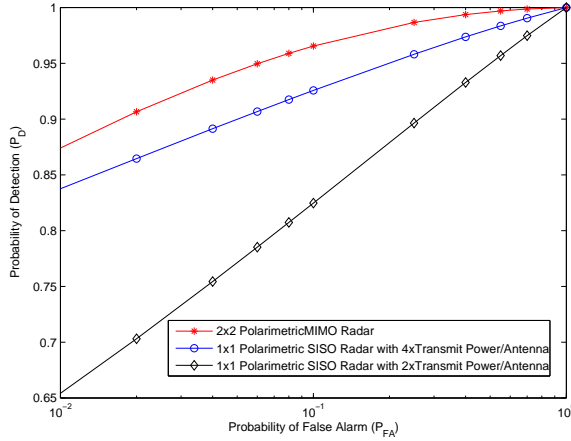


Figure 2.5: ROC curves demonstrating the improvement offered by employing multiple widely separated antennas compared with single input single output systems when $\sigma^2 = 0.2$.

addition of each extra receiver adds extra variables (receive polarization vectors) in the grid search and makes the calculations more complex. Therefore, in order to compare the performance of our proposed system with that of the scalar measurement system, we use the same numerical example as described so far; however, this time we stick to just two transmitters and one receiver to reduce the complexity of the optimization step. The Σ_s matrix now has the following form:

$$\Sigma_s = \begin{bmatrix} \Sigma_s^{11} & \mathbf{0} \\ \mathbf{0} & \Sigma_s^{21} \end{bmatrix}, \quad (2.41)$$

where matrices Σ_s^{11} and Σ_s^{21} are chosen to be the same, as defined earlier in this section. The noise variance remains the same for both the systems because the receive polarization vectors are assumed to be unit norm. We assume the same noise variance $\sigma^2 = 0.1$ for both systems in order to make a fair comparison. Figure 2.6 compares the performance of both systems under the optimal choice of polarization vectors. It clearly shows that by retaining the 2D vector measurements, we get significantly

improved results as compared with scalar measurement systems. Even though we perform joint optimization over both the transmit and receive polarizations for the scalar measurement systems, we are still finding just the best linear combination of the two received measurements at each receiver. However, combining them linearly need not be the overall optimal solution and we might be losing some important information by doing so. This can be avoided by retaining the vector measurements, thereby giving better performance as demonstrated in Figure 2.6.

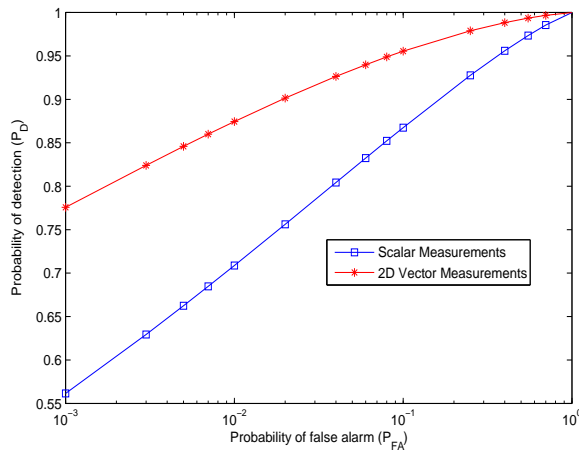


Figure 2.6: Comparison of performance between systems with scalar measurements and those with 2D vector measurements as a function of the probability of false alarm when $\sigma^2 = 0.1$.

Figure 2.7 shows the performance of both systems as a function of the noise variance when P_{FA} is fixed to a constant value of 0.02. At higher noise variances (lower signal-to-noise ratios), the improvement offered by retaining the 2D vector measurements becomes even more evident.

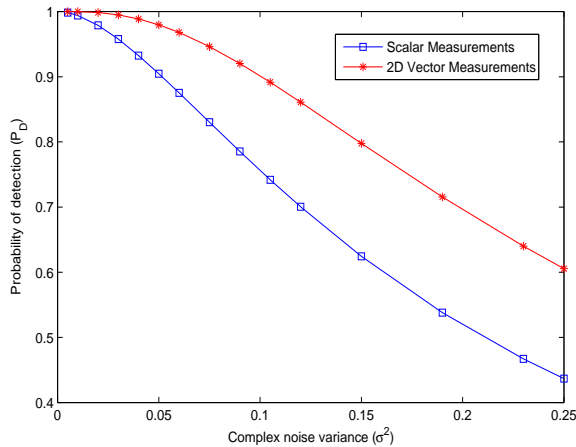


Figure 2.7: Comparison of performance between systems with scalar measurements and those with 2D vector measurements as a function of the noise variance when $P_{FA} = 0.02$.

2.7 Summary

We have proposed a radar system that combines the advantages of MIMO radar with distributed antennas and polarimetric radar at the same time. The proposed system uses two-dimensional vector sensors at each of the receivers, measuring both the horizontal and vertical components of the received signal. We dealt with the problem of target detection for such a system. We designed the well-known Neyman-Pearson detector for this problem and also analyzed the performance of the detector by obtaining approximate expressions for the probabilities of false alarm and detection. We developed a similar mathematical model for the conventional systems that combine the two received signals linearly and coherently to give only a scalar measurement at the receiver. Using numerical examples, we showed that the optimal selection of the polarizations gives significant improvement in performance over conventional systems using only horizontal or vertical polarizations all the time across all the antennas. We

showed that the performance improves by employing multiple widely separated antennas. We also demonstrated that retaining the 2D vector measurements enhances the performance of the proposed polarimetric MIMO radar system, especially at low signal-to-noise ratios.

Chapter 3

Game Theoretic Design for Polarimetric MIMO Radar Target Detection²

3.1 Introduction

The conventional approaches to polarimetric waveform design for radar systems rely on obtaining accurate estimates of the target properties from the measured data as we mentioned in the previous chapter. The improvement in performance is very sensitive to the accuracy of these estimates. Hence, we need large amounts of training data for the design scheme to be meaningful, which can be expensive. In this chapter, we propose a polarimetric design scheme for distributed MIMO radar target detection that does not depend on the training data (see also [24], [25], [26]). Using a game theoretic framework, we formulate the selection of transmit polarizations, by examining the impact of all possible transmit schemes on the different available target profiles.

²Based on S. Gogineni and A. Nehorai, “Game theoretic design for polarimetric MIMO radar target detection,” *Signal Processing*, to appear in. ©[2011] Elsevier.

This approach does not require accurate estimation of target properties from measured data and hence it can be implemented in practice without much cost unlike conventional approaches as mentioned above. This is the prime motivation for our work.

We will formulate the radar design problem as a game between the opponent and the radar design engineer. This approach utilizes the knowledge about the goals of both the players. However, conventional optimization approaches featuring cost functions that are a weighted summation of individual costs corresponding to different target profiles ignore knowledge about the goal of the opponent. This is another motivation for our proposed game theoretic framework. The game theoretic framework that we develop in this chapter is very general and can be applied to other radar waveform design problems also. Typically waveforms are expressed in parametric form like chirps, frequency hopping codes, etc. We can always divide these parameters into classes of categories and apply the same approach that we will present here.

3.2 Game Theory Background

A normal form game consists of three components: set of players, their strategies, and the players' payoff/utility functions [27], [28]. The radar design problem consists of only two players; player 1 is the opponent who chooses the target and its properties, player 2 is the radar design engineer who selects the different transmit waveform polarizations. We assume that players 1 and 2 have sets of R and Q possible pure strategies to choose from: $\mathcal{S} = \{s_1, \dots, s_R\}$ and $\mathcal{R} = \{r_1, \dots, r_Q\}$. Each of the players chooses one strategy from their corresponding set of possible strategies. Denote s and r as the pure strategies chosen by the two players. Then (s, r) denotes the

profile of actions by the players. For each of the possible profiles, we define utility functions u_1 and u_2 for the players. Note that the utility/payoff function for a player is dependent not just on his action but also on the action of the other player.

The goal for the players is to choose strategies that maximize their own payoff functions. However, since they do not have control over the actions of other player, this goal is difficult to achieve in practice. Some strategies for certain players are dominated by the others for all choices of strategies made by the other players and hence they can be eliminated from the list of possible strategies. In a two player game, a strategy r_i for player 2 is said to be dominated strictly by a strategy r_j of the same player if [27]

$$u_2(s_k, r_j) > u_2(s_k, r_i), \forall k = 1, \dots, R. \quad (3.1)$$

When the above conditions are satisfied, player 2 can eliminate r_i from the set of possible strategies because it is a strictly dominated strategy. After this, we go to the next iteration to search for strictly dominated strategies in the set of remaining possible strategies. We follow the same procedure iteratively to remove all the dominated strategies. However, this approach might not always work because strictly dominated strategies do not always exist in all the iterations. The Nash equilibrium is an alternate approach that can be considered in such scenarios.

A pure strategy Nash equilibrium is a profile of strategies such that the strategy for each player is an optimal response to the strategy of the other player. In other words, (s_i, r_j) is a Nash equilibrium if

$$u_1(s_i, r_j) \geq u_1(s_k, r_j), \forall k = 1, \dots, R, \quad (3.2)$$

$$u_2(s_i, r_j) \geq u_2(s_i, r_k), \forall k = 1, \dots, Q. \quad (3.3)$$

Therefore, if player 2 chooses r_j , then s_i is an optimal strategy for player 1 and vice versa.

A mixed strategy is specified by providing probability distributions over all the pure strategies for both the players separately [27]. Let a mixed strategy profile for both the players be given by

$$\mathcal{P}_1 = \{\mathcal{P}_1(s_1), \dots, \mathcal{P}_1(s_R)\}, \quad (3.4)$$

$$\mathcal{P}_2 = \{\mathcal{P}_2(r_1), \dots, \mathcal{P}_2(r_Q)\}. \quad (3.5)$$

Note that $\sum_{k=1}^R \mathcal{P}_1(s_k) = 1$ and $\sum_{k=1}^Q \mathcal{P}_2(r_k) = 1$. The player 1 utility function is defined as

$$u_1(\mathcal{P}_1, \mathcal{P}_2) = \sum_{\substack{i=1, \dots, R \\ j=1, \dots, Q}} \mathcal{P}_1(s_i) \mathcal{P}_2(r_j) u_1(s_i, r_j). \quad (3.6)$$

Further, we define

$$u_1(\mathcal{P}_1, r_j) = \sum_{i=1, \dots, R} \mathcal{P}_1(s_i) u_1(s_i, r_j), \quad (3.7)$$

and

$$u_1(s_i, \mathcal{P}_2) = \sum_{j=1, \dots, Q} \mathcal{P}_2(r_j) u_1(s_i, r_j). \quad (3.8)$$

The player 2 utility function is also defined using a similar approach. $(\mathcal{P}_1, \mathcal{P}_2)$ is a Nash equilibrium if

$$u_1(\mathcal{P}_1, \mathcal{P}_2) \geq u_1(s_k, \mathcal{P}_2), \forall k = 1, \dots, R, \quad (3.9)$$

$$u_2(\mathcal{P}_1, \mathcal{P}_2) \geq u_2(\mathcal{P}_1, r_k), \forall k = 1, \dots, Q. \quad (3.10)$$

The above definition implies that for any other mixed strategies $\widetilde{\mathcal{P}}_1$ and $\widetilde{\mathcal{P}}_2$, by averaging across the pure strategies on the right hand side, we obtain

$$u_1(\mathcal{P}_1, \mathcal{P}_2) \geq u_1(\widetilde{\mathcal{P}}_1, \mathcal{P}_2), \quad (3.11)$$

$$u_2(\mathcal{P}_1, \mathcal{P}_2) \geq u_2(\mathcal{P}_1, \widetilde{\mathcal{P}}_2). \quad (3.12)$$

For any given problem, the Nash equilibrium need not be unique, and we might end up with a set of Nash equilibria. At the same time, the existence of a pure strategy Nash equilibrium is not guaranteed for all the games. However, for a game with a finite number of pure strategies, the existence of a mixed strategy Nash equilibrium was shown in [29]. We will see later that our MIMO radar design problem can be reduced to a set of finite games for each transmitter, and hence the existence of an equilibrium is always guaranteed. In the next section, we will formulate the radar design problem using game theoretic framework, and in the numerical simulations, we will solve it by using well known methods like iterated strict dominance and Nash equilibrium, as we discussed in this section.

3.3 Polarimetric Design

3.3.1 Problem Formulation

We begin with a description of a distributed MIMO radar system. Let M and N denote the number of widely separated transmit and receive antennas, respectively. Each of the transmitters is capable of transmitting a waveform of any arbitrary polarization, and each receiver employs 2D vector sensors that capture both the horizontal

and vertical components of the received EM wave separately (see also [13]). Let $\mathbf{t}^i = [t_h^i, t_v^i]^T$ denote the polarization of the waveform sent out of the i^{th} transmit antenna. $\{\cdot\}^T$ denotes the transpose of $\{\cdot\}$. The subscripts h and v denote the horizontal and vertical polarization components of the i^{th} transmitter respectively; t_h^i and t_v^i are complex numbers such that $\|\mathbf{t}^i\| = 1$. The complex pulse wave shape transmitted from the i^{th} transmit antenna is defined as $w^i(t)$. These polarized waves travel in space and are reflected by the target before arriving at the receivers.

We assume that the target contains multiple individual isotropic scatterers. But due to signal bandwidth constraints, the system cannot resolve these individual scatterers. Therefore, this collection of scatterers can be expressed as one point scatterer which represents the radar cross section (RCS) center of gravity of these multiple scatterers [2]. By point target, we refer to the smallest target that can be resolved by the system and we do not refer to an isotropic scatterer. The polarizations are altered during this process of reflection. The polarizations of the received signals are determined by the target scattering matrices, which can be expressed as

$$\mathbf{S}^{ij} = \begin{bmatrix} s_{hh}^{ij} & s_{hv}^{ij} \\ s_{vh}^{ij} & s_{vv}^{ij} \end{bmatrix}. \quad (3.13)$$

Due to the distributed nature of all the antennas, the scattering matrix is dependent on the transmitter and receiver pair under consideration [13]. The signals received at each of the receivers are a combination of the signals from the different transmit antennas. Let $\mathbf{y}^j(t)$ be the complex envelope of the signal received by the j^{th} receive antenna. Then, the expressions for the received signals of a polarized radar system

are given as [15], [16], [17]

$$\mathbf{y}^j(t) = \sum_{i=1}^M \mathbf{S}^{ij} \mathbf{t}^i w^i(t - \tau^{ij}) + \mathbf{e}^j(t), \quad (3.14)$$

where $\mathbf{e}^j(t)$ is the additive noise, τ^{ij} is the time delay because of propagation. Separate these signals by employing banks of matched filters using the orthogonality of the waveforms [2]. The output of the i^{th} matched filter at the j^{th} receiver is given as [13]

$$\mathbf{y}^{ij} = \mathbf{S}^{ij} \mathbf{t}^i + \mathbf{e}^{ij}, \quad (3.15)$$

where \mathbf{e}^{ij} is the additive noise. Note that both \mathbf{y}^{ij} and \mathbf{e}^{ij} are two dimensional complex vectors because each receiver employs 2D vector sensors measuring both the horizontally and vertically polarized components separately.

We assume \mathbf{e}^{ij} to be independent realizations of zero mean Gaussian random variables with variance σ^2 . \mathbf{t}^i is the design vector for each transmitter. For each transmitter-receiver pair, we stack the complex entries of the scattering matrix as

$$\mathbf{s}^{ij} = [s_{\text{hh}}^{ij}, s_{\text{hv}}^{ij}, s_{\text{vh}}^{ij}, s_{\text{vv}}^{ij}]^T. \quad (3.16)$$

Define

$$\mathbf{s}^i = [(\mathbf{s}^{i1})^T, \dots, (\mathbf{s}^{iN})^T]^T, \quad (3.17)$$

$$\mathbf{y}^i = [(\mathbf{y}^{i1})^T, \dots, (\mathbf{y}^{iN})^T]^T, \quad (3.18)$$

$$\mathbf{e}^i = [(\mathbf{e}^{i1})^T, \dots, (\mathbf{e}^{iN})^T]^T. \quad (3.19)$$

Therefore, the measurement model corresponding to the i^{th} transmitter index reduces to

$$\mathbf{y}^i = \mathbf{H}^i \mathbf{s}^i + \mathbf{e}^i, \quad (3.20)$$

where

$$\mathbf{H}^i = \text{diag} \{ \mathbf{P}^i, \dots, \mathbf{P}^i \}, \quad (3.21)$$

$$\mathbf{P}^i = \begin{bmatrix} t_h^i & t_v^i & 0 & 0 \\ 0 & 0 & t_h^i & t_v^i \end{bmatrix}. \quad (3.22)$$

In the above expression, $\text{diag}\{\cdot\}$ represents a block diagonal matrix whose entries are given by $\{\cdot\}$. Further, we assume \mathbf{s}^i follows zero mean Gaussian distribution with covariance matrix Σ^i , which depends on the type and nature of target. Different classes of targets have different Σ^i , and we do not know the true value of Σ^i in advance. However, we assume knowledge about the list of all possible target classes. Assume there are a total of R target classes

$$\Xi^i = \{ \Sigma_1^i, \dots, \Sigma_R^i \}. \quad (3.23)$$

Note that these target classes differ only in the scattering covariance matrices. Since this is a detection problem, we test the presence of a target within a particular cell whose location is always known to the radar [1], [2]. Since, this testing cell is the same for all the target classes, we do not need to differentiate them in terms of the target locations.

Player 1 (opponent) selects one of the R possible target classes, and player 2 (design engineer) does not have knowledge about the true target class. Player 2 can obtain knowledge about the target class by performing experiments using training data, but

this can be expensive and time consuming. Instead, we propose an approach in which player 2 chooses a strategy by studying the list of all possible target classes and their implications for the radar system's performance. The pure strategies for player 2 are the choices of different transmit waveform polarizations. Since the transmitted waveforms are assumed to be mutually orthogonal for all delays, \mathbf{y}^i does not depend on \mathbf{t}^j , when $i \neq j$. Therefore, we can consider the design problem for each of the M different transmit antennas separately. Further, we assume that each transmitter has Q possible pure strategies (waveform polarizations)

$$\Omega^i = \{\mathbf{t}_1^i, \dots, \mathbf{t}_Q^i\}. \quad (3.24)$$

Now, we have finished formally defining the players and their pure strategies. The next step is to define the payoff functions of both the players for the $R \times Q$ possible profiles of strategies.

We consider that the payoff functions of both the players sum to zero. This is a reasonable assumption because the goals of both players are quite opposite. While player 1 tries to select a target class that is the most difficult to detect, player 2 will try to design the transmit waveform polarizations to improve the target detection performance. Such games, zero-sum games, have been discussed widely in game theory literature [27], [30]. Therefore, in our radar problem,

$$u_1(\boldsymbol{\Sigma}_k^i, \mathbf{t}_l^i) = -u_2(\boldsymbol{\Sigma}_k^i, \mathbf{t}_l^i), \forall k = 1, \dots, R, l = 1, \dots, Q. \quad (3.25)$$

We define the utility function corresponding to the i^{th} transmitter for player 2 as

$$u_2(\boldsymbol{\Sigma}_k^i, \mathbf{t}_l^i) = E \left\{ \|\mathbf{H}_l^i \mathbf{s}_k^i\|^2 \right\}, \quad (3.26)$$

$$= \text{tr} \left\{ \mathbf{H}_l^i E \left\{ \mathbf{s}_k^i \mathbf{s}_k^{iH} \right\} \mathbf{H}_l^{iH} \right\}, \quad (3.27)$$

$$= \text{tr} \left\{ \mathbf{H}_l^i \boldsymbol{\Sigma}_k^i \mathbf{H}_l^{iH} \right\}. \quad (3.28)$$

where $E\{\cdot\}$, $\{\cdot\}^H$ and $\text{tr}\{\cdot\}$ stand for the expectation, Hermitian, and trace of $\{\cdot\}$, respectively. If the players choose the mixed strategy profile $(\mathcal{P}_1, \mathcal{P}_2)$, then the corresponding utility function becomes

$$u_2(\mathcal{P}_1, \mathcal{P}_2) = \sum_{\substack{k=1, \dots, R \\ l=1, \dots, Q}} \mathcal{P}_1(\boldsymbol{\Sigma}_k^i) \mathcal{P}_2(\mathbf{t}_l^i) \text{tr} \left\{ \mathbf{H}_l^i \boldsymbol{\Sigma}_k^i \mathbf{H}_l^{iH} \right\}. \quad (3.29)$$

These expressions for the utility functions denote the received energy across all receivers corresponding to the i^{th} transmitter. So, the goal of each transmitter would be to maximize its utility and thereby improve the received signal energy. Note that \mathbf{H}_l^i is a function of the strategy \mathbf{t}_l^i chosen by player 2. Maximizing the received signal energy improves the detectability of the target. This is the goal of player 2. However, player 1 has the exact opposite goal of minimizing the detectability of the target. Therefore, the utilities of player 1 are defined as the additive inverse of the utilities of player 2, thereby leading to the zero-sum game.

To incorporate other mission considerations along with the detectability, we just need to modify the utility functions. The framework that we developed is very general and can be easily applied even for other scenarios. For example, our current definition of utility function considers the received signal energy. The opponent tries to minimize it. However, for someone designing the shape of the waveform, there may be other

issues like peak-to-average power ratio, etc that should be considered while designing the waveforms. In such a scenario, we can define a new utility function that puts weighted penalties for different mission considerations. This approach allows the use of this framework in diverse scenarios.

3.3.2 Solution

So far, we have expressed the problem of polarimetric waveform design using a zero-sum game. Different approaches can be used to solve this problem. As mentioned earlier, we can follow the procedure of iterated strict dominance. In each iteration, we look for the strategies that are strictly dominated by one or many of the other strategies, and remove them from the choices of possible strategies. However, the existence of such dominated strategies is not guaranteed in each iteration. If this procedure does not provide a solution, we will look for the possible Nash equilibria for this game and pick a solution from them. For finite games, the existence of a Nash equilibrium has been shown in literature [29]. Hence, we can always find at least one equilibrium solution to our design problem.

This game theoretic design is a one-time offline computation before the radar detection scan. Conventional design is done online within a particular scan while gathering training data, thereby making complexity a critical issue. The complexity of game-theoretic design depends only on the number of transmitters and the number of available profiles. This number is typically very small when compared with the dimensions of the training data required by conventional approaches. Further, computing the Nash equilibrium of any two-player zero-sum game can be formulated as a

linear programming problem and hence there exist algorithms to solve it in polynomial time [31], [32]. Hence, our approach is less complex and easy to implement.

3.4 Numerical Simulations

In this section, we will present numerical examples to demonstrate the performance of the proposed game theoretic design mechanism and compare it with purely horizontally or vertically polarized radar systems. First, we will present an example which gives a pure strategy Nash equilibrium solution to the design game. Later, we will also discuss a scenario in which the only possible Nash equilibrium solution is a mixed strategy. We are detecting the presence of a point-like target in the area illuminated by the radar. The simulated radar system consists of two transmit and two receive antennas that are widely separated and hence view the target from different angles. Therefore, the goal is to design two transmit polarization vectors that will enhance the target detection performance of the MIMO radar system. We define the unit norm complex design polarization vectors as

$$\mathbf{t}^1 = [t_h^1, t_v^1]^T, \quad (3.30)$$

$$\mathbf{t}^2 = [t_h^2, t_v^2]^T. \quad (3.31)$$

Therefore, we need to solve two games, each corresponding to a different transmit antenna. For each of the transmitters, we consider the following five possible strategies:

$$\mathbf{t}_1^i = [1, 0], \quad (3.32)$$

$$\mathbf{t}_2^i = [0, 1], \quad (3.33)$$

$$\mathbf{t}_3^i = [0.5 + \sqrt{-0.5}, 0.5 + \sqrt{-0.5}], \quad (3.34)$$

$$\mathbf{t}_4^i = [0.6 + \sqrt{-0.6}, 0.37 + \sqrt{-0.37}], \quad (3.35)$$

$$\mathbf{t}_5^i = [0.37 + \sqrt{-0.37}, 0.6 + \sqrt{-0.6}]. \quad (3.36)$$

The first two strategies correspond to using only the horizontal and vertical polarized waveforms from the transmitters, respectively. The waveforms corresponding to the other strategies contain both horizontally and vertically polarized components.

The reflection properties of the target are given by the scattering matrices corresponding to the different transmitter–receiver pairs. The statistical properties of these scattering coefficients are defined by the two covariance matrices Σ^1 and Σ^2 . We chose these covariance matrices to be of the following block diagonal structure for $i \in \{1, 2\}$. Each of the blocks corresponds to a different receive antenna index.

$$\Sigma^i = \begin{bmatrix} \Sigma^{i1} & \mathbf{0} \\ \mathbf{0} & \Sigma^{i2} \end{bmatrix}. \quad (3.37)$$

The block diagonal structure of these covariance matrices is a result of the wide separation between the receive antennas. Since the views of the target are from different angles, the corresponding target scattering coefficients will be independent.

We assume that Σ^1 is chosen by the opponent from a set of two possible target classes. The non-zero blocks of the covariance matrix Σ^1 corresponding to the first transmitter and first target class are

$$\Sigma_1^{11} = \begin{bmatrix} 0.8 & 0.05\epsilon & 0.05\epsilon & 0.04\epsilon \\ 0.05\epsilon^* & 0.4 & 0.03\epsilon & 0.03\epsilon \\ 0.05\epsilon^* & 0.03\epsilon^* & 0.3 & 0.03\epsilon \\ 0.04\epsilon^* & 0.03\epsilon^* & 0.03\epsilon^* & 0.5 \end{bmatrix}, \quad (3.38)$$

$$\Sigma_1^{12} = \begin{bmatrix} 0.5 & 0.03\epsilon & 0.04\epsilon & 0.05\epsilon \\ 0.03\epsilon^* & 0.7 & 0.02\epsilon & 0.03\epsilon \\ 0.04\epsilon^* & 0.02\epsilon^* & 0.6 & 0.02\epsilon \\ 0.05\epsilon^* & 0.03\epsilon^* & 0.02\epsilon^* & 0.3 \end{bmatrix}. \quad (3.39)$$

The non-zero blocks of the covariance matrix Σ^1 corresponding to the first transmitter and second target class are

$$\Sigma_2^{11} = \begin{bmatrix} 0.7 & 0.03\epsilon & 0.04\epsilon & 0.04\epsilon \\ 0.03\epsilon^* & 0.8 & 0.04\epsilon & 0.05\epsilon \\ 0.04\epsilon^* & 0.04\epsilon^* & 0.6 & 0.04\epsilon \\ 0.04\epsilon^* & 0.05\epsilon^* & 0.04\epsilon^* & 0.4 \end{bmatrix}, \quad (3.40)$$

$$\Sigma_2^{12} = \begin{bmatrix} 0.2 & 0.04\epsilon & 0.03\epsilon & 0.05\epsilon \\ 0.04\epsilon^* & 0.4 & 0.02\epsilon & 0.03\epsilon \\ 0.03\epsilon^* & 0.02\epsilon^* & 0.6 & 0.04\epsilon \\ 0.05\epsilon^* & 0.03\epsilon^* & 0.04\epsilon^* & 0.8 \end{bmatrix}. \quad (3.41)$$

Similarly, Σ^2 is also chosen by player 1 from a set of two possible target classes. The non-zero blocks of the covariance matrix Σ^2 corresponding to the second transmitter and first target class are given as

$$\Sigma_1^{21} = \begin{bmatrix} 0.3 & 0.03\epsilon & 0.04\epsilon & 0.04\epsilon \\ 0.03\epsilon^* & 0.5 & 0.03\epsilon & 0.05\epsilon \\ 0.04\epsilon^* & 0.03\epsilon^* & 0.2 & 0.04\epsilon \\ 0.04\epsilon^* & 0.05\epsilon^* & 0.04\epsilon^* & 0.4 \end{bmatrix}, \quad (3.42)$$

$$\Sigma_1^{22} = \begin{bmatrix} 0.7 & 0.02\epsilon & 0.04\epsilon & 0.04\epsilon \\ 0.02\epsilon^* & 0.4 & 0.03\epsilon & 0.03\epsilon \\ 0.04\epsilon^* & 0.03\epsilon^* & 0.5 & 0.05\epsilon \\ 0.04\epsilon^* & 0.03\epsilon^* & 0.05\epsilon^* & 0.3 \end{bmatrix}. \quad (3.43)$$

The non-zero blocks of the covariance matrix Σ^2 corresponding to the second transmitter and second target class are

$$\Sigma_2^{21} = \begin{bmatrix} 0.5 & 0.05\epsilon & 0.05\epsilon & 0.04\epsilon \\ 0.05\epsilon^* & 0.8 & 0.05\epsilon & 0.03\epsilon \\ 0.05\epsilon^* & 0.05\epsilon^* & 0.2 & 0.02\epsilon \\ 0.04\epsilon^* & 0.03\epsilon^* & 0.02\epsilon^* & 0.5 \end{bmatrix}, \quad (3.44)$$

$$\Sigma_2^{22} = \begin{bmatrix} 0.3 & 0.04\epsilon & 0.05\epsilon & 0.05\epsilon \\ 0.04\epsilon^* & 0.6 & 0.02\epsilon & 0.05\epsilon \\ 0.05\epsilon^* & 0.02\epsilon^* & 0.8 & 0.03\epsilon \\ 0.05\epsilon^* & 0.05\epsilon^* & 0.03\epsilon^* & 0.9 \end{bmatrix}, \quad (3.45)$$

where $\epsilon = 1 + \sqrt{-1}$.

However, the radar system does not know which of these different possible scattering matrices corresponds to the actual target. Hence, the radar must consider all the possible target scenarios before designing the transmit wave polarizations for each of the two transmit antennas. Given the above sets of possible strategies for each player, the next step remaining in defining the games is computing the utility functions for different profiles. There are $2 \times 5 = 10$ profiles in this problem, and we compute the utility functions for both the players using the expressions mentioned in the previous section.

Table 3.1: Game corresponding to transmitter 1.

Strategies	\mathbf{t}_1^1	\mathbf{t}_2^1	\mathbf{t}_3^1	\mathbf{t}_4^1	\mathbf{t}_5^1
Σ_1^1	2.2	1.9	3.27	3.28	3.1
Σ_2^1	2.1	2.4	3.6	3.46	3.55

Table 3.2: Game corresponding to transmitter 2.

Strategies	\mathbf{t}_1^2	\mathbf{t}_2^2	\mathbf{t}_3^2	\mathbf{t}_4^2	\mathbf{t}_5^2
Σ_1^2	1.7	1.6	2.67	2.66	2.57
Σ_2^2	1.8	2.8	3.66	3.36	3.77

The two games corresponding to the two transmitters are given in tables 3.1 and 3.2, where we specify the utilities corresponding to player 2. The utilities for player 1 are easily obtained using the zero-sum property of these games. We shall begin by considering game 1, which corresponds to the selection of polarizations for transmitter 1. We observe that the player 2 strategies \mathbf{t}_1^1 , \mathbf{t}_2^1 , and \mathbf{t}_5^1 are strictly dominated by the other two strategies. Similarly, for game 2, the strategies \mathbf{t}_1^2 , \mathbf{t}_2^2 , and \mathbf{t}_4^2 are dominated by the other two strategies. Therefore, after eliminating these dominated strategies, we arrive at the transformed games shown in tables 3.3 and 3.4.

Table 3.3: Game corresponding to transmitter 1 after removing player 2 dominated strategies.

Strategies	t_3^1	t_4^1
Σ_1^1	3.27	3.28
Σ_2^1	3.6	3.46

Table 3.4: Game corresponding to transmitter 2 after removing player 2 dominated strategies.

Strategies	t_3^2	t_5^2
Σ_1^2	2.67	2.57
Σ_2^2	3.66	3.77

If we assume that player 1 is knowledgeable and has information about the utility functions based on the locations and configuration of the radar system, then he will always choose the target to be from the first class, because both Σ_1^1 and Σ_2^1 give lesser utility to player 2 (higher utility for the opponent) under both the available strategies for player 2. Therefore, assuming player 1 makes a knowledgeable decision, player 2 selects t_4^1 as the polarization for the first transmit antenna and t_3^2 as the polarization for the second transmit antenna.

In higher dimensional problems, it might not always be feasible to find the dominated strategies iteratively and obtain the solution. In such a situation, we can directly compute the Nash equilibria for the games. Using Gambit [33] software for game theory, we observe that here, for both the games, there exists only one equilibrium profile, (t_4^1, Σ_1^1) for the first game and (t_3^2, Σ_1^2) for the second. Note that these are pure strategy profiles. These solutions are exactly same as the solutions obtained through iterated strict dominance. However, the solutions obtained using any of these procedures need not be unique in all situations, and we might indeed obtain a set of solutions, each of which can be an equally good strategy profile in the sense of

achieving the equilibrium. In such a situation, we assume that there is a mechanism in place to ensure that both the players expect the same equilibrium [27].

We need to rank all the possible profiles so that each player will pick the strategy that corresponds to the highest ranked profile among the multiple Nash Equilibria. Both players should use the same ranking order. So, we assume there is always a common predefined ranking order used by both the players. Note that the ranks of the profiles that are not part of the Nash equilibrium will not be considered while making the decision. There hasn't been a general argument in game theory literature that will guarantee this mechanism even though some approaches like focal-power and Pareto-dominance have been considered in [27] to achieve this common mechanism for some specific problems. But, equilibrium analysis has historically been very useful in practical applications and hence it is used for solving many problems [27]. Therefore, even though there isn't a clear analytical justification in literature that this procedure will always work, it has been shown to be very useful for a wide range of problems.

Now, having obtained the transmit waveform polarizations using game theoretic design, the next step is to observe the improvement in the radar detection performance due to this design mechanism. For this, we need to analyze the performance of the optimal Neyman-Pearson detector for this radar system by studying the statistical properties of the likelihood ratio. In [13] and [14], we derived the approximate analytical expressions for the probability of detection (P_D) and the probability of false alarm (P_{FA}) of a distributed polarimetric MIMO radar system as a function of the transmit waveform polarizations while employing the optimal detector. We use these expressions to plot the performance curves of this detector, as shown in Fig. 3.1 and Fig. 3.2.

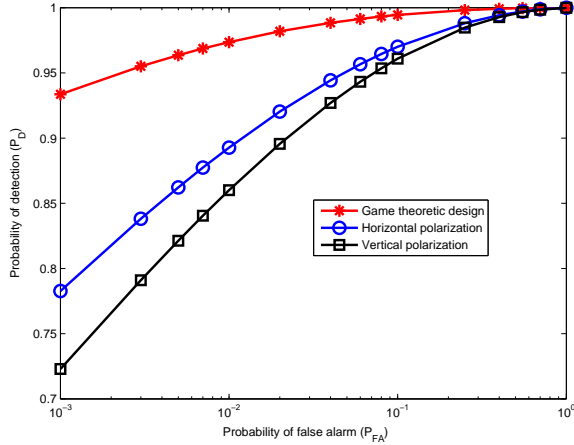


Figure 3.1: ROC curves when the complex noise variance $\sigma^2 = 0.2$.

We observe that the game theoretic design of transmit waveform polarizations gives significant improvement in performance when compared with systems which transmit only horizontally or vertically polarized waveforms. In these simulations, we assume the noise samples to be obtained from zero mean complex Gaussian distribution with variance σ^2 . In Fig. 3.1, we show the increase in P_D as a function of P_{FA} by plotting the receiver operating characteristics (ROC). Further, in Fig. 3.2, we also demonstrate the improvement in P_D for all values of the complex noise variance σ^2 . Further, we see that in this example, the system which transmits purely horizontally polarized waveforms outperforms the vertically polarized system. This is true only for this choice of scattering covariance matrices, and it need not always be the case.

In the above problem, the Nash equilibrium solutions to both the games were pure strategies for both the players. However, this may not be true for all other choices of covariance matrices. Thus, we will study a problem that does not have pure strategy equilibrium solutions. For example, assume that the first block of the scattering covariance matrix corresponding to the first target class in the previous problem is

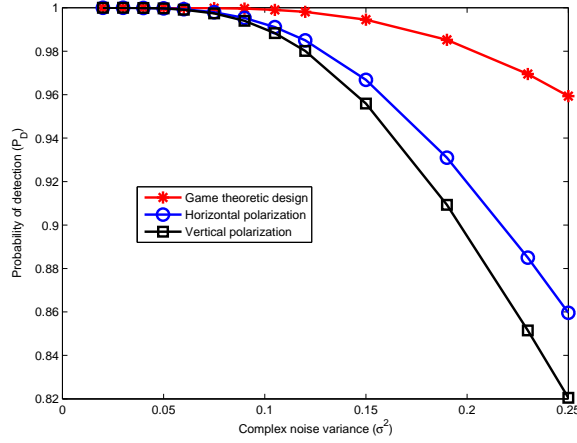


Figure 3.2: Probability of detection as a function of the noise variance when $P_{FA} = 0.02$.

changed to

$$\Sigma_1^{11} = \begin{bmatrix} 1.2 & 0.05\epsilon & 0.05\epsilon & 0.04\epsilon \\ 0.05\epsilon^* & 0.4 & 0.03\epsilon & 0.03\epsilon \\ 0.05\epsilon^* & 0.03\epsilon^* & 0.3 & 0.03\epsilon \\ 0.04\epsilon^* & 0.03\epsilon^* & 0.03\epsilon^* & 0.4 \end{bmatrix}. \quad (3.46)$$

This change affects only the utilities corresponding to the game of the first transmit antenna, and the modified 2 player game is described in table 3.5.

Table 3.5: Modified game corresponding to transmitter 1.

Strategies	t_1^1	t_2^1	t_3^1	t_4^1	t_5^1
Σ_1^1	2.6	1.8	3.5	3.61	3.21
Σ_2^1	2.1	2.4	3.6	3.46	3.55

The game corresponding to the second transmitter does not change because its corresponding covariance matrices have not been altered. Due to the modified utilities of the players, this zero-sum game does not have any pure strategy Nash equilibrium. The solution to this game is a unique mixed strategy Nash equilibrium that is given

by

$$\mathcal{P}_1 = \left\{ \frac{14}{25}, \frac{11}{25} \right\}, \quad (3.47)$$

$$\mathcal{P}_2 = \left\{ 0, 0, \frac{3}{5}, \frac{2}{5}, 0 \right\}. \quad (3.48)$$

Player 1 assigns non-zero probabilities to both his pure strategies, whereas player 2 assigns non-zero probabilities only to the pure strategies \mathbf{t}_3^1 and \mathbf{t}_4^1 . This assignment shows that the other pure strategies of player 2, namely \mathbf{t}_1^1 , \mathbf{t}_2^1 , and \mathbf{t}_5^1 , are dominated by the strategies \mathbf{t}_3^1 and \mathbf{t}_4^1 . Hence, they can be eliminated from the design problem.

In this problem, it is not straightforward to plot the ROC curves because the value of P_D will vary for the different non-dominated pure strategy pairs. We have four such pairs here, and hence we compute the constituent probabilities of detection $P_D|\Sigma_1^1, \mathbf{t}_3^1$, $P_D|\Sigma_1^1, \mathbf{t}_4^1$, $P_D|\Sigma_2^1, \mathbf{t}_3^1$, and $P_D|\Sigma_2^1, \mathbf{t}_4^1$. Based on the mixing probabilities of the Nash equilibrium, we define

$$P_D = \sum_{i=1}^2 \sum_{j=3}^4 \mathcal{P}_1(i) \mathcal{P}_2(j) P_D|\Sigma_i^1, \mathbf{t}_j^1. \quad (3.49)$$

Using this definition, we plot the ROC curves in Fig. 3.3. We observe that the mixed strategy polarimetric design outperforms the radar system with only horizontal or vertical polarizations. Also, horizontal polarization again gives better detection performance than vertical polarization. Note that even for plotting these ROC curves we combined the results corresponding to the two pure strategies of player 1, using the appropriate probabilities from the equilibrium solution. Further, in Fig. 3.4, we plotted P_D as a function of the noise variance. We notice that the mixed strategy equilibrium solution has a higher P_D for all values of the complex noise variance while maintaining a fixed P_{FA} .

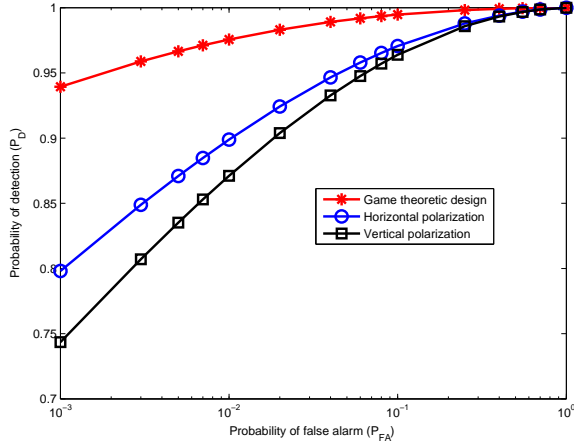


Figure 3.3: ROC curves demonstrating the improvement due to the mixed strategy solution.

3.5 Summary

We approached the problem of polarimetric waveform design for distributed MIMO radar from a game theoretic perspective. We formulated the problem in the form of a two player zero-sum game played between an opponent and the radar design engineer by defining the corresponding utility functions for both the players. This approach does not require estimation from the training data for performing the system design, and hence it can be easily implemented in a practical system. We demonstrated performance advantage of the proposed approach using numerical simulations to show the improvement in the probability of detection.

In future work, we will include the effect of clutter in our measurement model and investigate the problem of polarimetric design using the game theoretic approach we presented in this chapter. We will extend this approach to the problem of selecting optimal waveform shapes for colocated MIMO radar. Further, we will use this game theoretic framework for other radar problems including scheduling. We will extend

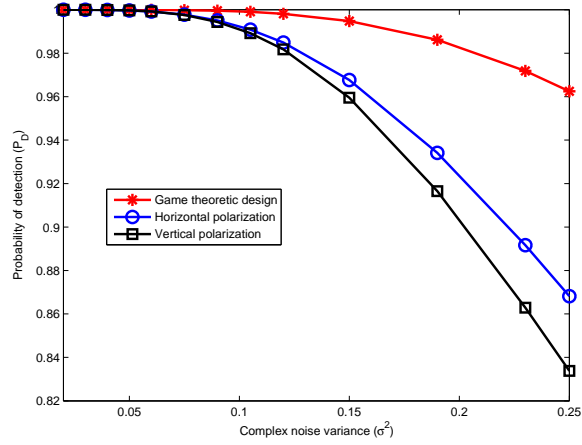


Figure 3.4: Probability of detection as a function of the noise variance when $P_{FA} = 0.02$.

our analysis to continuous-strategy games. Finally, we will also validate our results using real radar data.

Chapter 4

Monopulse MIMO Radar for Target Tracking³

4.1 Introduction

Angle tracking systems are primarily implemented using either of two main mechanisms, sequential lobing and simultaneous lobing [34], [35], [36]. In both these mechanisms, we project the radar beams slightly to either side of the radar axis in both the angular dimensions (azimuth and elevation). We compare the received signals in each of these beams to keep track of the angular position of the target. To perform this comparison, the system computes a ratio which is a function of the signals received through these beams. This ratio is called Monopulse Ratio [35]. In sequential lobing, as the name suggests, we carry out this procedure in a sequential manner by alternating between the different beams from one pulse to another. However, in simultaneous lobing, we generate all the beams at the same time. Simultaneous lobing is also called as monopulse.

³Based on S. Gogineni and A. Nehorai, "Monopulse MIMO radar for target tracking," *IEEE Trans. on Aerospace and Electronic Systems*, vol. 47, no. 1, pp. 755-768, Jan. 2011. ©[2011] IEEE.

If there are heavy fluctuations in the target returns from one time instant to another, sequential lobing suffers from a degradation in performance whereas monopulse is immune to these fluctuations because we measure the signals coming from all the beams at the same time [34], [35], [36]. Apart from this, sequential lobing also suffers from a reduction in the data rate because we need multiple pulses to receive the data from all the beams. However, the advantages offered by simultaneous lobing come at the cost of increased complexity because we need additional hardware to generate the two beams at the same time. In this chapter, we propose a distributed MIMO radar system that uses monopulse processing at the receivers (see also [37], [38]). It provides the spatial diversity offered by distributed MIMO radar and is also immune to highly fluctuating target returns just like any monopulse tracking radar.

4.2 System Description

In this section, we begin with a brief description of our proposed system. Fig. 4.1 gives the basic structure of our monopulse MIMO radar system. The system has M transmit antennas and N receive antennas. The different transmitters illuminate the target from multiple angles and the reflected signals from the surface of the target are captured by widely separated receivers. All the receivers are connected to a fusion center which can be a separate block by itself or one of the receivers can function as the fusion center. Each of the receivers generates two overlapping receive beams on either side of the boresight axis (see Fig. 4.2). Before initializing the tracking process, the fusion center makes the boresight axes of all the receivers point towards the same point in space (see Fig. 4.3). The fusion center has knowledge of the exact locations

of all the transmit and receive antennas and hence it can direct the receivers to align their respective axes accordingly.

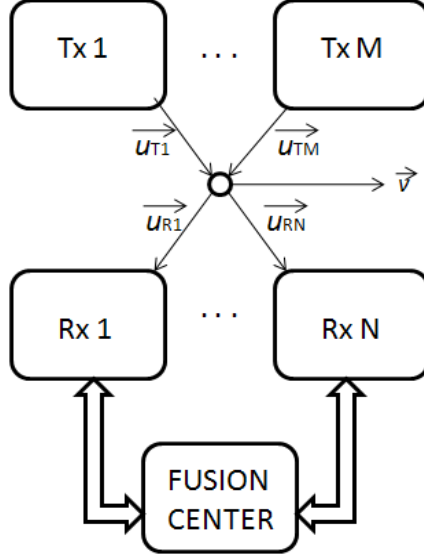


Figure 4.1: Our proposed monopulse MIMO radar system.

We assume that the target moves only in the azimuth plane scanned by these beams. However, we can easily extend this to the other angular dimension (elevation) without loss of generality by adding the extra beams. We compare the signals arriving through the two beams at each of the receivers in order to update the estimate of the angular position of the target. If the target is present to the left side of the boresight axis, then we expect the power of the signal from the left beam to be higher when compared with that from the right beam in an ideal noiseless scenario. After comparison of the signals, each receiver updates its angular estimate of the target location by appropriately moving the boresight axis. All the receivers send their new local angular estimates to the fusion center. The fusion center makes use of all the information sent to it and makes a final global decision on the location where the target could be present. It instructs all the receivers to align their boresight axes towards this estimated target location. After this processing, the receivers get ready

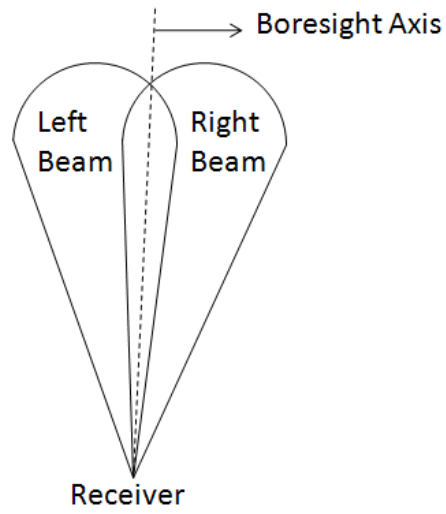


Figure 4.2: Overlapping monopulse beams at one of the receivers.

for the next iteration. We give the details of how these local and global estimates are updated in section 4.4.

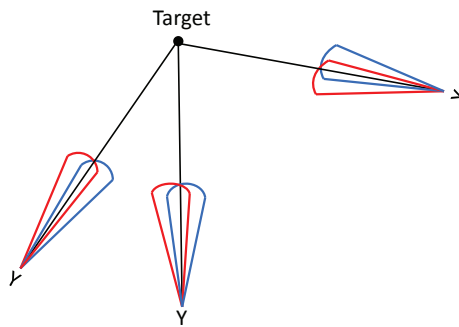


Figure 4.3: Monopulse MIMO radar receivers.

4.3 Signal Model

4.3.1 Transmitted Waveforms

As mentioned in the previous section, we assume there are M widely separated transmit antennas. Let $\tilde{s}_i(t), i = 1, \dots, M$, denote the complex baseband waveform transmitted from the i^{th} antenna. Therefore, after modulation, the bandpass signal emanating from the i^{th} transmit antenna is given as

$$s_i(t) = \text{Re} \{ \tilde{s}_i(t) e^{j2\pi f_c t} \}, \quad (4.1)$$

where $\text{Re}\{\cdot\}$ denotes the real part of the argument, $j = \sqrt{-1}$, and f_c denotes the carrier frequency. We assume that $\tilde{s}_i(t), \forall i = 1, \dots, M$ are narrowband waveforms with pulse duration T seconds. We repeat each of these pulses once every T_R seconds. We do not impose any further constraints on these waveforms. Especially, note that we do not need orthogonality between the different transmitted waveforms unlike conventional MIMO radar with widely separated antennas. As we shall see later in the chapter, the reason for this is that we do not need a mechanism to separate these waveforms at the receivers. We process the sum of the signals coming from different transmitters collectively without separating them. This is another advantage of the proposed system because the assumption that the waveforms remain orthogonal for different delays and doppler shifts is unrealistic. In section 4.5 (numerical results), we considered rectangular pulses.

4.3.2 Target and Received Signals

We assume a far-field target in our analysis. Further, we assume that the target is point like with its RCS varying with the angle of view. Hence, the signals coming from different transmitters undergo different attenuations before they travel to the receivers. Let $a_{ik}(t)$ denote the complex attenuation factor due to the distance of travel and the target RCS for the signal transmitted from the i^{th} transmitter and reaching the k^{th} receiver and τ_{ik} is the corresponding time delay. Note that for a colocated MIMO system, $a_{ik}(t)$ for different transmitter-receiver pairs will be the same because all the antennas will be viewing the target from closely spaced angles. Different models have been proposed in literature to model the time varying fluctuations in these attenuations $a_{ik}(t)$ [39], [40], [41]. Some of these models incorporate pulse-to-pulse fluctuations, scan-to-scan fluctuations, etc. These correspond to fast moving and slow moving targets respectively. In our numerical simulations, we consider a rapidly fluctuating scenario where these attenuations keep varying from one pulse instant to another because of the motion of the target. We assume $a_{ik}(t)$ to be constant over the duration of one pulse. These attenuations $a_{ik}(t)$ are not known at the receivers. The complex envelope of the signal reaching towards the k^{th} receiver is the sum of all the signals coming from different transmitters

$$\tilde{y}_k(t) = \sum_{i=1}^M a_{ik}(t) \tilde{s}_i(t - \tau_{ik}). \quad (4.2)$$

Hence, the actual bandpass signal arriving at the k^{th} receiver is

$$y_k(t) = \sum_{i=1}^M \text{Re} \{ a_{ik}(t) \tilde{s}_i(t - \tau_{ik}) e^{j2\pi f_c(t - \tau_{ik})} \}. \quad (4.3)$$

So far, we assumed the target to be stationary. When the target is moving, we modify the above equation to include the Doppler effect. Under the narrowband assumption for the complex envelopes of the transmitted waveforms, and further assuming the target velocity to be much smaller than the speed of propagation of the wave in the medium, the Doppler would not affect the component $a_{ik}(t)\tilde{s}_i(t - \tau_{ik})$ and it shows up only in the carrier component, transforming the signal to

$$y_k(t) = \sum_{i=1}^M \operatorname{Re} \left\{ a_{ik}(t)\tilde{s}_i(t - \tau_{ik})e^{j2\pi(f_c(t-\tau_{ik})+f_{Dik}(t-\tau_{ik}))} \right\}, \quad (4.4)$$

where f_{Dik} is the Doppler shift along the path from the i^{th} transmitter to the k^{th} receiver,

$$f_{Dik} = \frac{f_c}{c} (\langle \vec{v}, \vec{u}_{Rk} \rangle - \langle \vec{v}, \vec{u}_{Ti} \rangle), \quad (4.5)$$

where \vec{v} , \vec{u}_{Ti} , \vec{u}_{Rk} denote the target velocity vector, unit vector from the i^{th} transmitter to the target and the unit vector from the target to the k^{th} receiver, respectively; \langle, \rangle is the inner product operator, and c is the speed of propagation of the wave in the medium. Equation (4.4) is valid only when the target is moving with constant velocity. It is reasonable to assume uniform motion within any given processing interval because the typical duration of a processing interval is very small. If the target is accelerating and if the complex envelope is wideband, more detailed expressions can be derived using the theory in [42], [43], [44], [45]. Note that the Doppler shifts f_{Dik} are not known at the receivers.

4.3.3 Beamforming

The receive beams are generated using Capon beamformers [46], [47]. Capon beamformer is the minimum variance distortionless spatial filter. In other words, it minimizes the power of noise and signals arriving from directions other than the specific direction it was designed for. Each receiver generates two beams located at the same phase center using two linear arrays. Each array has L elements, each separated by a uniform distance of $\frac{\lambda}{2}$, where $\lambda = \frac{c}{f_c}$ is the wavelength corresponding to the carrier. Under the given antenna spacing, the steering vector of the beamformers becomes

$$\mathbf{d}(\theta, f) = \left[1, e^{-j\pi \frac{f\lambda}{c} \cos \theta}, \dots, e^{-j(L-1)\pi \frac{f\lambda}{c} \cos \theta} \right]^T, \quad (4.6)$$

where $[\cdot]^T$ denotes the transpose. Let θ_k be the angle between the approaching plane

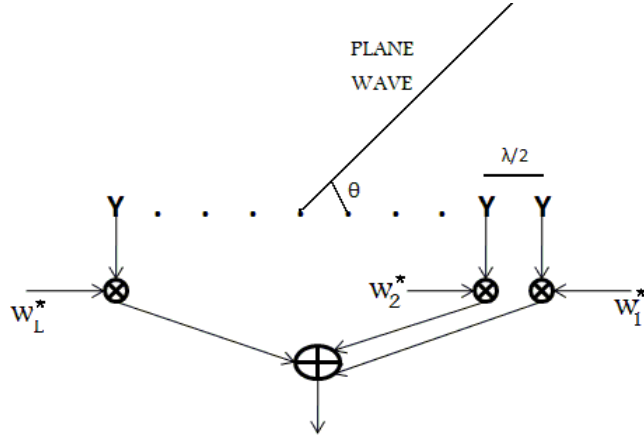


Figure 4.4: Spatial beamformer at the receiver.

wave and the two linear arrays at the k^{th} receiver (see Fig. 4.4). The received signals are first demodulated before passing through the two beamformers. Define the outputs of the two beamformers as $y_k^l(t)$ and $y_k^r(t)$, where the superscripts l and r correspond to the left and the right beams, respectively (see Fig. 4.2). Also, let

$\mathbf{w}_k^l = [w_{k1}^l, \dots, w_{kL}^l]^T$ and $\mathbf{w}_k^r = [w_{k1}^r, \dots, w_{kL}^r]^T$ denote the corresponding weight vectors of the beamformers. Similarly, $\mathbf{e}_k^l(t) = [e_{k1}^l(t), \dots, e_{kL}^l(t)]^T$ and $\mathbf{e}_k^r(t) = [e_{k1}^r(t), \dots, e_{kL}^r(t)]^T$ are the additive noise vectors of these two spatial filters. The outputs of these spatial filters become

$$\begin{aligned} y_k^l(t) &= \sum_{i=1}^M a_{ik}(t) \tilde{s}_i(t - \tau_{ik}) e^{j2\pi(f_c(-\tau_{ik}) + f_{Dik}(t - \tau_{ik}))} (\mathbf{w}_k^l)^H \mathbf{d}(\theta_k, f_c + f_{Dik}) + (\mathbf{w}_k^l)^H \mathbf{e}_k^l(t), \\ y_k^r(t) &= \sum_{i=1}^M a_{ik}(t) \tilde{s}_i(t - \tau_{ik}) e^{j2\pi(f_c(-\tau_{ik}) + f_{Dik}(t - \tau_{ik}))} (\mathbf{w}_k^r)^H \mathbf{d}(\theta_k, f_c + f_{Dik}) + (\mathbf{w}_k^r)^H \mathbf{e}_k^r(t). \end{aligned}$$

Defining

$$x_k(t) \triangleq \sum_{i=1}^M a_{ik}(t) \tilde{s}_i(t - \tau_{ik}) e^{j2\pi(f_c(-\tau_{ik}) + f_{Dik}(t - \tau_{ik}))}, \quad (4.7)$$

we get the sampled outputs as

$$y_k^l[n] = x_k[n] (\mathbf{w}_k^l)^H \mathbf{d}(\theta_k, f_c + f_{Dik}) + (\mathbf{w}_k^l)^H \mathbf{e}_k^l[n], \quad (4.8)$$

$$y_k^r[n] = x_k[n] (\mathbf{w}_k^r)^H \mathbf{d}(\theta_k, f_c + f_{Dik}) + (\mathbf{w}_k^r)^H \mathbf{e}_k^r[n]. \quad (4.9)$$

We assume that the additive noise vectors at the two arrays of sensors have zero mean and covariance matrices \mathbf{R}_k^l and \mathbf{R}_k^r , respectively. The Capon beamformer creates the beams by minimizing $(\mathbf{w}_k^l)^H \mathbf{R}_k^l \mathbf{w}_k^l$ and $(\mathbf{w}_k^r)^H \mathbf{R}_k^r \mathbf{w}_k^r$ subject to the constraints $\left\{ (\mathbf{w}_k^l)^H \mathbf{d}(\theta_k^l, f_c) = 1 \right\}$ and $\left\{ (\mathbf{w}_k^r)^H \mathbf{d}(\theta_k^r, f_c) = 1 \right\}$, respectively. The solution to this optimization problem gives the weights of the beamformers [47]

$$\mathbf{w}_k^l = \frac{(\mathbf{R}_k^l)^{-1} \mathbf{d}(\theta_k^l, f_c)}{\mathbf{d}(\theta_k^l, f_c)^H (\mathbf{R}_k^l)^{-1} \mathbf{d}(\theta_k^l, f_c)}, \quad (4.10)$$

$$\mathbf{w}_k^r = \frac{(\mathbf{R}_k^r)^{-1} \mathbf{d}(\theta_k^r, f_c)}{\mathbf{d}(\theta_k^r, f_c)^H (\mathbf{R}_k^r)^{-1} \mathbf{d}(\theta_k^r, f_c)}, \quad (4.11)$$

where θ_k^l, θ_k^r are the angles at which both the beams are directed. Hence, boresight axis of the receiver is located at an angle $\theta_k^b = \frac{\theta_k^l + \theta_k^r}{2}$. In practice, the covariance matrices \mathbf{R}_k^l and \mathbf{R}_k^r are not known at the receiver apriori. Therefore, they are approximated using the sample covariance matrices $\widehat{\mathbf{R}}_k^l$ and $\widehat{\mathbf{R}}_k^r$, respectively.

In Fig. 4.5, we plotted the response of the two spatial filters to exponential signals of frequency f_c coming from different angles. The left and the right beams are designed for signals coming from angles 80 degrees and 75 degrees, respectively with a frequency f_c . Hence, the boresight axis is at an angle of 77.5 degrees. We used an array of 10 elements to generate these beams and the beams were designed for a diagonal covariance matrix with a variance of 0.1 for the measurements. The response of these spatial filters at the boresight angle is 0.9258. We can control the widths of each of these beams by adjusting the number of elements in the linear array. A larger value of L gives a narrower beam width because of the increased degrees of freedom.

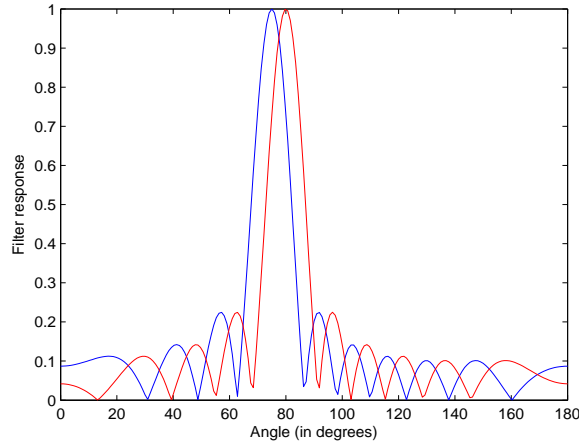


Figure 4.5: Responses of the two spatial filters as a function of the angle.

We evaluate the sum and the difference of the absolute values of the complex outputs at the two beamformers

$$y_k^s[n] = \text{abs}\{y_k^l[n]\} + \text{abs}\{y_k^r[n]\}, \quad (4.12)$$

$$y_k^d[n] = \text{abs}\{y_k^l[n]\} - \text{abs}\{y_k^r[n]\}, \quad (4.13)$$

where the superscripts s and d denote the sum and difference channels, respectively; $\text{abs}\{\cdot\}$ represents the absolute value of the complex number in the argument. Now, we send the measurements from these two channels to the monopulse processor for the decision making about the angular location of the target.

4.4 Tracking Algorithm

We propose a tracking algorithm for monopulse MIMO radar in this section.

4.4.1 Initialization

The fusion center has the information about the exact locations of all the receivers. It will initialize the tracking algorithm by making sure that the boresight axes of all the receivers intersect at the same point in space. After this, the receivers obtain the measurements from the first pulse according to equations (4.8) and (4.9).

4.4.2 Monopulse Processing: Local Angular Estimates

After obtaining the measurements from the sum and the difference channels, each of the receivers computes the monopulse ratio

$$M_k[n] = \frac{y_k^d[n]}{y_k^s[n]}. \quad (4.14)$$

If the $M_k[n]$ is positive, it implies that it is highly likely for the target to be present on the left side of the boresight axis. Similarly, a negative $M_k[n]$ indicates the opposite. The receiver k will adjust its boresight axis appropriately using the following equation

$$\theta_k^{\text{b(new)}} = \theta_k^{\text{b}} + \delta\{M_k[n]\}, \quad (4.15)$$

where δ is a positive valued design parameter. The above equation essentially increases the value of θ_k^{b} if the target is present to the left side of the axis and reduces it if the target is on the other side. The amount of increase or decrease in the angular adjustment is proportional to the monopulse ratio. The parameter δ has to be chosen carefully. A larger value of δ will enable tracking faster moving targets but will also lead to higher steady state errors. However, a smaller δ will increase the convergence time but the steady state errors will be less. Each of the receivers updates its angular estimates using the above mentioned processing. In our proposed system, we adjust the boresight axes electronically by adjusting the weights of both the beamformers. However, we can also do this by mechanically steering both the beams. The disadvantage of using mechanical steering is the delay encountered while rotating the beams. Electronic steering by beamforming is very quick and can be done instantaneously by adjusting the weights appropriately.

In Fig. 4.6, we plot the monopulse ratio formed by using the two spatial filters shown in Fig. 4.5. It can be seen that the ratio changes its sign exactly at the middle point between the two beams i.e, 77.5 degrees. The beams that we used in our numerical results have exactly the same width and same separation angle as mentioned in this example.

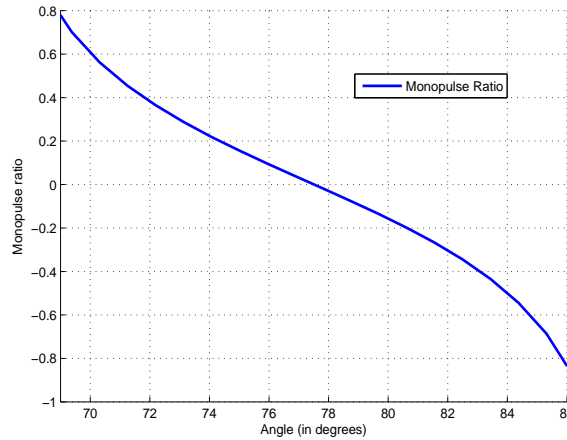


Figure 4.6: Monopulse ratio as a function of the angle.

4.4.3 Fusion Center: Global Location Estimate

The primary function of the fusion center is to combine these decentralized estimates and arrive at a global estimate for the target location. We have solved a similar problem for localizing acoustic sources using Cramer-Rao bound [48]. Here, we present a simpler method to combine the decentralized estimates. After obtaining new angular estimates, each of the receivers sends these new updates to the fusion center. Along with the angular estimates, the receivers also send the instantaneous energy of the received signal in the sum channel during that instant.

$$E_k[n] = (y_k^s[n])^2. \quad (4.16)$$

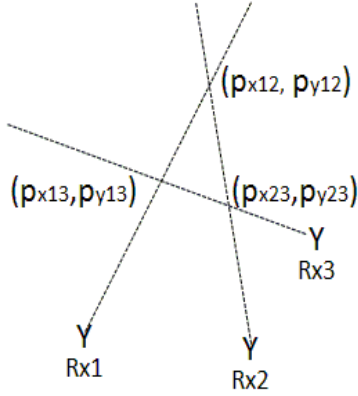


Figure 4.7: Polygon formed by the points of intersection of the boresight axes of three receivers.

The fusion center forms a polygon of $\frac{N(N-1)}{2}$ sides by connecting the points of intersection of the updated boresight axes of each of the N receivers (see Fig. 4.7). See also [49]. The fusion center will decide upon a point inside this polygon to be the global estimate of the target location. Define $(p_{x_{ij}}[n], p_{y_{ij}}[n])$ to be the cartesian coordinates of the vertex formed by the intersection of the boresight axes coming out from the i^{th} receiver and the j^{th} receiver. A linear combination of these vertices is chosen as the estimate of the target location

$$(\hat{p}_x[n], \hat{p}_y[n]) = \sum_{i=1}^N \sum_{j=i+1}^N \alpha_{ij}[n] (p_{x_{ij}}[n], p_{y_{ij}}[n]). \quad (4.17)$$

We choose the weights $\alpha_{ij}[n]$ to be proportional to the sum of instantaneous energies received from the corresponding receivers and $\sum_{i=1}^N \sum_{j=i+1}^N \alpha_{ij}[n] = 1$. Therefore,

$$\alpha_{ij}[n] = \frac{E_i[n] + E_j[n]}{\sum_{i'=1}^N \sum_{j'=i'+1}^N (E_{i'}[n] + E_{j'}[n])}. \quad (4.18)$$

These weights also depend on the locations of the transmitters and receivers relative to the target. The signal at each receiver is a sum of the signals coming from different

transmitters and bouncing off the surface of the target. Therefore, the path length and the target RCS play an important role in determining the received energies. Hence, it is highly likely that a transmitter-receiver pair which has a good look at the target and shorter path length will give a significant contribution to the instantaneous received energy at that receiver.

Finally, the fusion center sends the new estimate $(\widehat{p}_x[n], \widehat{p}_y[n])$ to all the receivers and guides them to align their axes towards this particular location before the next iteration. We summarize the important steps of the algorithm in Table 1. Note that the Doppler frequencies that appear in the expressions for the received measurements (see section 4.3) will degrade the performance of the tracking algorithm because they also impact the computation of the monopulse ratio and these frequencies are not known at the receivers. However, in certain situations, having large Doppler shifts might be an advantage. Consider an example when there is an additional target close to the target of interest. In such a scenario, if these targets have significantly different Doppler frequencies, we can separate the signals from both of them using Doppler filters if we have a rough estimate of these frequencies. Therefore, in such situations, it is useful if the Doppler shifts of the targets are far apart.

Table 4.1: Tracking algorithm

Step 1: Fusion center directs all the receivers to align their boresight axes to the same location.

Step 2: Each receiver calculates $M_k[n]$ and adjusts boresight axis to $\theta_k^{b(\text{new})} = \theta_k^b + \delta\{M_k[n]\}$.

Step 3: Receivers send $\theta_k^{b(\text{new})}$ and $E_k[n] = (y_k^s[n])^2$ to the fusion center.

Step 4: Fusion center identifies the points of intersection of these axes $(p_{x_{ij}}[n], p_{y_{ij}}[n])$ and estimates the target location to be $(\widehat{p}_x[n], \widehat{p}_y[n]) = \sum_{i=1}^N \sum_{j=i+1}^N \alpha_{ij}[n] (p_{x_{ij}}[n], p_{y_{ij}}[n])$, where $\alpha_{ij}[n] = \frac{E_i[n] + E_j[n]}{\sum_{i'=1}^N \sum_{j'=i'+1}^N (E_{i'}[n] + E_{j'}[n])}$.

Step 5: Fusion center directs all the receivers to point their boresight axes to this new estimate $(\widehat{p}_x[n], \widehat{p}_y[n])$ and we start again with step 2.

4.4.4 Multiple Targets

The scenario in which multiple targets are present in the illuminated scene is of interest. If we have more than a single target, the tracking algorithm might end up pointing towards neither of the actual targets. It could be pointing towards some region in between these targets. The multi-target problem has been addressed in [50], [51], [52], [53], [54], [55]. [50] studies the varieties of monopulse responses to multiple targets. The problem of estimation of the direction of arrival is studied in [52], in the context of two unresolved Rayleigh targets. In [54], the authors exploit the Doppler separation between the targets to perform the tracking of the intended target in the presence of the interfering target. These different techniques can be applied at each of the receivers in our proposed system. Also, we use electronic steering for rotating the beams at the receivers. Hence, this can be done instantaneously without much delay. This is in contrast with mechanical steering that will have some lag. This helps us to continue to keep track of the multiple moving targets even when they move into different range bins. We can quickly switch the receive beams from one angle to another as we move from one range bin to another. Thus, the point of intersection of the boresight axes of the receivers (see Fig. 4.3) can be made to change from one range bin to another. Also, we can apply Doppler processing to separate the targets in a similar manner as it is done for SISO monopulse radar.

4.5 Numerical Results

4.5.1 Simulated Scenario

In this section, we demonstrate the advantage of the proposed monopulse MIMO tracking system under realistic scenarios. We simulated such a scenario to demonstrate the advantages of this system. First, we describe the locations of the transmitters, receivers, and target on a cartesian coordinate system. The simulated system has two transmitters that are located on the y-axis at distances of 20km and 40km from the origin, respectively. There are three receivers located on the x-axis at the origin, 20km and 40km from the origin, respectively. The receiver at the origin also serves as the fusion center for this setup. The target is initially present at the coordinate (30, 35). Fig. 4.8 shows the simulated radar-target scenario.

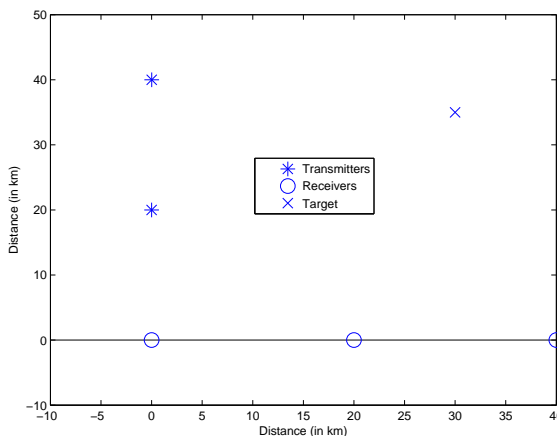


Figure 4.8: Simulated radar-target scenario.

We chose the carrier frequency $f_c = 1\text{GHz}$. We used complex rectangular pulses each with a constant value $\frac{1+\sqrt{-1}}{\sqrt{2}}$ and bandwidth 100MHz for the transmitted baseband

waveforms. Therefore, the pulse duration $T = 10^{-8}$ s. The pulses coming from different transmitters reach the receivers in different intervals of time because of the different delays caused by the distances between them. The processing remains the same even if the square pulses from different transmit antennas overlap because we are only interested in the ratio of the signals in the difference and the sum channels i.e., we do not need a mechanism to separate these pulses. The pulse repetition interval $T_R = 4$ ms. We further had two samples per pulse duration (Nyquist rate). We ran the simulation for 2s. Hence, we had 500 pulses from each transmitter. The target is airborne and moving with a constant velocity of $(0.25, 0.25)$ km/s. There are six complex numbers $\{a_{11}, a_{12}, a_{13}, a_{21}, a_{22}, a_{23}\}$ describing the attenuation experienced by the signals. It is important to realistically model these attenuations. They were independently generated from one pulse to another using zero mean complex normal random variables with their variances chosen from the set $\{0.15, 0.3, 0.45, 0.6, 0.75, 0.9\}$. The a_{ik} corresponding to the antenna pair that are the closest to the target got the higher values and vice versa. We assumed the additive noise at every element of the receiver array is uncorrelated zero mean complex Gaussian distributed with variance σ^2 . The received powers are different at different receivers because the attenuations a_{ik} do not have the same variances. Therefore, we evaluate the overall signal to noise ratio (SNR) by computing the average. For a noise variance of $\sigma^2 = 0.1$, SNR=12.3dB. We further assumed the noise to be stationary. The noise variance was estimated from a training data set of 50 samples. We assumed that the target returns were not present in the training samples that were used. We independently generated the noise from one time sample to another. The two beams at each receiver were generated using $L = 10$ element linear arrays and they were made to point 5 degrees on either side of the boresight axis. The -3 dB beamwidth of these beams is approximately 12 degrees. We chose the parameter $\delta = 0.25$ degrees in our algorithm.

4.5.2 Spatial Diversity

We first demonstrate the spatial diversity offered by monopulse MIMO radar with widely separated antennas by comparing this system with monopulse SISO radar. Since a single receiver monopulse tracking radar can only track the angular location of the target, we shall compare only the angle errors of the SISO and MIMO monopulse radars. For SISO radar, we assumed only the first transmitter $(0, 20)$ and the first receiver $(0, 0)$ (see Fig. 4.8) to be present. First, we assumed that the initial estimate of the target location for 2x3 MIMO radar is far from the actual location at $(32, 32)$. Hence, the initial estimate was at a distance of 3.61km from the actual location. The same initial estimate was also used for SISO radar and it corresponds to an initial angular error of 4.3987 degrees. In order to make the comparison fair, we deliberately increased the transmit power per antenna for the SISO system to make the overall transmit power the same. We chose the complex noise variance σ^2 for this comparison to be 0.1. We plotted the angular error as a function of the pulse index. Fig. 4.9 shows that the MIMO system overcomes a poor initial estimate and manages to track down the target much quicker than the SISO radar. The SISO system takes 60 pulses to come within an angular error of 1 degree. However, the 2x3 MIMO system takes only 20 pulses to reach within the same level of angular error. To obtain good accuracy, we plotted these curves by averaging the results over 100 independent realizations.

Next, we assumed a good initial estimate of $(29.9, 34.9)$ and plotted the average angular errors of both these systems as a function of the complex noise variances. As expected, Fig. 4.10 shows that the average angular error increases with an increase in the noise variance. MIMO system significantly outperforms the SISO system. The angular error of these systems can further be reduced by using a smaller value of δ . However, if the initial estimate of the target location is poor, a smaller δ would

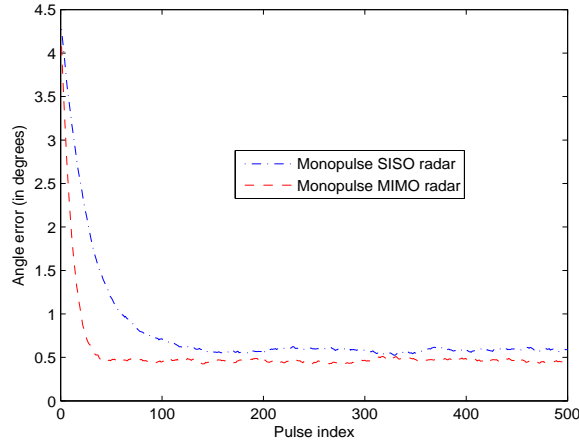


Figure 4.9: Comparing the angle error of SISO and MIMO monopulse radars as a function of the pulse index for $\sigma^2 = 0.1$.

mean that the convergence time of the algorithm would increase. Hence, it is a trade-off between the steady-state error and convergence rate. Note that as the noise variance reduces, the gap between the performances of the systems reduces because the advantage offered by the spatial diversity becomes more relevant when there is more noise. The performance of any monopulse system is independent of the absolute values of the signals of interest. This is an outcome of the fact that we use a ratio in monopulse processing instead of the absolute values of the measured signals in both the channels. As the noise variance increases, we get to see that the improvement offered by the spatial diversity of the MIMO system also increases.

The advantage of the proposed monopulse MIMO radar over monopulse SISO radar stems from the fact that by employing multiple antennas, we are exploiting the fluctuations in the target RCS values with respect to the angle of view. Even if the RCS between one transmitter-receiver pair is very small, it is highly likely that the other transmitter-receiver pairs will compensate for it. Also, in our proposed algorithm, the weights are proportional to the received energies. Hence, with high probability,

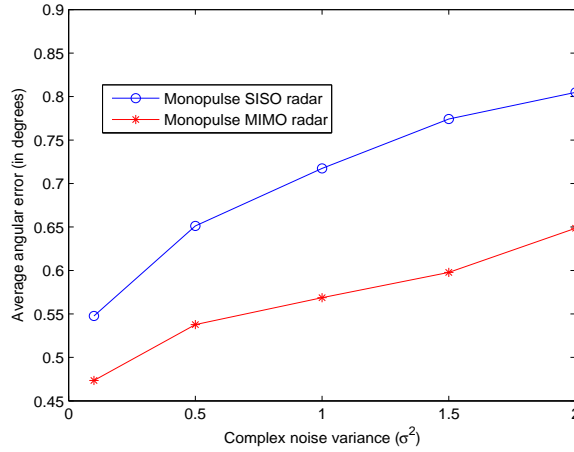


Figure 4.10: Comparing the average angle error of SISO and MIMO monopulse radars as a function of the complex noise variance σ^2 .

a transmitter-receiver pair with high RCS value will contribute significantly to the received energy at that particular receiver.

Along with tracking the angular location of the target, the exact coordinates of the target location can also be estimated by evaluating the points of intersection of the boresight axes coming from all the receivers. Since this processing is possible only for monopulse systems with multiple receivers, we compare the the locating capabilities of our proposed 2x3 MIMO radar and conventional 2x3 radar. For the conventional 2x3 radar, all the 6 attenuations will be the same where as these attenuations will be different for MIMO radar due to the wide antenna separation. This takes care of the target fluctuations. From Fig. 4.11, it is evident that MIMO radar outperforms the conventional 2x3 radar at all the noise variances since it offers more spatial diversity.

In the following simulations, we show the localizing abilities of 2x3 MIMO radar under different challenging scenarios.

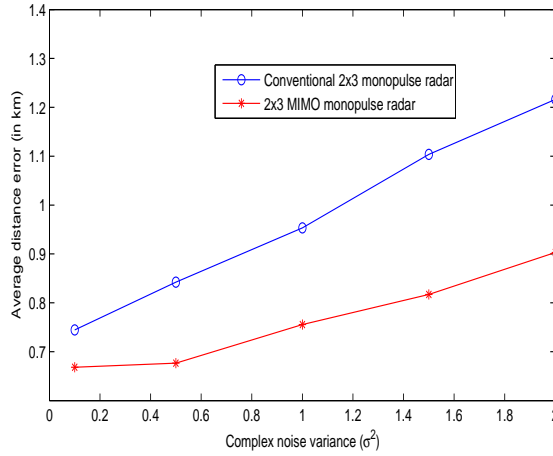


Figure 4.11: Comparing the average distance errors of 2x3 MIMO and conventional radars as a function of the complex noise variance σ^2 .

4.5.3 Rapidly Maneuvering Airborne Target

A clever target would change its direction of travel at high velocities to reduce the detectability and to confuse the tracking radar. Hence, it is extremely important to track a rapidly maneuvering airborne target. In order to check the performance of the algorithm in this scenario, we increased the velocity of the target to (2.5, 0.833) km/s and further made the target change its direction at two different locations over a time span of 8s. These high velocities are a feature of the next generation hypersonic missiles. We see from Fig. 4.12 that the radar system keeps track of the target inspite of the very high velocities and direction changes. The noise variance $\sigma^2 = 0.1$ for this simulation. This corresponds to an SNR of 12.3dB.

4.5.4 Effect of a Jamming Signal

In defense applications, the enemy tries to mislead the radar by sending jamming signals that interfere with the target returns. If the frequency of the jamming signals

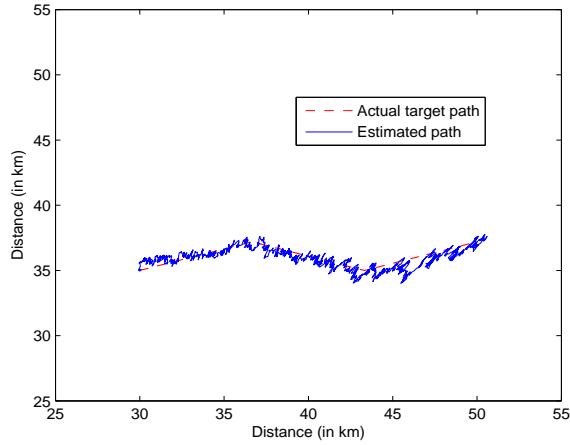


Figure 4.12: Monopulse MIMO tracker for a rapidly maneuvering airborne target for $\sigma^2 = 0.1$.

is close to f_c , it is difficult for the radar to localize the target. This situation is analogous to having an interfering target apart from the target of interest. We now show that the proposed monopulse MIMO radar system manages to locate the target even in the presence of a jamming sinusoid of frequency f_c . We assumed the source of the sinusoid is located at the coordinates (25, 10). We chose the power of the received sinusoid to be 10 percent of that of each transmitted waveform. We used the same target path and velocities as described for the rapidly maneuvering airborne target. We clearly see from Fig. 4.13 that there is a degradation in performance when compared to Fig. 4.12 because of the jamming signal. The tracker moves in a different direction for a while but still manages to correct itself and locates the target. Hence, even in the presence of the jammer, the proposed system manages to follow a rapidly maneuvering airborne target.

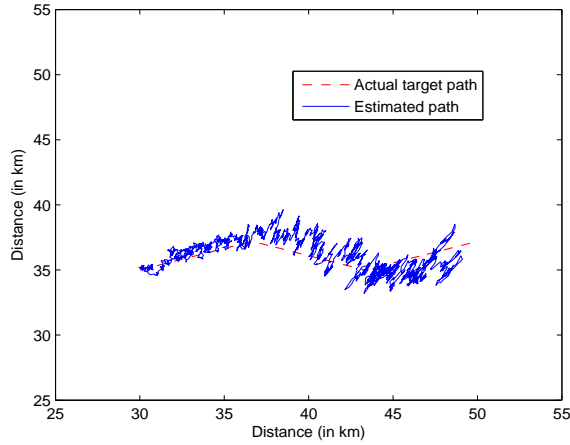


Figure 4.13: Monopulse MIMO tracker for a rapidly maneuvering airborne target in the presence of a jammer for $\sigma^2 = 0.1$.

4.5.5 Sequential vs Simultaneous Lobing

We mentioned in the introduction section that simultaneous lobing (monopulse) is immune to pulse-to-pulse fluctuations whereas sequential lobing suffers from this drawback. Now, we demonstrate the advantage of choosing simultaneous lobing for our proposed system using numerical simulations. We used the same radar, rapidly maneuvering airborne target, jammer scenario as described in this section. In order to make a fair comparison, we doubled the pulse repetition frequency for sequential lobing to keep the overall data rate constant. It is evident from Fig. 4.14 that the system completely loses track of the target in the middle of the flight. It moves in a completely different direction to that of the target. In fact, the tracker moves significantly in the direction of the jamming source located at (25, 10). This shows the shortcomings of sequential lobing and thus emphasizes the advantages of using monopulse for the proposed multiple antenna tracking radar.

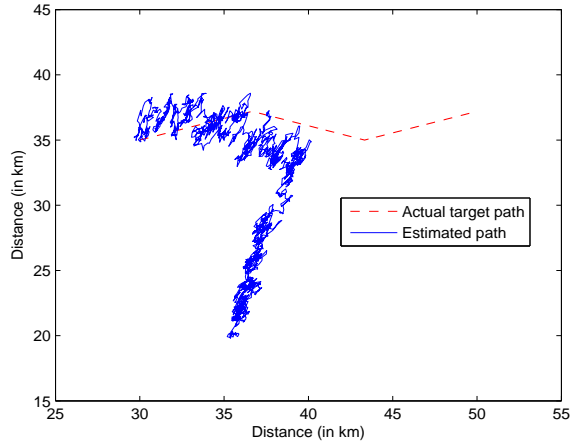


Figure 4.14: Monopulse MIMO tracker for a rapidly maneuvering airborne target using sequential lobing in the presence of a jammer for $\sigma^2 = 0.1$.

4.5.6 Maneuvering Ground Target

Ground targets move at lesser velocities when compared with the airborne targets we have considered so far. However, ground targets have the flexibility to change directions at sharp angles. They can sometimes change their direction by 90 degrees. This poses an important challenge to the tracking system. In Fig. 4.15, we simulated a ground target moving at a velocity of $(25, 25)$ m/s and completely changing directions at three different locations. Since the target moves slower than an airborne target, we chose the pulse repetition rate $T_R = 0.4$ s for the simplicity of numerical simulations. We see that the tracker follows the target at each of these locations inspite of the sharp angle changes and the reduction of pulse repetition frequency.

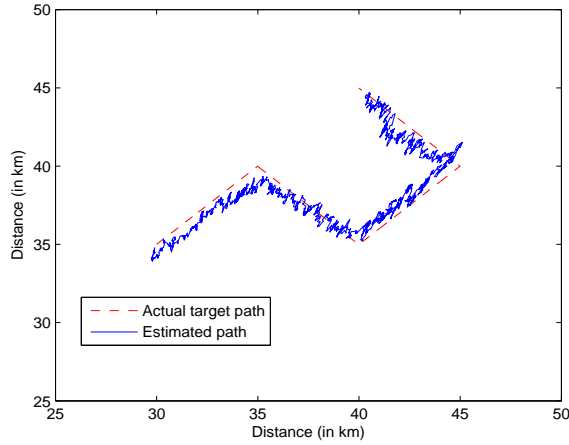


Figure 4.15: Monopulse MIMO tracker for a maneuvering ground target for $\sigma^2 = 0.1$.

4.6 Summary

We have proposed a multiple distributed antenna tracking radar system with monopulse receivers. We used Capon beamforming to generate the beams of the monopulse receivers. Further, we developed a tracking algorithm for this system. We simulated a realistic scenario to analyze the performance of the proposed system. We demonstrated the advantages offered by this system over conventional single antenna monopulse tracking radar. This advantage is a result of the spatial diversity offered by distributed MIMO radar systems. We also showed that the proposed system keeps track of a rapidly maneuvering airborne target, even in the presence of an intentional jamming signal. This is an extremely important feature in any defence application. Further, we demonstrated the advantages of having simultaneous lobing (monopulse) in our system as opposed to sequential lobing. Also, we showed that the monopulse MIMO tracker follows a maneuvering ground target that changes its directions at sharp angles.

In future work, we will perform an asymptotic error analysis and develop performance bounds for the proposed tracking algorithm. We will also use real data to demonstrate the advantages of the proposed system.

Chapter 5

Target Estimation Using Sparse Modeling for Distributed MIMO Radar⁴

5.1 Introduction

Compressive sensing allows us to accurately reconstruct data from significantly fewer samples than the Nyquist rate if the received signal is sparse in some basis representation [56], [57], [58], [59]. With the improvement in the capabilities of the computational resources, it has become more feasible to use compressive sensing for different medical and engineering applications [60], [61], [62], [63], [64], [65]. Since the number of targets in a radar scene is often limited, we can use sparse modeling to represent the radar data. Therefore, compressive sensing is applicable to the field of radar [62], [63], [64], [65].

⁴Based on S. Gogineni and A. Nehorai, “Target estimation using sparse modeling for distributed MIMO radar,” *IEEE Trans. Signal Process.*, vol. 59, no. 11, pp. 5315-5325, Nov. 2011. ©[2011] IEEE.

So far, compressive sensing has been used for MIMO radar only in the context of closely spaced antennas [64]– [66]. In this chapter, we propose to use sparse modeling and compressive sensing for distributed MIMO radar (see also [67], [68]) in the context of multiple-target parameter estimation problem. We develop a new realistic metric to analyze the performance of such systems. Additionally, we propose an optimal adaptive energy allocation mechanism for distributed MIMO radar by making use of the estimates of the complex target attenuations from the previous processing interval (see also [69]).

5.2 Signal Model

In this section, we describe the signal model for our MIMO radar system. We assume that there are M_T transmitters, M_R receivers, and K targets. Further, we assume that all the targets are moving in a two dimensional plane. However, without loss of generality, we can extend the analysis in this chapter to the three dimensional case. We assume that each of the targets contains multiple individual isotropic scatterers. The bandwidth of the transmitted waveform determines the resolution of the system. We require very high bandwidth to resolve each of the individual scatterers of the target. But due to practical bandwidth constraints, the system cannot resolve these individual scatterers. Therefore, this collection of scatterers can be expressed as one point scatterer which represents the RCS center of gravity of these multiple scatterers [2], [70]. By point target, we refer to the smallest target that can be resolved by the system. The RCS center of gravity of the k^{th} target is located at $\vec{\mathbf{p}}^k = [p_x^k, p_y^k]$ on a Cartesian coordinate system and it moves with a velocity $\vec{\mathbf{v}}^k = [v_x^k, v_y^k]$. The position and velocity parameters represent the center of gravity of the

target during a particular processing interval. The i^{th} transmitter and j^{th} receiver are located at $\vec{\mathbf{t}}_i = [t_{i_x}, t_{i_y}]$ and $\vec{\mathbf{r}}_j = [r_{j_x}, r_{j_y}]$, respectively. We transmit orthonormal waveforms from the different transmitters. Hence, the transmitted energy from the i^{th} antenna $E_i = 1$ and the total transmitted energy $E = \sum_{i=1}^{M_T} E_i = M_T$. Let $w_i(t)$ be the complex baseband waveform transmitted from the i^{th} transmitter. Then, the bandpass signal emanating from the i^{th} transmit antenna is given as

$$\tilde{w}_i(t) = \text{Re} \{ w_i(t) e^{j2\pi f_c t} \}, \quad (5.1)$$

where $\text{Re}\{\cdot\}$ denotes the real part of the argument, $j = \sqrt{-1}$, f_c is the carrier frequency. These signals travel in space and reflect off the surfaces of the targets and are captured by the receivers. Further, we assume that the cross correlations between these waveforms is close to zero for different delays [2], [1], [13]. Let $a_{ij}^k(t)$ denote the attenuation corresponding to the k^{th} target between the i^{th} transmitter and the j^{th} receiver. Note that the attenuation is dependent on the transmitter-receiver indices under consideration. This is a result of the wide separation between the antennas. For a colocated MIMO setup, the RCS value would be the same for all transmitter-receiver indices [3], [4].

Under a narrow band assumption on the waveforms, the bandpass signal arriving at the j^{th} receiver can be expressed as

$$y_j(t) = \text{Re} \left\{ \sum_{k=1}^K \sum_{i=1}^{M_T} a_{ij}^k(t) w_i(t - \tau_{ij}^k) e^{j2\pi (f_{D_{ij}}^k (t - \tau_{ij}^k) + f_c (t - \tau_{ij}^k))} \right\}, \quad (5.2)$$

where τ_{ij}^k and $f_{D_{ij}}^k$ are the delay and Doppler shift corresponding to the k^{th} target.

$$\tau_{ij}^k = \frac{1}{c} \left(\|\vec{\mathbf{p}}^k - \vec{\mathbf{t}}_i\| + \|\vec{\mathbf{p}}^k - \vec{\mathbf{r}}_j\| \right), \quad (5.3)$$

$$f_{D_{ij}}^k = \frac{f_c}{c} \left(\langle \vec{\mathbf{v}}^k, \vec{\mathbf{u}}_{r_j}^k \rangle - \langle \vec{\mathbf{v}}^k, \vec{\mathbf{u}}_{t_i}^k \rangle \right), \quad (5.4)$$

where $\vec{\mathbf{u}}_{t_i}^k, \vec{\mathbf{u}}_{r_j}^k$ denote the unit vector from the i^{th} transmitter to the k^{th} target and the unit vector from the k^{th} target to the j^{th} receiver, respectively; \langle, \rangle is the inner product operator, and c is the speed of propagation of the wave in the medium. The term $e^{-j2\pi f_c \tau_{ij}^k}$ represents the phase shift and it is also dependent on the transmitter-receiver indices under consideration.

The received signals at each receiver are first down converted from the radio frequency and then passed through a bank of M_T matched filters, each of which corresponds to a particular transmitter. Assume that the target attenuations values do not vary within a pulse duration and the Doppler shift is small. Therefore, $a_{ij}^k(t)e^{j2\pi f_{D_{ij}}^k t}$ varies slowly when compared with the waveform $w_i(t)$ and is almost constant across a pulse duration. In other words, it can be taken outside of the integral in the matched filter operation. This is a valid assumption for targets whose velocity is much smaller than the speed of light in the medium. So, the integral only contains the waveform terms and under the orthogonality assumption of the waveforms for all delays [1], [2], [13], the sampled outputs of the i^{th} matched filter at the j^{th} receiver are given as

$$y_{ij}(n) = \sum_{k \in \mathcal{K}} a_{ij}^k(n) e^{j2\pi \left(f_{D_{ij}}^k (nT_s - \tau_{ij}^k) - f_c \tau_{ij}^k \right)} + e_{ij}(n), \quad (5.5)$$

where $e_{ij}(n)$ is the additive noise at the output of the i^{th} matched filter of the j^{th} receiver, \mathcal{K} represents a set containing all the targets that contribute to the matched filter output at n . n and T_s denote the sample index and sampling interval, respectively. Note that the waveform term w_i is no longer present in this equation as it is integrated out of the matched filter due to the orthogonality of the waveforms (see also [1]).

We define the target state vector $\zeta = [p_x, p_y, v_x, v_y]^T$. Hence, the important properties of the target (position, velocity) are specified by ζ . The goal is to estimate ζ for all the K targets. Now, we discretize the target state space into a grid of L possible values $\{\zeta^l, \forall l = 1, \dots, L\}$. Hence, each of the targets is associated with a state vector belonging to this grid. If the presence of a target at ζ^l would contribute to the matched filter output at n , then define

$$\psi_{ij}^l(n) = e^{j2\pi(f_{D_{ij}}^l(nT_s - \tau_{ij}^l) - f_c \tau_{ij}^l)}. \quad (5.6)$$

Otherwise, $\psi_{ij}^l(n) = 0$. Also, if ζ^l is the state vector of the k^{th} target, we define

$$s_{ij}^l(n) = a_{ij}^k(n). \quad (5.7)$$

Otherwise, $s_{ij}^l(n) = 0$. For each j , we stack $s_{ij}^l(n)$, $y_{ij}(n)$, and $e_{ij}(n)$ corresponding to different transmitters to obtain M_T dimensional column vectors $\mathbf{s}_j^l(n)$, $\mathbf{y}_j(n)$ and $\mathbf{e}_j(n)$, respectively. Similarly, we arrange $\psi_{ij}^l(n)$ into $(M_T) \times (M_T)$ dimensional diagonal matrix $\Psi_j^l(n)$.

$$\mathbf{s}_j^l(n) = [s_{1j}^l(n), \dots, s_{M_T j}^l(n)]^T, \quad (5.8)$$

$$\mathbf{y}_j(n) = [y_{1j}(n), \dots, y_{M_T j}(n)]^T, \quad (5.9)$$

$$\mathbf{e}_j(n) = [e_{1j}(n), \dots, e_{M_T j}(n)]^T, \quad (5.10)$$

$$\Psi_j^l(n) = \text{diag} \{ \psi_{1j}^l(n), \dots, \psi_{M_T j}^l(n) \}, \quad (5.11)$$

where $\text{diag}\{\cdot\}$ refers to a diagonal matrix whose entries are given by $\{\cdot\}$ and $[\cdot]^T$ denotes the transpose of $[\cdot]$. Further, we arrange $\{\mathbf{s}_j^l(n)\}_{j=1}^{M_R}$, $\{\mathbf{y}_j(n)\}_{j=1}^{M_R}$, and $\{\mathbf{e}_j(n)\}_{j=1}^{M_R}$ into $M_T M_R$ dimensional column vectors $\mathbf{s}^l(n)$, $\mathbf{y}(n)$, and $\mathbf{e}(n)$, respectively and

$\{\Psi_j^l(n)\}_{j=1}^{M_R}$, into $(M_T M_R) \times (M_T M_R)$ dimensional diagonal matrix $\Psi^l(n)$.

$$\mathbf{s}^l(n) = \left[(\mathbf{s}_1^l(n))^T, \dots, (\mathbf{s}_{M_R}^l(n))^T \right]^T, \quad (5.12)$$

$$\mathbf{y}(n) = \left[(\mathbf{y}_1(n))^T, \dots, (\mathbf{y}_{M_R}(n))^T \right]^T, \quad (5.13)$$

$$\mathbf{e}(n) = \left[(\mathbf{e}_1(n))^T, \dots, (\mathbf{e}_{M_R}(n))^T \right]^T, \quad (5.14)$$

$$\Psi^l(n) = \text{diag} \{ \Psi_1^l(n), \dots, \Psi_{M_R}^l(n) \}. \quad (5.15)$$

Finally, stacking $\{\mathbf{s}^l(n)\}_{l=1}^L$ and $\{\Psi^l(n)\}_{l=1}^L$ into $LM_T M_R$ dimensional column vector and $(M_T M_R) \times (LM_T M_R)$ dimensional matrix, respectively, we obtain

$$\mathbf{s}(n) = \left[(\mathbf{s}^1(n))^T, \dots, (\mathbf{s}^L(n))^T \right]^T, \quad (5.16)$$

$$\Psi(n) = [\Psi^1(n), \dots, \Psi^L(n)]. \quad (5.17)$$

Therefore, we can express the received vector at n as

$$\mathbf{y}(n) = \Psi(n)\mathbf{s}(n) + \mathbf{e}(n), \quad (5.18)$$

where $\mathbf{s}(n)$ is a sparse vector with $K M_T M_R$ non-zero entries. Note that the non zero entries of this vector appear in blocks of size $M_T M_R$. Therefore, we can call $\mathbf{s}(n)$ as a block sparse vector with K non zero blocks and each block containing $M_T M_R$ entries. We have expressed our observed data at n using sparse representation. For each matched filter, let the sampled output signal for each pulse contain N_M samples. When the velocities of the targets are much smaller than the speed of wave propagation in the medium, we require multiple pulses to estimate these velocities since the effect of the Doppler within one pulse duration will be negligible (see Fig. 4.2 in [71]). Hence, in each processing interval we consider N_P pulses. Therefore,

in each processing interval, we have $N = N_M \times N_P$ samples at the output of each matched filter. We assume that the target attenuation values do not vary over a period of N_P pulses. Now, we stack $\{\mathbf{y}(n)\}_{n=1}^N$, $\{\mathbf{e}(n)\}_{n=1}^N$, and $\{\Psi(n)\}_{n=1}^N$ into

$$\mathbf{y} = \left[(\mathbf{y}(1))^T, \dots, (\mathbf{y}(N))^T \right]^T, \quad (5.19)$$

$$\mathbf{e} = \left[(\mathbf{e}(1))^T, \dots, (\mathbf{e}(N))^T \right]^T, \quad (5.20)$$

$$\Psi = \left[(\Psi(1))^T, \dots, (\Psi(N))^T \right]^T, \quad (5.21)$$

to obtain

$$\mathbf{y}_{(NM_T M_R) \times (1)} = \Psi_{(NM_T M_R) \times (LM_T M_R)} \mathbf{s}_{(LM_T M_R) \times (1)} + \mathbf{e}_{(NM_T M_R) \times (1)}. \quad (5.22)$$

Note that in the above expression for the measurement vector, Ψ is known and only \mathbf{s} depends on the actuals targets present in the illuminated area. The non zero entries of \mathbf{s} represent the target attenuation values and the corresponding indices determine the positions and velocities. Further, note that in order to obtain the measurement vector in the above equation, each of the receivers sends their measurements to a common processor that stacks them appropriately to obtain \mathbf{y} . This common processor performs the estimation that we describe in the next section. None of the receivers perform any local estimation because any such approach can only be sub optimal. In [72], the authors show that the estimation error of a MIMO radar system is increased while employing decentralized processing.

5.3 Sparse Support Recovery

In the previous section, we have expressed the signal received across M_R receive antennas over N samples using sparse representation. In order to find the properties of the targets (position, velocity), we need to recover the sparse vector \mathbf{s} from the measurements \mathbf{y} . There are many approaches to perform the recovery. Two approaches are Basis Pursuit [73] (BP) and Matching Pursuit [74] (MP). These algorithms are well known in the field of sparse signal processing. Further, these algorithms recover sparse vectors but do not exploit the knowledge of the block sparsity. However, very recently, in [75], the authors propose an extension of the matching pursuit algorithm called block-Matching Pursuit (BMP) that exploits the knowledge of block sparsity. In this section, we present BP and BMP for sparse support recovery. We shall use these algorithms in the numerical simulations to demonstrate the performance of the MIMO radar system. We will use the same algorithms while employing compressive sensing.

5.3.1 Basis Pursuit (BP)

Basis pursuit is an optimization principle. It is presented under two scenarios; in the absence of noise and in the presence of noise.

Absence of Noise

In the absence of noise, BP aims at minimizing $\|\mathbf{s}\|_1$ under the constraint $\mathbf{y} = \Psi\mathbf{s}$. Since usually $N \ll L$, there are many different vectors \mathbf{s} that satisfy the constraint. We choose the solution that has the least l_1 norm. This optimization problem can

be modeled as a linear program [73]. There are many existing algorithms to solve this problem. It can be solved using `CVX`, a package for specifying and solving convex programs [76], [77].

Presence of Noise

Clearly the above approach of basis pursuit will fail in the presence of noise. Hence, in [73], the authors propose Basis Pursuit De-Noising (BPDN). This is an unconstrained minimization problem

$$\min \frac{1}{2} (\|\mathbf{y} - \mathbf{\Psi}\mathbf{s}\|_2)^2 + \lambda\|\mathbf{s}\|_1. \quad (5.23)$$

When the columns of $\mathbf{\Psi}$ are normalized, typically $\lambda = \sigma\sqrt{2\log(LM_{\text{T}}M_{\text{R}})}$ where σ represents the noise level [73]. In this problem, since we consider multiple pulses in each processing interval, the columns are not normalized by definition. Therefore, we scale the λ value accordingly to perform the simulations. We used `CVX` to implement this algorithm. We present the results in section 5.6.

5.3.2 Block-Matching Pursuit (BMP)

Before we describe BMP, we shall first give a description of the conventional MP. It is an iterative algorithm [74] that can be used for sparse signal recovery. Since all the columns of $\mathbf{\Psi}$ are not necessarily independent, there are infinitely many solutions for \mathbf{s} even when there is no noise. In MP, we first initialize the reconstructed vector $\mathbf{s}^{(0)} = \mathbf{0}$ and the residual $\mathbf{r}^{(0)} = \mathbf{y}$. In each subsequent iteration k' , we project the residual vector $\mathbf{r}^{(k'-1)}$ onto all the columns of $\mathbf{\Psi}$ and pick the column $\boldsymbol{\psi}^{(k')}$ that has the highest correlation with the residual. We update the estimated reconstructed

vector

$$\mathbf{s}^{(k')} = \mathbf{s}^{(k'-1)} + \frac{\langle \mathbf{r}^{(k'-1)}, \boldsymbol{\psi}^{(k')} \rangle}{\langle \boldsymbol{\psi}^{(k')}, \boldsymbol{\psi}^{(k')} \rangle} \boldsymbol{\psi}^{(k')}. \quad (5.24)$$

We finally update the residual as

$$\mathbf{r}^{(k')} = \mathbf{r}^{(0)} - \mathbf{s}^{(k')}. \quad (5.25)$$

Even though this algorithm can be used to recover \mathbf{s} , it does not make use of the knowledge that the vector \mathbf{s} is block sparse. In [75], the authors propose BMP which exploits this knowledge. Similar to MP, we initialize the reconstructed vector $\mathbf{s}^{(0)} = \mathbf{0}$ and the residual $\mathbf{r}^{(0)} = \mathbf{y}$. We divide the columns of $\boldsymbol{\Psi}$ into blocks of size $M_T M_R$. There are L such blocks. In each subsequent iteration, we project the residual vector onto all of these L blocks and pick the block that gives the highest energy after projection. Now, the estimated reconstructed vector is updated by adding the projections onto each of the columns of this block. The residual is also updated accordingly. Note that the main difference when compared with MP is that here the updates are done one block (columns corresponding to different transmitter and receivers) at a time whereas in MP, the updates are done one column at a time. In [75], the authors analyze the performance of block sparsity based approaches and show that the improvement in using the block sparsity based recovery algorithms is maximum when all the columns within a block are orthogonal. It can be easily checked that the columns corresponding to different transmitter-receiver pairs in the basis matrix $\boldsymbol{\Psi}$ are orthogonal by the definition of $\boldsymbol{\Psi}$ in our signal model. Therefore, BMP is well suited for recovering \mathbf{s} in this problem.

The performance of the sparsity based estimation approaches is determined by the correlations between the columns of the dictionary matrix $\boldsymbol{\Psi}$ and the distance between

the adjacent grid points. More specifically, when the non zero entries of the sparse vector appear in blocks, a major factor in determining the performance of the system is the block coherence measure [75]. Let $\Psi[l]$ denoted the l^{th} block of the dictionary. Therefore, $\Psi[l]$ has $M_T M_R$ columns. Define

$$\mathbf{M}[l, r] = \Psi^H[l] \Psi[r]. \quad (5.26)$$

The block coherence measure is defined as

$$\mu_B = \max_{l, r \neq l} \frac{1}{M_T M_R} \rho(\mathbf{M}[l, r]), \quad (5.27)$$

where $\rho(\mathbf{M}[l, r])$ denotes the spectral norm of $\mathbf{M}[l, r]$. The block coherence measure should be small in order to obtain good performance. However, as the grid points come closer, the resolution is improved but block coherence measure increases because the correlation between the adjacent blocks will increase. Therefore, it is a tradeoff between the grid size and the coherence measure. In Fig. 5.1, we plot the block coherence measure as a function of the distance between adjacent grid points (in m and m/s for position and velocity respectively). We observe the coherence measure increases as the distance reduces.

5.4 Optimal Adaptive Energy Allocation

Before we propose the energy allocation mechanism, we first define a new performance metric that naturally fits into this multiple target scenario. Conventional metrics like mean square error (MSE) are commonly used in radar applications and they are apt in single target scenarios. However, they do not efficiently capture the estimation

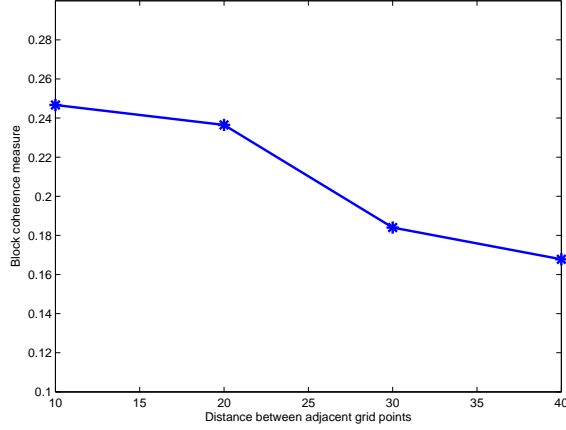


Figure 5.1: Block coherence measure as a function of the distance between adjacent grid points.

accuracies in multi-target scenario. For example, even if the estimates of the parameters of some of the targets are poor, the overall MSE (averaged over all the targets) can still be small if the estimates of majority of the other targets are very accurate. Hence the deficiencies in the estimates of the weak targets will go unnoticed. To overcome this problem, we propose a new performance metric. We will describe this metric in this section.

As mentioned earlier, the $LM_{\text{T}}M_{\text{R}}$ length vector \mathbf{s} has only $KM_{\text{T}}M_{\text{R}}$ non-zero entries. Let the reconstructed vector be denoted by $\hat{\mathbf{s}}$. We would like to have the most significant $KM_{\text{T}}M_{\text{R}}$ entries of $\hat{\mathbf{s}}$ correspond to the same indices as the non-zero entries of the actual sparse vector \mathbf{s} . If this is not the case, then we will wrongly map the target states for one or more targets. We define a L length vector

$$\tilde{\mathbf{s}}(l) = \sum_{i=1}^{M_{\text{T}}} \sum_{j=1}^{M_{\text{R}}} \|\hat{\mathbf{s}}(M_{\text{T}}M_{\text{R}}(l-1) + M_{\text{R}}(j-1) + i)\|^2, \forall l = 1, \dots, L. \quad (5.28)$$

This vector essentially combines the energies of the components corresponding to the different transmit-receiver pairs for each point in the target state space. Further, define $\tilde{\mathbf{s}}^*$ as a K length vector which contains the values that $\tilde{\mathbf{s}}$ carries at the correct K indices. Similarly we define $\overline{\mathbf{s}}^*$ as a L length vector that takes a value of 0 at the correct K indices and takes the same values as $\tilde{\mathbf{s}}$ at every other index. It is clear that the non-zero entries of $\overline{\mathbf{s}}^*$ correspond to the non-target states and the zero entries correspond to the correct target states.

We define the metric

$$\Delta = \frac{\min \tilde{\mathbf{s}}^*}{\max \overline{\mathbf{s}}^*}. \quad (5.29)$$

The numerator of this metric denotes the weakest target component in the reconstructed vector. The denominator denotes the strongest non-target component in the reconstructed vector. If this metric has value greater than one, then all the actual (correct) target indices dominate the other indices in $\tilde{\mathbf{s}}$ and hence the estimates of position and velocity will exactly match the true values. Otherwise, at least one of the non-target indices will dominate the weakest target and hence, the position and velocity estimates do not match the true values. Note that $\Delta > 1$ only guarantees exact estimation of the position and velocity. The accuracy in the estimates of the target attenuations is determined by the exact value taken by Δ . If Δ is large, then most of the reconstructed energy is distributed in the correct target indices, thereby giving accurate estimates of the attenuations. Hence, the higher the value of Δ , the better the performance of the system. In section 5.6, we use this metric to analyze the results.

Adaptive energy allocation has been shown to provide improved detection performance in distributed MIMO radar systems [78]. In this chapter, we will present a

novel adaptive energy allocation scheme to improve the estimation performance. Let E_i be the energy of the waveform transmitted from the i^{th} transmitter. We initialize the system by transmitting multiple pulses of unit energy waveforms $E_i = 1$, from all the transmitters. Hence, the total energy transmitted per pulse is $\sum_{i=1}^{M_T} E_i = M_T$. After collecting a vector of outputs at the multiple receiver matched filters, the processor performs the sparse recovery to estimate the attenuations a_{ij}^k using the algorithms mentioned in the previous section. Since the different antenna pairs view the targets from different angles, these attenuations and their corresponding estimates will be different from each other. Hence, equal energy allocation to all the transmitters does not necessarily give the best performance. After the estimation, the energy allocation scheme is applied to decide upon the transmit energies for the next set of transmit pulses while keeping the total transmitted energy constant. The goal of this scheme is to maximize the minimum target returns. This is naturally motivated from the performance metric defined earlier in this section. The numerator in the performance metric denotes the minimum target returns. We solve the following optimization problem and find the optimal E_i such that $\sum_{i=1}^{M_T} E_i = M_T$

$$\max_{E_i} \min_k \sum_{i=1}^{M_T} \sum_{j=1}^{M_R} E_i \|\widehat{a}_{ij}^k\|^2. \quad (5.30)$$

We can solve the above optimization problem using CVX [76], [77]. Since this problem depends only on the dimensionality of the MIMO radar configuration and the number of targets and not on the huge dimensionality of the basis dictionary, it can be solved quickly. This makes it amenable to use in practical systems in an online manner. After solving this problem, the processor feeds back this information to the transmitters which send the next set of pulses with these optimally selected values of

energies. Hence, the system operates in a closed loop. The energy allocation mechanism discussed above is not only applicable to the sparsity based estimation method mentioned in this chapter but it is relevant in any multiple target scenario. Note that it only requires us to have estimates of the attenuations. In this chapter, these estimates are computed using sparse support recovery. In principle, these estimates can be computed using any other approach and still this energy allocation scheme will be relevant. We shall show in section 5.6 that this optimal choice of waveform energies gives significant improvement in performance.

5.5 Compressive Sensing

Compressive sensing allows us to accurately reconstruct data from significantly fewer samples than the Nyquist rate if the received signal is sparse [56]. Nyquist rate sampling assumes the signals to be bandlimited. Similarly, the requirement for applying compressive sampling is that the signals must have a sparse representation using some basis. In section 5.2, we saw that the measurement vector \mathbf{y} has dimensions $NM_T M_R$. Since our measurement vector is sparse in the space spanned by the columns of the matrix Ψ , the theory of compressive sensing says that we can reconstruct the vector \mathbf{s} from far fewer samples than contained in the vector \mathbf{y} . If the sensing basis is represented by Φ , then the coherence measure between Φ and Ψ measures the largest correlation between them. Φ must be such that it has as little coherence with Ψ as possible [56]. Since random matrices satisfy low coherence properties, we generate the entries of the $(N_{CS}) \times (NM_T M_R)$ dimensional sensing matrix Φ from independent Gaussian distribution, where $N_{CS} \ll NM_T M_R$. Since the entries of Φ are independent from each other, each sensor will project its received data separately

using Gaussian sequences of appropriate lengths and send the compressed data to the fusion center which will combine the data from different sensors appropriately. The new measurement vector at the fusion center in the presence of noise is

$$\mathbf{y}_{\text{CS}} = \Phi\Psi\mathbf{s} + \Phi\mathbf{e}. \quad (5.31)$$

For reconstruction of \mathbf{s} , we use the same algorithms as presented in section 5.3. Define $\frac{N_{\text{CS}}}{NM_{\text{T}}M_{\text{R}}} \times 100\%$ as the percentage of samples used in compressive sensing. In section 5.6, we will show the performance of the MIMO radar system for different levels of compression. The adaptive energy allocation mechanism presented in the previous section can also be applied for the case of compressive sensing. We use the estimates of the target attenuations $\widehat{a_{ij}^k}$ to select the energy allocation for the next processing interval.

5.6 Numerical Results

We begin with a description of the simulated scenario. We simulated a 2×2 MIMO radar system. We denote the positions of all the transmitters, targets and receivers on a common Cartesian coordinate system. The transmitters are located at $\vec{\mathbf{t}}_1 = [100, 0]$ m and $\vec{\mathbf{t}}_2 = [200, 0]$ m, respectively. The receiver locations are $\vec{\mathbf{r}}_1 = [0, 200]$ m and $\vec{\mathbf{r}}_2 = [0, 100]$ m, respectively. The carrier frequency of the transmitted waveforms is $f_c = 1$ GHz. Within each processing interval, we consider three pulses that are transmitted 33.3ms apart. We choose $N = 243$ for the simulation results. Therefore, \mathbf{y} has 972 entries. We divide the target position space into 9×9 grid points and the target velocity space into 5×5 grid points. Therefore, the total number of possible

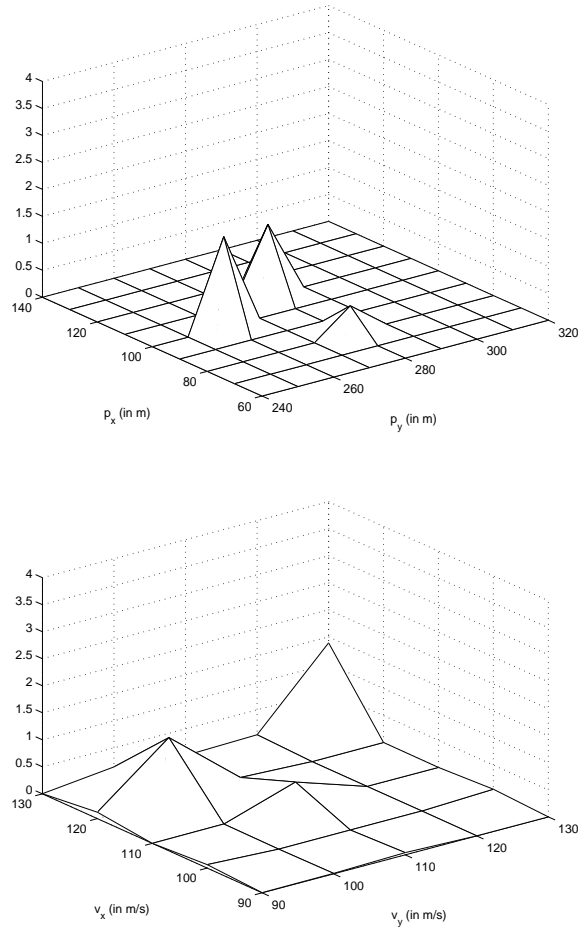


Figure 5.2: Reconstructed vectors using basis pursuit de-noising at SNR=3.7dB, (a) position estimates, (b) velocity estimates.

target states $L = 2025$. We considered the presence of 3 targets. Hence, the 8100 dimensional sparse vector \mathbf{s} has only $KM_{\text{T}}M_{\text{R}} = 12$ non-zero entries corresponding to the targets.

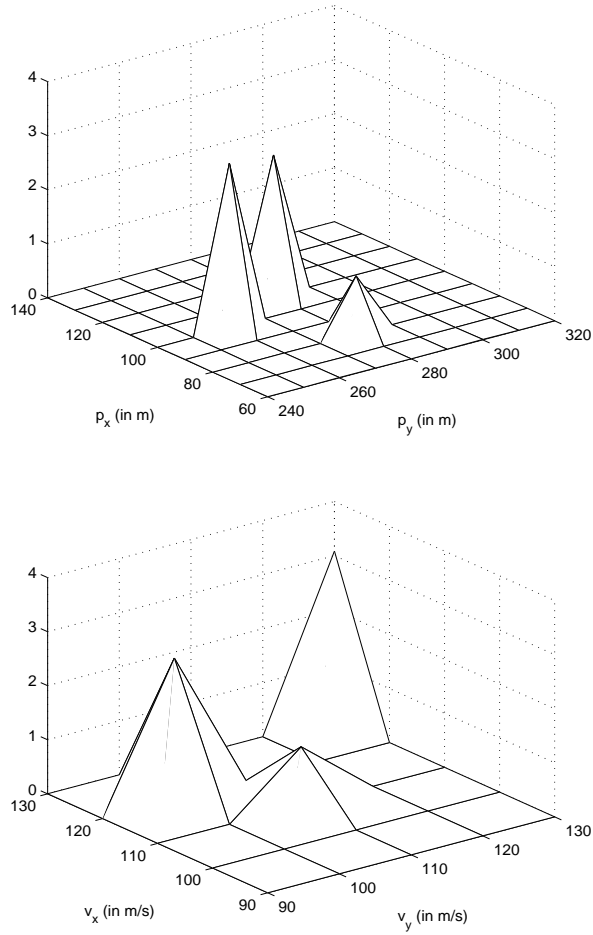


Figure 5.3: Reconstructed vectors using block-matching pursuit at SNR=3.7dB, (a) position estimates, (b) velocity estimates.

The positions and the velocities of the targets are given as

$$\vec{\mathbf{p}}^1 = [110, 280] \text{ m}, \quad (5.32)$$

$$\vec{\mathbf{v}}^1 = [120, 100] \text{ m/s}, \quad (5.33)$$

$$\vec{\mathbf{p}}^2 = [80, 280] \text{ m}, \quad (5.34)$$

$$\vec{\mathbf{v}}^2 = [110, 110] \text{ m/s}, \quad (5.35)$$

$$\vec{\mathbf{p}}^3 = [100, 260] \text{ m}, \quad (5.36)$$

$$\vec{\mathbf{v}}^3 = [130, 130] \text{ m/s}. \quad (5.37)$$

The complex attenuations corresponding to the 3 targets are

$$[a_{11}^1, a_{12}^1, a_{21}^1, a_{22}^1] = [0.3\epsilon, 0.3\epsilon, 0.7\epsilon, 0.8\epsilon], \quad (5.38)$$

$$[a_{11}^2, a_{12}^2, a_{21}^2, a_{22}^2] = [0.4\epsilon, 0.5\epsilon, 0.3\epsilon, 0.2\epsilon], \quad (5.39)$$

$$[a_{11}^3, a_{12}^3, a_{21}^3, a_{22}^3] = [0.4\epsilon, 0.5\epsilon, 0.8\epsilon, 0.7\epsilon], \quad (5.40)$$

where $\epsilon = 1 + \sqrt{-1}$.

The entries of \mathbf{e} are generated independently from Gaussian distribution. We assume each of these samples has the same variance σ^2 . We define the signal to noise ratio (SNR) for the MIMO radar system as

$$\text{SNR} = 10 \log \left(\frac{\|\Psi \mathbf{s}\|^2}{\mathbb{E}(\|\mathbf{e}\|^2)} \right) \text{ dB}. \quad (5.41)$$

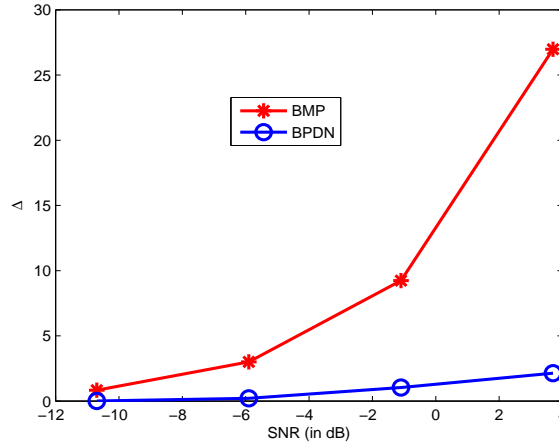


Figure 5.4: Performance metric Δ for basis pursuit de-noising and block-matching pursuit as a function of SNR.

First we compare the performances of the two algorithms basis pursuit de-noising and block-matching pursuit that we presented in section 5.3. We performed these simulations at an SNR of 3.7dB. For BMP, we used 10 iterations. Since it is not

possible to plot the position and velocity on the same plot, we plotted the estimates of position and velocity separately. For computing the estimate at a particular grid point on the position plot, we average over all 5×5 velocity grid points corresponding to that position grid point. Similarly, we average over all the 9×9 position grid points in order to obtain the velocity plot. We do this only to be able to plot position and velocity estimates separately.

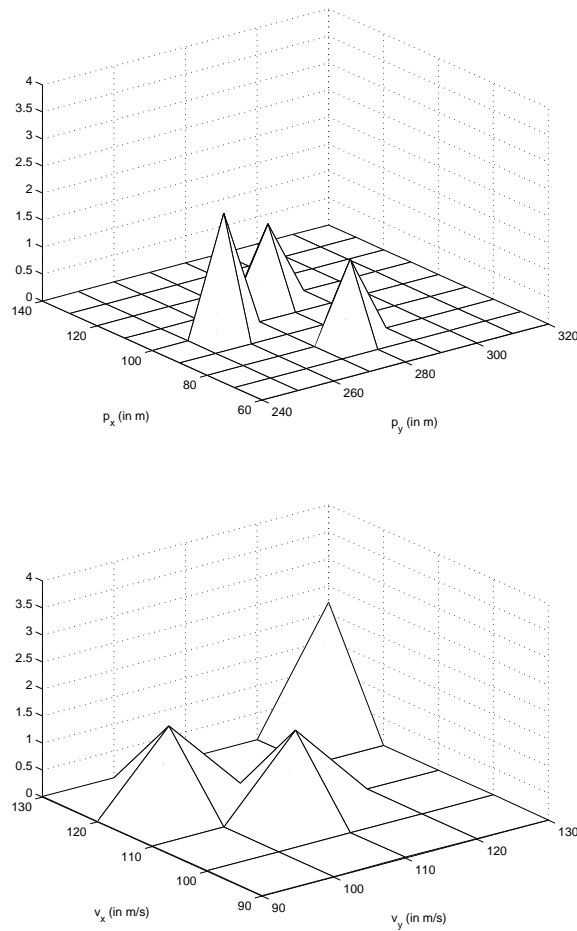


Figure 5.5: Reconstructed vectors with optimal energy allocation at SNR=3.7dB, (a) position estimates, (b) velocity estimates.

From Fig. 5.2 and Fig. 5.3, we can see that both the algorithms are able to estimate the positions and velocities of the 3 targets at an SNR of 3.7dB but the performance

of BP is poor especially for the velocity estimates. We can observe this from Fig. 5.2 because the grid points surrounding the correct velocity points also have significant energies. However, it is important for us to analyze the performances of the two algorithms by evaluating the performance metric Δ . Fig. 5.4 plots Δ as a function of the SNR and we can clearly see that BMP outperforms BP. The value of Δ remains above 1 for much lower SNR for BMP when compared with MP. This clearly shows the improvement in performance as a result of exploiting the block sparse structure of the vector \mathbf{s} . We used 25 independent Monte Carlo runs to generate these results. When $\Delta < 1$, then some of the non-target states dominate the reconstructed vector and hence estimates of the target positions and velocities are incorrect for at least one target. Since BMP outperforms BP, for all further simulation results, we shall use only BMP.

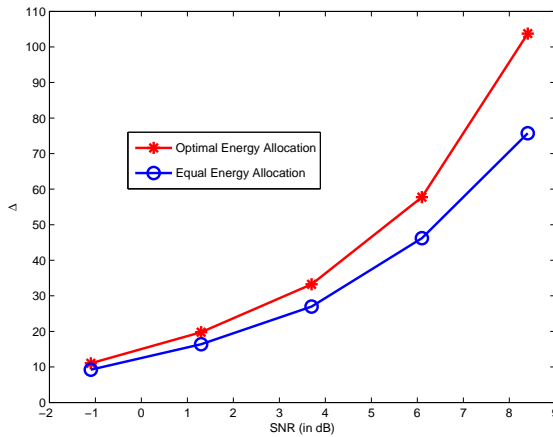


Figure 5.6: Performance metric Δ with and without adaptive energy allocation.

Now, we shall demonstrate the advantages of having adaptive energy allocation. We assume we have estimates of the target attenuations from the estimation of the previous processing interval. We apply the optimization principle we described in section 5.4. The reconstructed vectors for an SNR of 3.7dB are plotted in Fig. 5.5. We can

clearly see that an equalization effect has been achieved when compared with Fig. 5.3. This is a result of the optimization. Now, we quantitatively compare the performances of the MIMO radar system with and without optimal energy allocation. We solve the optimization problem presented in section 5.4 to obtain the optimal $E_1 = 1.626$ and $E_2 = 0.374$. Note that the total transmitted energy is the same $E = M_T = 2$. As we see from Fig. 5.6, the adaptive energy allocation gives significant improvement in performance. The value of Δ for the optimal energy scheme is higher when compared with the equal energy transmission. Even at an extremely low SNR of -10.7dB , the value of Δ remains greater than 1 for the proposed energy allocation scheme whereas it falls below 1 with equal transmit energies.

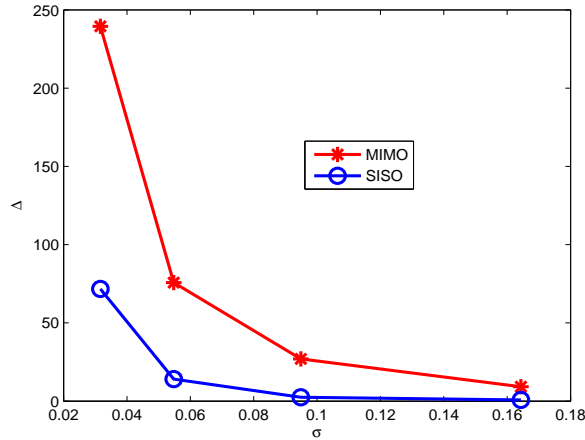


Figure 5.7: Performance metric Δ for MIMO and SISO systems as a function of the noise level σ .

Next, we demonstrate the improvement offered by the MIMO system over conventional SISO systems. This improvement is a result of the spatial diversity provided by distributed MIMO radar. We get multiple views of the target in MIMO radar. In Fig. 5.7, we see that MIMO system significantly outperforms the SISO system. For the SISO system, we considered transmitter and receiver to be present at the locations \vec{t}_1

and \vec{r}_1 , respectively. For fairness of comparison, we increased the number of samples per each pulse by a factor of $M_T M_R$ for the SISO system.

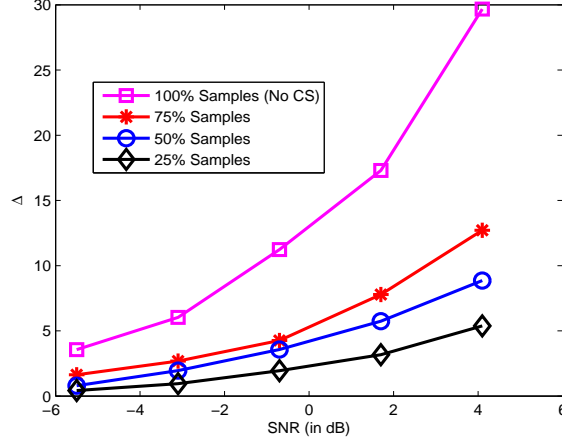


Figure 5.8: Performance metric Δ for different percentages of samples.

Now, we shall present the results for compressive sensing. As we defined earlier, the percentage of samples used is given by

$$\frac{N_{CS}}{NM_T M_R} \times 100\%. \quad (5.42)$$

We plot the performance of MIMO radar for different percentages of samples used. As expected, we observe from Fig. 5.8 that the performance degrades as the percentage of samples reduces. However, even while using just 25% of the samples, we can obtain $\Delta > 1$ for SNR as low as -3.5 dB. In other words, the reconstructed estimates of the position and velocity match the true values at an SNR of -3.5 dB while using only 25% of the samples. We used 25 independent Monte Carlo runs to produce these results.

We show the advantages of optimal energy allocation even for the compressive sensing scenario. From Fig. 5.9, we observe that the optimal choice of transmit energies gives

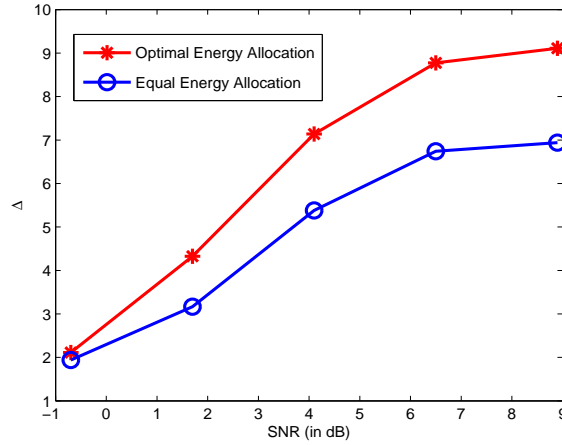


Figure 5.9: Performance metric Δ with and without adaptive energy allocation with 25% of samples.

significant improvement in performance even when we have just 25% of the samples. The reconstructed vectors for an SNR of 3.7dB are plotted in Fig. 5.10. We can see an equalization effect even here.

Finally, we wish to investigate the performance of the sparse recovery algorithm when there are modeling errors. More specifically, the targets may not fall exactly on the grid points. This can be a result of the grid size not being small enough. Also, the movement of the targets within the processing intervals can also lead to these modeling errors. We quantify the modeling error in each dimension as a percentage of the maximum possible error in that dimension. The maximum possible error is half the grid size in that dimension. Fig. 5.11 shows the reconstructed vector in the presence of 20% modeling error in both the x and y dimensions for each of the 3 targets. We observe that at an SNR of 3.7dB, the target parameters are mapped to the nearest grid points even in the presence of 20% modeling error. Note that we considered simultaneous errors in all the targets in both the dimensions. The system can handle larger errors when we consider the modeling errors separately. Fig. 5.12

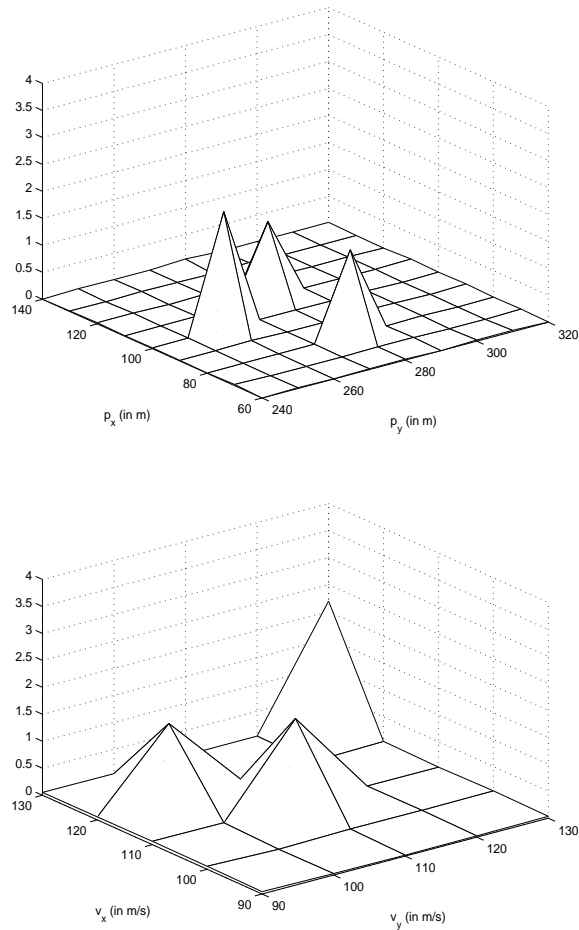


Figure 5.10: Reconstructed vectors with optimal energy allocation at SNR=3.7dB using 25% of the samples, (a) position estimates, (b) velocity estimates.

shows the reconstructed vector in the presence of 95% modeling error in only the y dimension for one of the 3 targets. We observe that at an SNR of 3.7dB, the target parameters are mapped to the nearest grid points even in the presence of 95% modeling error. Further, by including more pulses within a processing interval, the system can increase its robustness.

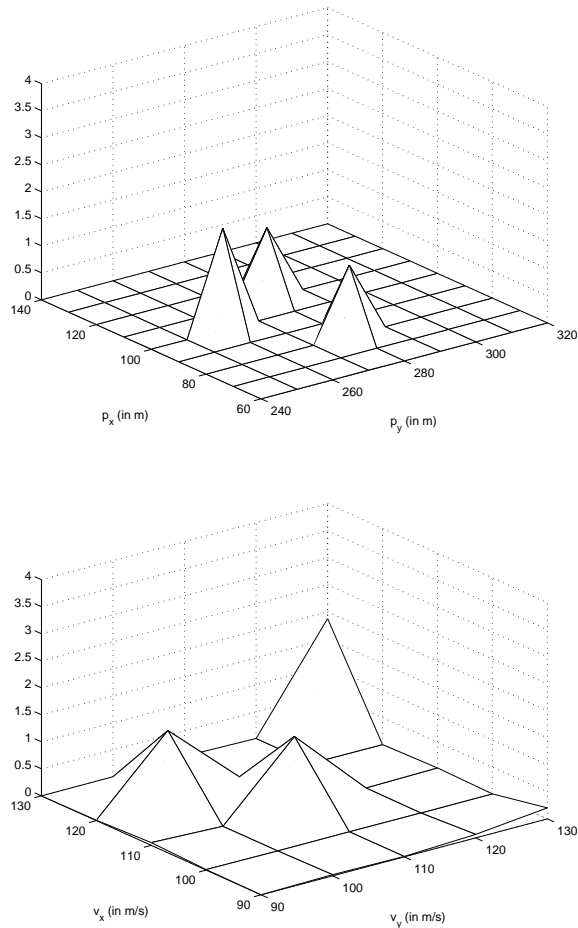


Figure 5.11: Reconstructed vectors with optimal energy allocation at SNR=3.7dB with 20% modeling errors in all the targets, (a) position estimates, (b) velocity estimates.

5.7 Summary

In this chapter, we used a novel approach to estimate the positions and velocities of multiple targets using MIMO radar systems with widely separated antennas by employing sparse modeling and compressive sensing. We also proposed a new metric to analyze the performance of these systems. We then developed an adaptive optimal energy allocation mechanism to get significant improvement in performance. We used

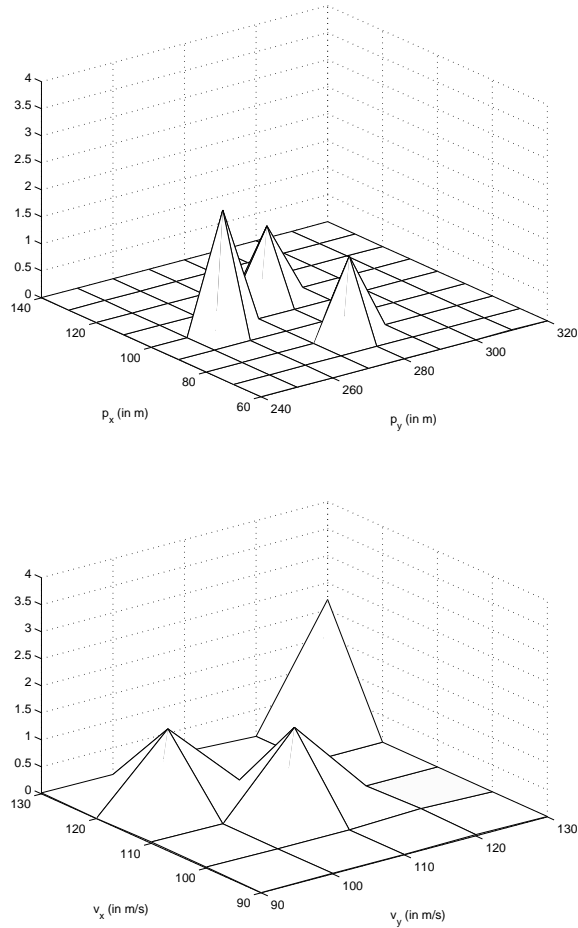


Figure 5.12: Reconstructed vectors with optimal energy allocation at SNR=3.7dB with 95% modeling errors in one of the targets in one dimension, (a) position estimates, (b) velocity estimates.

numerical simulations to demonstrate this improvement. We demonstrated that by employing compressive sensing, we can accurately reconstruct the target properties from very few samples. Finally, we showed that the proposed system is robust to modeling errors that may arise due to the discretization of the target state space.

In future work, we shall extend our results in this chapter to the case of extended targets. In such a scenario, the multiple targets will have impulse responses as opposed to a single reflection coefficient that we use for point targets. Further, we will model

the grid mismatch error using scaled von Mises distribution and analyze the estimation performance. Uniform distribution is a special case of von Mises distribution. Von Mises distribution is commonly used for modeling phase errors in radar problems [78] since the phase is bounded between $[-\pi, \pi]$. Since the grid error is bounded by half the grid size, scaled von Mises distribution fits this problem well.

Chapter 6

Frequency-hopping Code Design for MIMO Radar Estimation Using Sparse Modeling⁵

6.1 Introduction

In this chapter, we employ sparse modeling to estimate the unknown parameters of multiple targets using a pulsed colocated MIMO radar system that transmits frequency-hopping waveforms (see also [79], [80], [81]). More specifically, we formulate the measurement model using a block sparse representation. Further, we adaptively design the parameters of the transmitted waveforms to achieve improved performance. First, we derive analytical expressions for the correlations between the different columns of the sensing matrix. Next, we use this result for optimal design by computing the block coherence measure of the sensing matrix and selecting the

⁵Based on S. Gogineni and A. Nehorai, “Frequency-hopping code design for MIMO radar estimation using sparse modeling,” *IEEE Trans. Signal Process.*, to appear in. ©[2012] IEEE.

hopping frequencies of all the transmitters. Finally, we transmit constant modulus waveforms using these selected frequencies to estimate the Radar Cross Section (RCS) values of all the targets. We use these RCS estimates to adaptively design the amplitudes of the transmitted waveforms during each hopping interval for achieving improved sparse recovery performance.

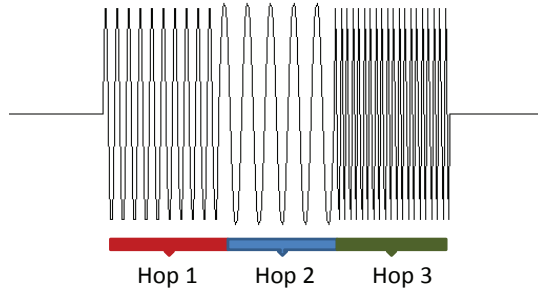


Figure 6.1: Example of a frequency hopping waveform with three hopping intervals.

6.2 Signal Model

We consider the problem of target estimation using a colocated MIMO radar system operating in a monostatic configuration. We assume there are M_T transmit antennas and M_R receive antennas arranged in linear arrays (see Fig. 6.2). The components of the transmit and receive arrays are separated by a distance of d_T and d_R , respectively. Further, we assume that these arrays form an angle θ with the target. The i^{th} transmitter emits frequency hopping waveform $u_i(t)$ (see Fig. 6.1). These waveforms are a generalization of linear frequency-modulated (LFM) waveforms. LFM is a special case of frequency hopping waveforms. In LFM, the frequency changes at the same linear rate, whereas for these codes the rate need not necessarily be linear as depicted in Fig. 6.1. In [82], the authors demonstrate the performance improvement

offered by these codes over LFM. Further, we consider a pulsed radar system in this chapter. Assuming L pulses make up a waveform, the signal from the i^{th} transmitter is given as

$$u_i(t) = \sum_{l=0}^{L-1} \phi_i(t - T_l), \quad (6.1)$$

where

$$\phi_i(t) = \sum_{q=0}^{Q-1} b_{i,q} e^{j2\pi c_{i,q} \Delta f t} s(t - q\Delta t), \quad (6.2)$$

and

$$s(t) = \begin{cases} 1, & \text{if } 0 < t < \Delta t, \\ 0, & \text{otherwise.} \end{cases} \quad (6.3)$$

T_l and Δt denote the pulse repetition interval and hopping interval duration, respectively. q and Q denote the hopping index and the total number of hopping intervals, respectively.

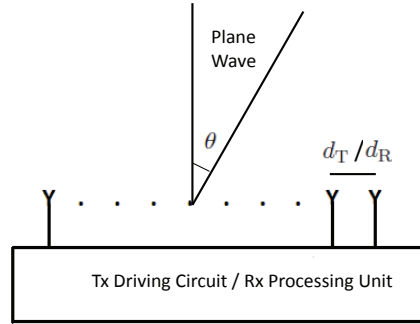


Figure 6.2: Transmit/Receive antenna array.

Design of the transmit waveforms amounts to choosing $c_{i,q}$ and $b_{i,q}$ for all the transmitters and all the hopping intervals. $c_{i,q}$ specifies the frequency of the transmitted signal during each hopping interval and $b_{i,q}$ gives the corresponding amplitude of the transmitted sinusoid. We assume that each $c_{i,q}$ takes a value from the set $\{1, \dots, G\}$, where G is a positive integer. We assume $\Delta f \Delta t = 1$. Further, to ensure orthogonality

of the waveforms for zero lag, we assume that for every hopping interval q ,

$$c_{i,q} \neq c_{i',q}, \forall i \neq i'. \quad (6.4)$$

We can arrange $c_{i,q}$ into an $M_T \times Q$ dimensional code matrix \mathbf{C} . This code matrix describes all the transmitted frequencies. Further, we constrain the amplitudes to satisfy $b_{\min} \leq |b_{i,q}| \leq b_{\max}$ for all transmitters and frequencies. This requirement ensures control over the peak-to-average-power ratio of all the transmitted radar waveforms. Further, we normalize the transmitted energy for each waveform by assuming $\sum_{q=0}^{Q-1} |b_{i,q}|^2 = 1$.

Define

$$f = \frac{d_R \sin(\theta)}{\lambda}, \quad (6.5)$$

$$\gamma = \frac{d_T}{d_R}, \quad (6.6)$$

where λ is the wavelength of the carrier. We assume that the target is made up of multiple individual isotropic scatterers. But, because of signal bandwidth constraints, these individual scatterers cannot be resolved. Therefore, we express this collection of scatterers as one point scatterer representing the RCS center of gravity [2], [70]. Further, we assume that different scattering centers of the target resonate at different frequencies [83]. Therefore, the target has an RCS that varies with the frequencies of the waveforms. Note that unlike distributed MIMO radar, the RCS does not vary with the antenna index for colocated MIMO radar.

The received signal at each receiver is a linear combination of the target-reflected waveforms from all the transmitters. Therefore, we can express the received signal at

the k^{th} receiver as

$$y_k(t) = \sum_{i=1}^{M_T} \sum_{l=0}^{L-1} \sum_{q=0}^{Q-1} a_{i,q} b_{i,q} e^{j2\pi c_{i,q} \Delta f (t - T_l - \tau)} s(t - q\Delta t - T_l - \tau) e^{j2\pi \nu t} e^{j2\pi f(\gamma i + k)} + e_k(t), \quad (6.7)$$

where τ and ν represent the delay and Doppler, respectively, and $e_k(t)$ denotes the additive noise at the k^{th} receiver. The target RCS is given by $a_{i,q}$. Note that we consider transmit waveforms whose bandwidth is much smaller when compared with the carrier frequency. Equation (7.6) gives the measurement model when a single target is present in the region illuminated by the MIMO radar system.

Now, we consider the presence of multiple targets. Consider R targets in the scene illuminated by the radar. Here we assume that all the targets are present in the far-field. Therefore, each of them makes an angle approximately equal to θ with the radar arrays. Then, the received signal at the k^{th} receiver is a summation of the reflections from all the targets. We sample the received signal to obtain

$$y_k(n) = \sum_{i=1}^{M_T} \sum_{l=0}^{L-1} \sum_{q=0}^{Q-1} \sum_{r=1}^R a_{i,q}^r b_{i,q} e^{j2\pi c_{i,q} \Delta f (nT_S - T_l - \tau^r)} \times s(nT_S - q\Delta t - T_l - \tau^r) e^{j2\pi \nu^r nT_S} e^{j2\pi f(\gamma i + k)} + e_k(n), \quad \forall n = 1, \dots, N,$$

where N denotes the total number of samples at each receiver during one processing interval and T_S denotes the corresponding sampling interval. Further, τ^r and ν^r represent the delay and Doppler of the r^{th} target, respectively.

6.3 Sparse Representation

Recently, sparse modeling is being used increasingly for solving radar problems by exploiting sparsity in the target delay-Doppler space [62], [64], [65], [69]. In this section, we will use sparse modeling to represent the radar measurements given in the previous section. These measurements can be captured using a block sparse model. For each of the R targets, the unknown parameters are the attenuation, delay, and Doppler. We shall discretize the delay-Doppler space into V uniformly spaced grid points. Only R of these grid points correspond to the true target parameters, and the goal is to estimate the correct grid points. Let τ_v and ν_v represent the delay and Doppler corresponding to the v^{th} grid point.

For each grid point $v \in \{1, \dots, V\}$, we define

$$\psi_{i,k,q}(n, v) = \sum_{l=0}^{L-1} e^{j2\pi c_{i,q}\Delta f(nT_S - T_l - \tau_v)} s(nT_S - q\Delta t - T_l - \tau_v) e^{j2\pi\nu_v nT_S} e^{j2\pi f(\gamma_i + k)}. \quad (6.8)$$

We stack $\{\psi_{i,k,q}(n, v)\}_{n=1}^N$ into an N dimensional column vector

$$\boldsymbol{\psi}_{i,k,q}(v) = [\psi_{i,k,q}(1, v), \dots, \psi_{i,k,q}(N, v)]^T, \quad (6.9)$$

where $\{\cdot\}^T$ denotes the transpose of $\{\cdot\}$.

Similarly, we stack $\{\boldsymbol{\psi}_{i,k,q}(v)\}_{k=1}^{M_R}$ into an NM_R dimensional column vector $\boldsymbol{\psi}_{i,q}(v)$. Each of these column vectors corresponds to a different transmitter and hopping interval, and we stack the columns corresponding to the same hopping interval together. Now, for each grid point v , we stack the column vectors into an $NM_R \times M_T Q$ dimensional matrix $\boldsymbol{\Psi}(v)$. Further, we arrange $\{\boldsymbol{\Psi}(v)\}_{v=1}^V$ into an $NM_R \times VM_T Q$

dimensional matrix Ψ . This is the dictionary matrix that defines the basis elements of our sparse representation.

Stacking $a_{i,q}^r$ and $a_{i,q}^r b_{i,q}$ corresponding to different transmitters and hopping intervals, we obtain $M_T Q$ dimensional column vectors \mathbf{a}^r and \mathbf{x}^r , respectively. Next, we define sparse vectors $\mathbf{a}(v)$ and $\mathbf{x}(v)$ whose support set and entries are given as

$$\mathbf{a}(v) = \begin{cases} \mathbf{a}^r, & \text{if } (\tau_v, \nu_v) = (\tau^r, \nu^r), \\ \mathbf{0}, & \text{otherwise,} \end{cases} \quad (6.10)$$

$$\mathbf{x}(v) = \begin{cases} \mathbf{x}^r, & \text{if } (\tau_v, \nu_v) = (\tau^r, \nu^r), \\ \mathbf{0}, & \text{otherwise.} \end{cases} \quad (6.11)$$

Finally, we stack these vectors $\mathbf{a}(v)$ and $\mathbf{x}(v)$ corresponding to all the grid points to obtain a $V M_T Q$ dimensional block-sparse vectors:

$$\mathbf{a} = [\mathbf{a}(1)^T, \dots, \mathbf{a}(V)^T]^T, \quad (6.12)$$

$$\mathbf{x} = [\mathbf{x}(1)^T, \dots, \mathbf{x}(V)^T]^T. \quad (6.13)$$

These sparse vectors contains only R non-zero blocks, each corresponding to a different target. Further, each block contains $M_T Q$ entries. Therefore $(V - R) M_T Q$ entries of \mathbf{x} are zeros.

We stack the measurements and the additive noise samples at each receiver to obtain the vectors

$$\mathbf{y}_k = [y_k(1), \dots, y_k(N)]^T, \quad (6.14)$$

$$\mathbf{e}_k = [e_k(1), \dots, e_k(N)]^T. \quad (6.15)$$

Additionally, stacking the measurement and noise vectors at all the receivers, we obtain

$$\mathbf{y} = [\mathbf{y}_1^T, \dots, \mathbf{y}_{M_R}^T]^T, \quad (6.16)$$

$$\mathbf{e} = [\mathbf{e}_1^T, \dots, \mathbf{e}_{M_R}^T]^T. \quad (6.17)$$

Then, our measurement model reduces to

$$\mathbf{y} = \mathbf{\Psi}\mathbf{x} + \mathbf{e}. \quad (6.18)$$

This is a familiar linear model used in most applications of sparse modeling.

The estimation of attenuation, delay, and Doppler for all the targets reduces to recovering the non-zero entries and the support set of the sparse vector \mathbf{x} from the measurement vector \mathbf{y} . In Section 6.6, we will present a sparse support recovery algorithm.

6.4 Block Coherence Measure

In this section, we will analyze the performance of the sparsity-based estimation approaches as a function of the sensing matrix Ψ . The correlations between the columns of the dictionary matrix Ψ determine the accuracy of sparse-recovery algorithms. More specifically, when the non-zero entries of the sparse vector appear in blocks (as in our radar estimation problem), a major factor affecting the performance of the system is the block coherence measure [75], [84]. This concept is an extension of the well-known coherence measure [56] used to block sparse signals. It can be used to derive sufficient conditions for guaranteed sparse support recovery.

Let $\Psi(v)$ and $\Psi(v')$ denote the v^{th} and v'^{th} blocks of the dictionary, respectively. Each block contains $M_T Q$ columns. Each column corresponds to a different transmitter and hopping interval. Since the columns corresponding to different hopping intervals do not overlap and, further, we imposed the condition in (6.4) to ensure orthogonality across all the transmitters for zero lag, all the columns within a block are orthogonal.

If any columns of $\Psi(v)$ are exactly the same as the corresponding columns in $\Psi(v')$, we can remove them, since they will not contribute to the sparse recovery problem while comparing these two blocks. Therefore, we define

$$D_{v,v'} = M_T Q - d_{v,v'}, \quad (6.19)$$

where $d_{v,v'}$ denotes the number of columns of $\Psi(v)$ that are exactly the same as the corresponding columns of $\Psi(v')$. Let us define the correlation matrix $\mathbf{M}[v, v']$ for

each pair of blocks of the dictionary matrix Ψ as

$$\mathbf{M}[v, v'] = \Psi^H(v)\Psi(v'). \quad (6.20)$$

Each entry of this matrix contains the auto-correlation between the different columns of the selected blocks. Using these notations, the authors in [75] defined the block coherence measure of the basis matrix as

$$\mu_B = \max_{v, v' \neq v} \frac{1}{D_{v, v'}} \rho(\mathbf{M}[v, v']), \quad (6.21)$$

where $\rho(\mathbf{M}[v, v'])$ denotes the spectral norm [85] of $\mathbf{M}[v, v']$:

$$\rho(\mathbf{M}[v, v']) = \frac{1}{D_{v, v'}} \lambda_{\max}^{\frac{1}{2}} \left(\mathbf{M}[v, v']^H \mathbf{M}[v, v'] \right), \quad (6.22)$$

where $\lambda_{\max}(\cdot)$ denotes the largest eigenvalue of (\cdot) .

The block coherence measure provides a sufficiency measure for ensuring sparse support recovery [75]. Therefore, minimizing the block coherence measure ensures theoretical guarantee for sparse support recovery of signals with potentially higher sparsity level. In the next section, we will use this concept to select the hopping frequencies of all the transmitters.

6.5 Optimal Hopping-Frequency Design

In this section, we present a mechanism for designing optimal hopping frequencies. The expression for the block coherence measure μ_B given in equation (6.21) depends

on the transmitted code matrix \mathbf{C} through the correlation matrices $\mathbf{M}[v, v']$. First, we will formulate the frequency-selection problem using the theory developed in the previous sections. Next, we develop a solution mechanism for this problem to obtain the code matrix.

6.5.1 Problem Formulation

In order to compute the optimal code matrix, we need to minimize the block coherence measure by solving the following optimization problem:

$$\mathbf{C}_{\text{opt}} = \underset{\mathbf{C}}{\operatorname{argmin}} (\mu_{\text{B}}), \quad (6.23)$$

$$= \underset{\mathbf{C}}{\operatorname{argmin}} \left(\max_{v, v' \neq v} \frac{1}{D_{v, v'}} \rho(\mathbf{M}[v, v']) \right), \quad (6.24)$$

$$= \underset{\mathbf{C}}{\operatorname{argmin}} \left(\max_{v, v' \neq v} \frac{1}{D_{v, v'}} \lambda_{\max}^{\frac{1}{2}} \left(\mathbf{M}[v, v']^H \mathbf{M}[v, v'] \right) \right). \quad (6.25)$$

The correlation matrices are obtained from the basis matrix using equation (6.20).

Substituting this relation into the above expression, we obtain

$$\mathbf{C}_{\text{opt}} = \underset{\mathbf{C}}{\operatorname{argmin}} \left(\max_{v, v' \neq v} \frac{1}{D_{v, v'}} \lambda_{\max}^{\frac{1}{2}} \left(\mathbf{\Psi}^H(v') \mathbf{\Psi}(v) \mathbf{\Psi}^H(v) \mathbf{\Psi}(v') \right) \right). \quad (6.26)$$

6.5.2 Correlation Matrix Entries

Since directly computing the block coherence measure is difficult, we first compute the entries of the correlation matrix $\mathbf{M}[v, v']$. Let $M_{rc}[v, v']$ represent the $(r, c)^{\text{th}}$ element of $\mathbf{M}[v, v']$ such that $r = qQ + i$ and $c = q'Q + i'$, where $q, q' \in \{0, \dots, Q - 1\}$ and $i, i' \in \{1, \dots, M_{\text{T}}\}$. Note that there is always a unique mapping between r and

(i, q) ; similarly between c and (i', q') . Therefore, we will alternatively use the notation $M_{iq, i'q'}[v, v']$ instead of $M_{rc}[v, v']$. Let grid point v correspond to the delay-Doppler pair (τ_v, ν_v) . Further, let grid point v' correspond to the delay-Doppler pair $(\tau_{v'}, \nu_{v'})$. Below, we state the assumptions made for performing the subsequent derivations.

We assume that the difference between the delays of any two grid points $(\tau_v - \tau_{v'})$ is always a multiple of the duration of the hopping interval Δt . Additionally, we assume that Δt is the size of the delay grid. Therefore, it gives us the range resolution of the sparsity-based radar estimation. Further, the target velocity components that are orthogonal to the radial direction (radar array to the target) do not produce a Doppler shift. The radial speeds of the targets are much smaller than the speed of wave propagation in the medium. We assume that the sampling rate is at least as big as the Nyquist rate corresponding to the largest possible hopping frequency:

$$\frac{1}{T_s} \geq 2G\Delta f. \quad (6.27)$$

Therefore, for all choices of coding matrices, we meet the Nyquist sampling criterion.

Then, we obtain the following expressions for the auto-correlations between the different columns of the blocks corresponding to v and v' :

$$\begin{aligned}
M_{rc}[v, v'] &= M_{iq, i'q'}[v, v'] \\
&= \sum_{k=1}^{M_R} \sum_{n=1}^N \sum_{l=0}^{L-1} e^{j2\pi(c_{i',q'}\Delta f(nT_S - T_l - \tau_{v'}) - c_{i,q}\Delta f(nT_S - T_l - \tau_v))} \\
&\quad \times s(nT_S - q'\Delta t - T_l - \tau_{v'})s(nT_S - q\Delta t - T_l - \tau_v) \\
&\quad \times e^{j2\pi(\nu_{v'}nT_S - \nu_v nT_S)} e^{j2\pi(f(\gamma i' + k) - f(\gamma i + k))}, \\
&= M_R \sum_{n=1}^N \sum_{l=0}^{L-1} e^{j2\pi\Delta f((c_{i',q'} - c_{i,q})(nT_S - T_l) + (c_{i,q}\tau_v - c_{i',q'}\tau_{v'}))} \\
&\quad \times s(nT_S - q'\Delta t - T_l - \tau_{v'})s(nT_S - q\Delta t - T_l - \tau_v) \\
&\quad \times e^{j2\pi(nT_S(\nu_{v'} - \nu_v) + f\gamma(i' - i))}.
\end{aligned}$$

Each column of the dictionary contains delay-Doppler shifted versions of the transmitted waveforms. Since we chose radar waveforms that have a bounded temporal support (rectangular pulses multiplied by sinusoids), the columns have only a few non-zero samples. All the other column entries are zero. The expression inside the summation will be non-zero only when the corresponding entries of both the columns are non-zero. Therefore, we can express the term inside the summation as

$$e^{j2\pi(\Delta f(c_{i',q'} - c_{i,q})(nT_S - T_l) + \Delta f(c_{i,q}\tau_v - c_{i',q'}\tau_{v'}) + nT_S(\nu_{v'} - \nu_v) + f\gamma(i' - i))}, \quad (6.28)$$

only when

$$q\Delta t < nT_S - T_l - \tau_v < (q + 1)\Delta t, \quad (6.29)$$

and

$$q'\Delta t < nT_S - T_l - \tau_{v'} < (q' + 1)\Delta t. \quad (6.30)$$

All other entries of the summation will be zero.

These conditions ensure that the rectangular pulses corresponding to both columns overlap at the given temporal index. For a given q, q', v, v' we denote as \mathcal{L} and $\mathcal{N}(\mathcal{L})$ the sets containing all l and n satisfying the conditions in (6.29) and (6.30). Note that for each pulse index, the sample indices that give non-zero entries are different. Then, we can express the entries of the correlation matrix as

$$M_{iq,i'q'}[v, v'] = M_{\text{R}} \sum_{(l,n) \in \mathcal{L} \times \mathcal{N}(\mathcal{L})} e^{j2\pi(\Delta f(c_{i',q'} - c_{i,q})(nT_{\text{S}} - T_l) + \Delta f(c_{i,q}\tau_v - c_{i',q'}\tau_{v'}) + nT_{\text{S}}(\nu_{v'} - \nu_v) + f\gamma(i' - i))}. \quad (6.31)$$

The exponential term on the right side, $e^{j2\pi f\gamma(i' - i)}$, is constant and does not depend on the time index; hence, it can be moved out of the summation. After removing this term, each entry of matrix $\mathbf{M}[v, v']$ is a summation of the product of complex exponentials, $e^{j2\pi(c_{i',q'}\Delta f(nT_{\text{S}} - T_l - \tau_{v'}) - c_{i,q}\Delta f(nT_{\text{S}} - T_l - \tau_v))}$ and $e^{j2\pi nT_{\text{S}}(\nu_{v'} - \nu_v)}$.

Let N_c be the number of samples per hopping interval. In other words, $N_c T_{\text{S}} = \Delta t$. Since the radial speeds of the targets are much smaller than the speed of wave propagation in the medium, the Doppler shift is measurable only between pulses and is negligible within the pulse duration. Therefore, we can express the correlation terms as a product of separate summations:

$$M_{iq,i'q'}[v, v'] = M_{\text{R}} e^{j2\pi f\gamma(i' - i)} \sum_{l \in \{0, \dots, L-1\}} e^{j2\pi T_l(\nu_{v'} - \nu_v)} \quad (6.32)$$

$$\times \sum_{\tilde{n} \in \{0, \dots, N_c - 1\}} e^{j2\pi \Delta f(c_{i',q'} - c_{i,q})\tilde{n}}. \quad (6.33)$$

The above equation contains three product terms. The first term is independent of the temporal index. The second term represents the contribution between the L

different pulses, and the third term represents the contribution from within a hopping interval. The dependence of the third term on the code matrix is evident from the exponential. Note that the second term depends on the Doppler shift, which in turn depends on the frequency of the complex exponential. This frequency is a sum of the carrier frequency and the hopping frequency. Therefore, we conclude that the second and third terms in equation (6.32) depend on the code matrix (hopping frequencies).

Now, we give expressions for these terms as a function of the code matrix. Define f_c as the carrier frequency, η as the speed of wave propagation in the medium, and $(v^r, v^{r'})$ as the radial speeds corresponding to the grid points v and v' , respectively. Then, we have

$$\sum_{l \in \{0, \dots, L-1\}} e^{j2\pi T_l (\nu_{v'} - \nu_v)} = \sum_{l \in \{0, \dots, L-1\}} e^{j2\pi T_l \frac{1}{\eta} ((f_c + \Delta f c_{i', q'}) v^{r'} - (f_c + \Delta f c_{i, q}) v^r)}. \quad (6.34)$$

Even though the term in equation (6.34) depends on the code matrix, the dependence is negligible since it is absorbed by the carrier frequency term that is much larger when compared with the baseband code frequencies:

$$f_c \gg G\Delta f, \quad (6.35)$$

where $G\Delta f$ denotes the maximum hopping frequency. The summation of the samples of a complex exponential is zero for all T_S satisfying (6.27). Hence, we have

$$\sum_{\tilde{n} \in \{0, \dots, N_c - 1\}} e^{j2\pi \Delta f (c_{i', q'} - c_{i, q}) \tilde{n}} = \begin{cases} N_c, & \text{if } c_{i', q'} = c_{i, q}, \\ 0, & \text{otherwise.} \end{cases} \quad (6.36)$$

Finally we express the entries $M_{i_q, i'_{q'}}[v, v']$ of the correlation matrix corresponding to the blocks v and v' as

$$M_{i_q, i'_{q'}}[v, v'] = \begin{cases} M_{\text{R}} N_{\text{c}} e^{j2\pi f \gamma (i' - i)} \sum_{l \in \{0, \dots, L-1\}} e^{j2\pi T_l (\nu_{v'} - \nu_v)}, & \text{if } c_{i', q'} = c_{i, q}, \\ 0, & \text{otherwise.} \end{cases} \quad (6.37)$$

Note that the auto-correlation matrix $\mathbf{M}[v, v']$ need not be a Hermitian matrix since $M_{i_q, i'_{q'}}[v, v']$ need not be equal to $M_{i'_{q'}, i_q}^*[v, v']$ for all i, q, i', q' . Therefore, the spectral norm and spectral radius of $\mathbf{M}[v, v']$ are not the same. Thus, we need to compute the eigenvalues of $\mathbf{M}[v, v']^H \mathbf{M}[v, v']$ to evaluate the spectral norm of $\mathbf{M}[v, v']$.

6.5.3 Correlation Matrix Structure

We now partition $\mathbf{M}[v, v']$ into Q^2 sub-matrices $\left\{ \mathbf{M}^{qq'}[v, v'] \right\}_{q, q'=0}^{Q-1}$ each of dimensions $M_{\text{T}} \times M_{\text{T}}$ such that

$$M_{ii'}^{qq'}[v, v'] = M_{i_q, i'_{q'}}[v, v'], \quad (6.38)$$

where $M_{ii'}^{qq'}[v, v']$ is the (i, i') th element of $\mathbf{M}^{qq'}[v, v']$. We use this notation to study the structure of $\mathbf{M}[v, v']$ for different pairs of grid points.

Without loss of generality, assume $\tau_{v'} \geq \tau_v$. Then, we combine the conditions in (6.29) and (6.30) to obtain the following conditions:

$$q - q' < \frac{(\tau_{v'} - \tau_v)}{\Delta t} + 1, \quad (6.39)$$

and

$$q - q' > \frac{(\tau_{v'} - \tau_v)}{\Delta t} - 1. \quad (6.40)$$

Since $(\tau_{v'} - \tau_v)$ is a multiple of Δt , the above conditions yield only a maximum of one possible positive integer value for q such that $\mathbf{M}^{qq'}[v, v']$ is a non-zero matrix:

$$q = q' + \frac{(\tau_{v'} - \tau_v)}{\Delta t}. \quad (6.41)$$

When $q' + \frac{(\tau_{v'} - \tau_v)}{\Delta t} > Q - 1$, then $\mathbf{M}^{qq'}[v, v'] = \mathbf{0}$ for every choice of valid q . In such a scenario the entire q'^{th} column of blocks is filled with zero sub-matrices. Therefore, $\mathbf{M}[v, v']$ can be partitioned into a special structure of sub-matrices. It is a block-lower-triangular matrix whose non-zero blocks appear in a single diagonal line parallel to the principal diagonal. The distance between this line and the principal diagonal is given by $\frac{(\tau_{v'} - \tau_v)}{\Delta t}$.

For example, consider the difference between the delays $(\tau_{v'} - \tau_v) = 2\Delta t$, when the number of hopping intervals $Q = 4$. $\mathbf{M}[v, v']$ can be expressed as

$$\mathbf{M}[v, v'] = \begin{bmatrix} \mathbf{0} & \mathbf{0} & \mathbf{0} & \mathbf{0} & \mathbf{0} \\ \mathbf{0} & \mathbf{0} & \mathbf{0} & \mathbf{0} & \mathbf{0} \\ \mathbf{M}^{20}[v, v'] & \mathbf{0} & \mathbf{0} & \mathbf{0} & \mathbf{0} \\ \mathbf{0} & \mathbf{M}^{31}[v, v'] & \mathbf{0} & \mathbf{0} & \mathbf{0} \\ \mathbf{0} & \mathbf{0} & \mathbf{M}^{42}[v, v'] & \mathbf{0} & \mathbf{0} \end{bmatrix}. \quad (6.42)$$

Here, the distance between the principal diagonal and the diagonal line of non-zero blocks is 2. When we are comparing blocks whose grid points have the same delay but different Doppler, $\mathbf{M}[v, v']$ will be a block-diagonal matrix.

Computing $\mathbf{M}[v, v']^H \mathbf{M}[v, v']$ for matrices following this structure yields block-diagonal matrices whose non-zero diagonal blocks are given by the non-zero blocks in the diagonal line of the original matrix $\mathbf{M}[v, v']$. In the above example, we obtain

$$\mathbf{M}[v, v']^H \mathbf{M}[v, v'] = \text{diag} \left\{ \mathbf{M}^{20}[v, v']^H \mathbf{M}^{20}[v, v'], \mathbf{M}^{31}[v, v']^H \mathbf{M}^{31}[v, v'], \mathbf{M}^{42}[v, v']^H \mathbf{M}^{42}[v, v'], \mathbf{0}, \mathbf{0} \right\}.$$

Only when $\tau_{v'} = \tau_v$ will all the diagonal blocks of $\mathbf{M}[v, v']^H \mathbf{M}[v, v']$ be non-zero. All the diagonal blocks of $\mathbf{M}[v, v']^H \mathbf{M}[v, v']$ will be zero when

$$(\tau_{v'} - \tau_v) > (Q - 1)\Delta t. \quad (6.43)$$

This result is a consequence of the fact that for all delays that exceed $(Q - 1)\Delta t$, the radar waveforms do not have overlapping time intervals and hence they will be orthogonal.

6.5.4 Optimal Code Matrix Selection

We know from the properties of block-diagonal matrices that their largest eigenvalue can be expressed as the largest of the eigenvalues of each of the individual blocks. Using this property, we have

$$\lambda_{\max} \left(\mathbf{M}[v, v']^H \mathbf{M}[v, v'] \right) = \max_{q, q'} \left(\lambda_{\max} \left(\mathbf{M}^{qq'}[v, v']^H \mathbf{M}^{qq'}[v, v'] \right) \right). \quad (6.44)$$

Next, we substitute the above expression into equation (6.25). Then, the code design problem reduces to

$$\mathbf{C}_{\text{opt}} = \underset{\mathbf{C}}{\text{argmin}} \left(\max_{v, v' \neq v} \frac{1}{D_{v, v'}} \max_{q, q'} \left(\lambda_{\max}^{\frac{1}{2}} \left(\mathbf{M}^{qq'}[v, v']^H \mathbf{M}^{qq'}[v, v'] \right) \right) \right). \quad (6.45)$$

Let us define

$$\widetilde{\mathbf{M}}^{qq'}[v, v'] = \mathbf{M}^{qq'}[v, v']^H \mathbf{M}^{qq'}[v, v']. \quad (6.46)$$

Using the definition of $\mathbf{M}^{qq'}[v, v']$, we compute the (i, i') th element of the Hermitian matrix $\widetilde{\mathbf{M}}^{qq'}[v, v']$ as

$$\widetilde{M}_{i, i'}^{qq'}[v, v'] = \sum_{k'=1}^{M_T} M_{k', i, q'}^*[v, v'] M_{k', i', q'}[v, v']. \quad (6.47)$$

Therefore,

$$\widetilde{M}_{i, i'}^{qq'}[v, v'] = \begin{cases} |\alpha|^2 \xi_{iqi'q'} e^{j2\pi f \gamma(i' - i)}, & \text{if } c_{i, q'} = c_{i', q'}, \\ 0, & \text{otherwise,} \end{cases} \quad (6.48)$$

where

$$\alpha = M_R N_c \sum_{l \in \{0, \dots, L-1\}} e^{j2\pi T_l (\nu_{v'} - \nu_v)}, \quad (6.49)$$

and $\xi_{iqi'q'}$ denotes the number of elements in the q^{th} column of code matrix \mathbf{C} that have the same value as $c_{i, q'} = c_{i', q'}$.

Since we assumed orthogonality for zero lag in (6.4), $c_{i, q'} = c_{i', q'}$ if and only if $i = i'$.

Therefore, equation (6.48) can be reduced to

$$\widetilde{M}_{i, i'}^{qq'}[v, v'] = \begin{cases} |\alpha|^2 \xi_{iqi'q'}, & \text{if } i = i', \\ 0, & \text{otherwise.} \end{cases} \quad (6.50)$$

Therefore, $\widetilde{\mathbf{M}}^{qq'}$ $[v, v']$ is a diagonal matrix. Further, (6.4) also implies that $\xi_{iqiq'}$ can take values only from the set $\{0, 1\}$. Therefore,

$$\lambda_{\max}^{\frac{1}{2}} \left(\mathbf{M}^{qq'} [v, v']^H \mathbf{M}^{qq'} [v, v'] \right) = |\alpha|. \quad (6.51)$$

$|\alpha|$ depends only on the difference in the Doppler shifts corresponding to grid points v and v' , i.e., $(\nu_{v'} - \nu_v)$. Since $|\alpha|$ does not depend on the entries of the code matrix, it does not affect the code selection problem.

Also,

$$d_{v,v'} = \sum_{i,q,q'=q-\frac{(\tau_{v'}-\tau_v)}{\Delta t}} \xi_{iqiq'}. \quad (6.52)$$

Note that the summation is carried out only among columns that satisfy the condition in (6.41). Therefore, this summation varies with respect to the difference of delays, $\tau_v - \tau_{v'}$. Finally, substituting equations (6.51) and (6.52) into (6.45), the optimal code selection simplifies to the following:

$$\mathbf{C}_{\text{opt}} = \underset{\mathbf{C}}{\operatorname{argmin}} \left(\max_{v,v' \neq v} \frac{1}{D_{v,v'}} \right), \quad (6.53)$$

$$= \underset{\mathbf{C}}{\operatorname{argmax}} \left(\min_{v,v' \neq v} D_{v,v'} \right), \quad (6.54)$$

$$= \underset{\mathbf{C}}{\operatorname{argmin}} \left(\max_{v,v' \neq v} d_{v,v'} \right), \quad (6.55)$$

$$= \underset{\mathbf{C}}{\operatorname{argmin}} \left(\max_{v,v' \neq v} \sum_{i,q,q'=q-\frac{(\tau_{v'}-\tau_v)}{\Delta t}} \xi_{iqiq'} \right). \quad (6.56)$$

Define

$$\beta(\mathbf{C}) = \left(\max_{v, v' \neq v} \sum_{i, q, q' = q - \frac{(\tau_{v'} - \tau_v)}{\Delta t}} \xi_{iqiq'} \right). \quad (6.57)$$

Since $\beta(\mathbf{C})$ governs the performance of any code matrix \mathbf{C} , we will use it in Section 6.9 to show the improvement due to the optimal code design.

6.5.5 Iterative Exhaustive Search Algorithm for Code Selection

We observe that (6.53) is a combinatorial optimization problem, and these do not yield easily to direct solution. Further, the solution to this problem need not be unique. Any of the optimal solutions is equally good for our purpose. Thus, we will use an iterative approach to obtain an optimal code matrix. First, we notice from (6.53) that for any code matrix, the objective function is a non-negative integer. Therefore, we start with a desired objective function value of 0 (corresponding to no overlaps between the columns satisfying (6.41) for all differences in delays) and search for availability of codes satisfying this objective. If no such codes exist, we increment the objective function and follow the same procedure iteratively. We describe the steps in detail below.

This algorithm is implemented in two major loops. The outer loop corresponds to the desired objective value and the inner loop corresponds to the code column. Let \mathcal{G}^{M_T} denote a set containing all column vectors of size M_T whose entries are taken from $\{1, \dots, G\}$. Further, we avoid the repetition of entries within these columns to ensure orthogonality at zero lag. Let l_o and l_i denote the iteration indices of the outer and inner loops, respectively. For the first outer iteration, $l_o = 1$ and the corresponding

objective is $d^{(1)} = 0$. For the inner loop, we initialize by selecting any arbitrary column from the set of columns \mathcal{G}^{M_T} as the first column of our code matrix.

In every subsequent iteration, we increment the column index and add a column from \mathcal{G}^{M_T} that satisfies the following condition with regard to the already existing columns:

$$\sum_{i, l_i, q' = l_i - \frac{(\tau_{v'} - \tau_v)}{\Delta t}} \xi_{il_i q'} \leq d^{(l_o)}, \quad \forall v, v'. \quad (6.58)$$

If no such column exists, we decrement the column index and replace the existing column of the previous iteration with another alternative that satisfies (6.58). If we exhaust the inner loop without obtaining sufficient columns to complete the code matrix, we know that an objective of $d^{(l_o)}$ cannot be attained by any code matrix. Therefore, we increment the objective $d^{(l_o+1)} = d^{(l_o)} + 1$ for the next outer iteration and reset the inner loop index to $l_i = 0$.

We terminate the algorithm when we obtain a full (Q columns) code matrix from the inner loop satisfying the objective given by the outer-loop index. The code matrix obtained using this algorithm will always have the optimal objective function. However, the convergence times depend on Q , G , and M_T . Fig. 6.3 shows the major blocks used in the implementation of this algorithm. The column-selection block is very critical, as it controls the inner loop of the algorithm. It searches for a column in \mathcal{G}_T^M that satisfies (6.58). Depending on the result of this search, we increment or decrement the column index.

Note that there may be other efficient algorithms to solve (6.53) to obtain an optimal code matrix using combinatorial optimization. However, it is beyond the scope of this chapter to analyze the computational complexity and present the theory of

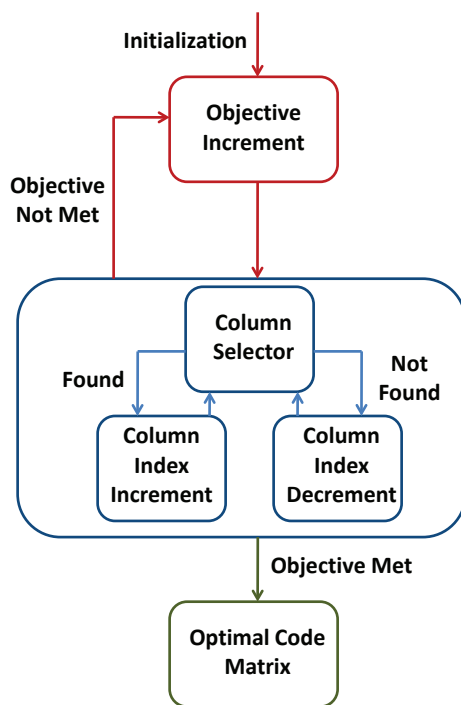


Figure 6.3: Flowchart of code selection algorithm.

combinatorial optimization for developing these alternate algorithms. We will explore these approaches as a future extension to our work. Further, this hopping-frequency (code matrix) design is done offline, whereas the amplitude design given later in the chapter is an online design procedure. Therefore, computational complexity is not a very critical issue when designing the code matrix.

6.6 Sparse Reconstruction

In this section, we present a reconstruction algorithm to recover the sparse vector \mathbf{s} from the noisy measurement vector \mathbf{y} . Ideally, in a noiseless scenario, we need to

solve the following optimization problem to recover the sparse vector

$$\min_{\mathbf{z}} \|\mathbf{z}\|_0 \quad \text{s.t.} \quad \mathbf{y} = \Psi \mathbf{z}. \quad (6.59)$$

However, this problem is NP hard. Therefore, this problem is relaxed to one that involves the l_1 norm, and several approaches have been proposed in the literature to solve it. In [74], a heuristic iterative approach called Matching Pursuit (MP) is presented. Further, [73], formulates the problem such that it can be solved using convex programming. Approaches such as Basis Pursuit (BP) and Basis Pursuit Denoising (BPDN) are popular in this category.

However, these algorithms do not exploit the fact that the non-zero entries of the sparse vector appear in blocks. Using the knowledge of block sparsity will improve recovery performance. In [75], the authors present block extension of matching pursuit algorithm known as Block Matching Pursuit (BMP). This algorithm is a direct extension of the conventional MP, and is used when the columns within the blocks of the dictionary matrix are orthogonal. We observed in Section 6.5 that the columns of $\Psi(v)$ are orthogonal since $c_{i,q} \neq c_{i',q}, \forall q, i' \neq i$. We start with an initial estimate of $\hat{\mathbf{x}} = \mathbf{0}$. Let $\hat{\mathbf{x}}(v)$ denote the components of the estimate corresponding to the v^{th} block. Further, we initialize the residue to be $\mathbf{r}^{(0)} = \mathbf{y}$. In each subsequent iteration l' , we project the residue onto each block of Ψ and pick the block that gives the maximum correlation with the residue:

$$\mathbf{v}_{\max}^{(l')} = \underset{v}{\operatorname{argmax}} \left(\Psi^H(v) \mathbf{r}^{(l'-1)} \right). \quad (6.60)$$

We update the residue as

$$\mathbf{r}^{(l')} = \mathbf{r}^{(l'-1)} - \mathbf{\Psi}^H(v_{\max}^{(l')})\mathbf{r}^{(l'-1)}\mathbf{\Psi}(v_{\max}). \quad (6.61)$$

Finally, we update the $v_{\max}^{(l')}$ block of the estimate vector as

$$\hat{\mathbf{x}}(v_{\max}^{(l')}) = \mathbf{\Psi}^H(v_{\max}^{(l')})\mathbf{r}^{(l'-1)}. \quad (6.62)$$

In a noiseless scenario, after R iterations, the estimate vector $\hat{\mathbf{x}}$ will converge to the true sparse vector \mathbf{x} . Further iterations will not result in a change in the residue or the estimate. In the presence of noise, some of the incorrect blocks may also contain non-zero entries.

Note that in the above expressions for sparse support recovery, we assumed that all the columns of $\mathbf{\Psi}$ have unit norm. When all of them are scaled by the same constant factor (non-unit norm), the update equations change by an appropriate scale factor corresponding to this norm. We will use BMP in Section 6.9 to perform sparse support recovery.

6.7 Adaptive Waveform Amplitude Design

6.7.1 Design

After we select hopping frequencies using the block coherence measure mentioned earlier, the transmitters emit constant modulus waveforms; i.e., $b_{i,q} = 1, \forall i, q$. We use sparse recovery algorithm (BMP) to estimate the unknown delay, Doppler, and RCS

of the targets. We perform the amplitude design for all the transmitters. We use the target RCS estimates to adaptively design the amplitudes of the sinusoids during each hopping interval of the subsequent pulses. Since the RCS of the targets are frequency dependent, the optimal amplitudes need not be the same for all hopping intervals. As we shall see later, this problem can be divided into independent optimization problems for each transmitter.

Let $\widehat{\mathbf{x}}$ denote the sparse vector reconstructed using the algorithm given in the previous section. If \mathcal{R} gives the support set corresponding to the R highest reconstruction energies in $\widehat{\mathbf{x}}$, then define $\widehat{\mathbf{x}}_{\mathcal{R}}$ as an R -dimensional vector containing only the estimates corresponding to the indices in \mathcal{R} . During the initialization step, since $b_{i,q} = 1$, the non-zero entries of the sparse vector \mathbf{x} depend only on the attenuations $a_{i,q}^r$. Hence, we obtain $\widehat{a}_{i,q}^r$ as the estimates of the target attenuations after sparse support recovery.

For all subsequent steps, the entries of $\widehat{\mathbf{x}}_{\mathcal{R}}$ contain the product of the transmitted amplitude and the target RCS ($b_{i,q}\widehat{a}_{i,q}^r$). We compute the summation of the energies of these estimates for each transmitter over all the hopping interval indices to obtain

$$\widehat{x}_i^r = \sum_{q=0}^{Q-1} b_{i,q}^2 |\widehat{a}_{i,q}^r|^2. \quad (6.63)$$

Further, let $b_{i,q}^*$ denote the optimal amplitude for the i^{th} transmitter and q^{th} frequency hop. We vectorize $b_{i,q}$ and $b_{i,q}^*$ for the i^{th} transmitter into \mathbf{b}_i , \mathbf{b}_i^* , respectively.

Define the vector

$$\widetilde{\mathbf{x}}_i(\mathbf{b}_i) = [\widehat{x}_i^1(\mathbf{b}_i), \dots, \widehat{x}_i^R(\mathbf{b}_i)]. \quad (6.64)$$

This vector contains the estimates of the returns from all the R targets. Note that here we assume that the indices in \mathcal{R} correspond to the true target entries; i.e, delay-Doppler estimates using sparse reconstruction are exact. Otherwise, incorrect indices will impact the amplitude design and degrade the performance. Using these definitions, the amplitude design problem for each transmitter can be expressed as

$$\mathbf{b}_i^* = \underset{\mathbf{b}_i}{\operatorname{argmax}} (\min \{\tilde{\mathbf{x}}_i(\mathbf{b}_i)\}), \quad (6.65)$$

under the constraints

$$b_{\min} \leq |b_{i,q}| \leq b_{\max}; \quad \sum_{q=0}^{Q-1} |b_{i,q}|^2 = 1, \quad (6.66)$$

where $\min \{\tilde{\mathbf{x}}_i(\mathbf{b}_i)\}$ denotes the minimum entry of the vector $\tilde{\mathbf{x}}_i(\mathbf{b}_i)$.

We will solve this optimization problem using `CVX`, a MATLAB package for specifying and solving convex programs [76], [77] after appropriate convex transformation (see also [67]). Note that we need to solve this optimization problem for each transmitter separately. Since the dimensions involved in solving these problems (number of targets and number of transmitters) are typically small, we can compute the optimal energies in quick time and implement the design online.

6.7.2 Metric

Next, we present a performance metric to analyze the accuracy of sparse reconstruction (see also [69], [67] for more details on this metric). Let \mathcal{R} and $\bar{\mathcal{R}}$ denote the support sets of the correct and incorrect target indices, respectively. Then, we define

the performance metric as

$$\Delta = \frac{\min \widehat{\boldsymbol{x}}_{\mathcal{R}}}{\max \widehat{\boldsymbol{x}}_{\bar{\mathcal{R}}}}. \quad (6.67)$$

The numerator of Δ denotes the weakest target reconstruction and the denominator denotes the strongest reconstruction of the incorrect target indices. Therefore, $\Delta > 1$ guarantees that the correct R target indices dominate the others, thereby resulting in exact estimates of the target delays and Dopplers. The exact value of Δ gives the accuracy in the estimates of the target RCS values.

In Section 6.9, we will demonstrate the improvement in performance as a result of the optimal transmit amplitude design when compared with the constant modulus waveforms by using this performance metric.

6.8 Compressive Sensing

In this section, we use compressive sensing to accurately reconstruct the sparse vector from far fewer samples when compared with the Nyquist rate. The theory of compressive sensing says that this is possible when the sensing matrix has minimal coherence with the dictionary matrix. Since random matrices have been shown in the literature [56] to give a low coherence measure, we will generate the entries of the sensing matrix as realizations of independent and identically distributed (i.i.d.) Gaussian random variables.

Let Φ denote an $N_{\text{CS}} \times NM_{\text{R}}$ dimensional random Gaussian sensing matrix, where $N_{\text{CS}} < NM_{\text{R}}$. Define $\boldsymbol{y}_{\text{CS}}$ as the measurement vector after compressive sensing. Then,

the measurement model in equation (7.12) changes to

$$\mathbf{y}_{\text{CS}} = \Phi\Psi\mathbf{x} + \Phi\mathbf{e}. \quad (6.68)$$

The sensors receive continuous data across all the pulses. This data is projected onto a finite lower dimensional space spanned by random continuous Gaussian noise sequences. The dimensions of this space are much smaller than the Nyquist rate. Therefore, we are actually sampling directly at a reduced rate. The above equation is just an equivalent way of representing the signal processing involved in this procedure.

Now we need to recover \mathbf{x} from the compressed measurement vector \mathbf{y}_{CS} . The reconstruction algorithm and design schemes presented in the earlier sections of the chapter are also valid for compressive sensing. We define the percentage of compression as

$$\delta = \frac{N_{\text{CS}}}{NM_{\text{R}}} \times 100\%. \quad (6.69)$$

The performance of the system degrades as the value of δ reduces. We will show this dependence in Section 6.9 for different values of δ .

6.9 Numerical Simulations

In this section, we present numerical simulations to demonstrate the performance of our proposed radar system.

6.9.1 Code Matrix Design

First, we will present examples for the code matrix selection. Let the number of transmitters be $M_T = 3$ and the number of hopping intervals be $Q = 5$. In addition, we chose $G = 7$. Therefore, the code matrix contains 15 entries, each chosen from $\{1, \dots, 7\}$. We ran the iterative algorithm for code selection and obtained the following code matrix as an optimal code:

$$\mathbf{C}_{\text{opt}} = \begin{bmatrix} 1 & 3 & 2 & 1 & 1 \\ 2 & 4 & 6 & 4 & 2 \\ 3 & 5 & 7 & 6 & 3 \end{bmatrix}. \quad (6.70)$$

For the first three iterations of the outer loop (i.e., $d^{(1)} = 0$, $d^{(2)} = 1$, and $d^{(3)} = 2$), the objective is not met. An objective of $d^{(4)} = 3$ is met by the code matrix in equation (6.70). Note that other code matrices may also give the same objective and provide equal performance. However, no other code matrix will give better performance. The block coherence measure corresponding to the following code is the same as that of the code matrix in (6.70):

$$\mathbf{C}_{\text{opt}} = \begin{bmatrix} 3 & 1 & 4 & 1 & 1 \\ 5 & 2 & 5 & 2 & 2 \\ 6 & 7 & 7 & 6 & 3 \end{bmatrix}. \quad (6.71)$$

Both are equally good for selecting the MIMO radar waveforms, and there is not any particular advantage in choosing one of them over the other for performing the target parameter estimation.

Now, we demonstrate the improvement in performance due to the hopping-frequency design by plotting $\beta(\mathbf{C})$ as a function of the number of hopping intervals Q . Note that we defined $\beta(\mathbf{C})$ in equation (6.57). Fig. 6.4 compares the curves for the optimal code matrix and a random code matrix whose columns are chosen uniformly from the set of possible columns. We average across 10000 Monte Carlo runs to obtain the curve for the random code matrix. $\beta(\mathbf{C})$ is a multiple of the block coherence measure. Therefore, we intend to have as low a $\beta(\mathbf{C})$ as possible. From Fig. 6.4, we observe that the optimal code matrix has much lower block coherence when compared with the average block coherence of the random code matrix. Having a lower $\beta(\mathbf{C})$ ensures theoretical guarantee for sparse support recovery of signals with potentially higher sparsity level [75]. Therefore, Fig. 6.4 essentially states that while using the random code matrix, we cannot guarantee sparse recovery for the same level of sparsity as we can for the optimal code word but for specific examples, it might reconstruct the targets correctly. However, it is not reliable as we do not have any guarantee on the performance at the higher levels of sparsity.

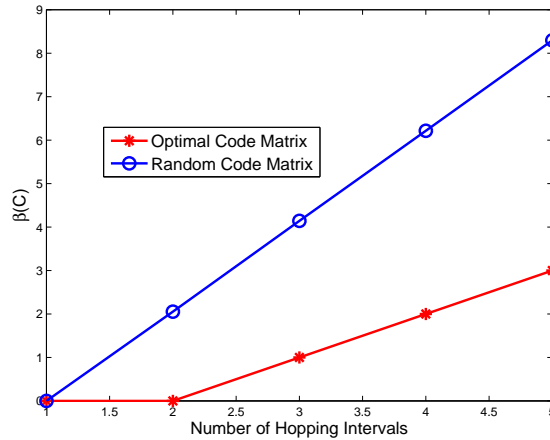


Figure 6.4: $\beta(\mathbf{C})$ as a function of the number of hopping intervals.

6.9.2 Sparse Support Recovery

In this section we simulated a radar system consisting of $M_R = 3$ receive antennas. Choose $\theta = 30^\circ$ and $d_T = d_R = \frac{\lambda}{2}$, obtaining $f = \frac{1}{4}$ and $\gamma = 1$. Each processing interval consists of 10 pulses (i.e., $L = 10$). The time interval in between the pulses was chosen to be 3mS. Let the chip duration be $\Delta t = 1\mu\text{S}$. Therefore, the width of each pulse $Q\Delta t = 5\mu\text{S}$. $\Delta f = 1\text{MHz}$ is the minimum frequency of the waveform inside a hopping interval. Since we chose $G = 7$, the maximum hopping frequency is $G\Delta f = 7\text{MHz}$. Therefore, we sampled at a Nyquist rate of 14×10^6 samples per second. During each chip duration, we have 14 samples.

Three targets are present in the illuminated space. Each target resonates differently at different frequencies. Therefore, we specify the amplitudes of $G = 7$ attenuations for each target:

$$\mathbf{a}^1 = [0.4, 0.2, 0.5, 0.8, 0.1, 0.4, 0.3], \quad (6.72)$$

$$\mathbf{a}^2 = [0.6, 0.2, 0.8, 0.9, 0.1, 0.3, 0.5], \quad (6.73)$$

$$\mathbf{a}^3 = [0.2, 0.4, 0.3, 0.7, 0.4, 0.1, 0.9]. \quad (6.74)$$

Using these attenuations, the target RCS corresponding to different hopping frequencies and transmitters can be found. Note that we use (6.70) as our choice of code matrix.

Now, we discretize the target delay-Doppler space. As we mentioned earlier, we assume that the grid size in the delay dimension is $\Delta t = 1\mu\text{S}$. The grid points lie uniformly in the interval $[0, 10] \mu\text{S}$. Note that this is just an example and the proposed approach can be applied to any arbitrary grid. In a live tracking system, the grid will

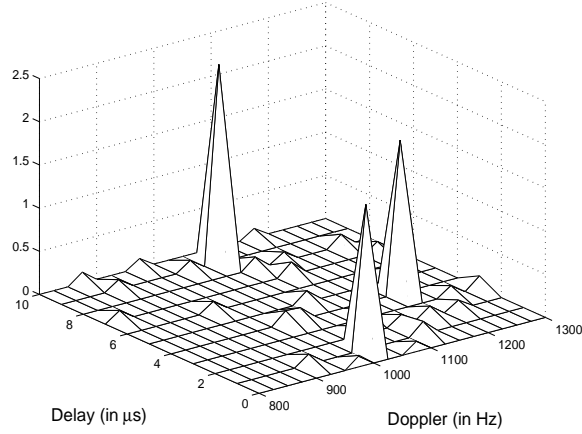


Figure 6.5: Target estimates using BMP at an SNR of 2.6574dB.

be adjusted to center around the delay estimate from the previous tracking interval. The Doppler space is uniformly divided in the interval $[800, 1300]$ Hz with a separation of 25Hz between adjacent grid points. Therefore, we have a total of $V = 11 \times 21 = 231$ grid points, with only 3 corresponding to the true targets.

We assume the true delays and Doppler shifts of the targets are given as

$$[\tau^1, \tau^2, \tau^3] = [4, 9, 1] \mu\text{S}, \quad (6.75)$$

$$[\nu^1, \nu^2, \nu^3] = [1200, 1075, 1025] \text{ Hz}. \quad (6.76)$$

Next, we perform sparse support recovery using the BMP algorithm to estimate the target parameters. We define the signal-to-noise-ratio (SNR) as

$$\text{SNR} = 10 \log \left(\frac{\|\Psi \mathbf{a}\|^2}{\mathbb{E}(\|\mathbf{e}\|^2)} \right) \text{ dB}, \quad (6.77)$$

where $\mathbb{E}\{\cdot\}$ denotes the expected value of $\{\cdot\}$.

First we show the reconstructed target parameters in Fig. 6.5 at an SNR of 2.6574dB. We observe that the delays and Doppler shifts of all three targets are exactly reconstructed. Since the true target indices dominate the incorrect target indices in the recovered vector, the value of the performance metric Δ will be greater than unity. We used 30 iterations for the BMP algorithm. We have assumed the target will lie exactly on the grid points. However, in reality it may lie in between two grid points. When such modeling errors occur, we have demonstrated in [67] that the reconstruction algorithm BMP will map the estimates to the grid point that is closest to the true target parameter. The same holds true even for the results in this chapter as we are using BMP.

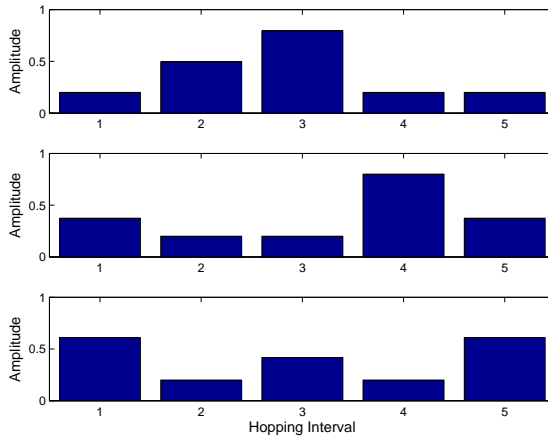


Figure 6.6: Amplitudes of waveforms from $M_T = 3$ transmitters.

6.9.3 Adaptive Waveform Amplitude Design

After selecting the hopping frequencies using the code matrices mentioned earlier in the section, we consider waveform amplitude selection. We need to solve $M_T = 3$ optimization problems. For each transmitter, we need to design 5 amplitudes, each corresponding to a different hopping interval. We constrain these amplitudes to lie in

the interval $[b_{\min}, b_{\max}] = [0.2, 0.8]$. Further, the sum of squares of these amplitudes is constrained to be unity. Using CVX to solve the amplitude selection problem, we obtain the following optimal transmit amplitudes:

$$\mathbf{b}_1^* = [0.2, 0.50, 0.80, 0.2, 0.2], \quad (6.78)$$

$$\mathbf{b}_2^* = [0.37, 0.2, 0.2, 0.8, 0.37], \quad (6.79)$$

$$\mathbf{b}_3^* = [0.61, 0.2, 0.42, 0.2, 0.61]. \quad (6.80)$$

In Fig. 6.6, we plot these amplitudes as a function of the hopping interval. We observe that the maximum energy for each transmitter need not be present during the same hopping interval. Transmitters 1 and 2 emit their maximum energy during the third and fourth hopping intervals, respectively. However, transmitter 3 emits its maximum energy during the first and fifth hopping intervals. It transmits equal energy during both these intervals, since the corresponding frequency entries of the code matrix in (6.70) are the same.

During each hopping interval, these waveforms are multiplied by exponential waveforms whose frequencies are given by the entries of the code matrix in (6.70). If we constrain the amplitudes such that

$$b_{\min} = b_{\max} = \frac{1}{\sqrt{Q}}, \quad (6.81)$$

then we will obtain constant-modulus waveforms. Such waveforms are useful when the variations in the amplitudes of the radar waveforms are not desired because of hardware constraints of the radar transmit antennas.

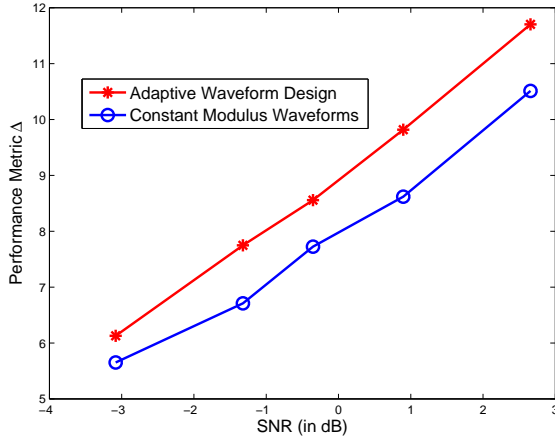


Figure 6.7: Curves demonstrating the improvement in performance due to adaptive amplitude design.

In Fig. 6.7, we plot the performance metric Δ to demonstrate the improvement offered by the adaptive amplitude design mechanism. Recall that we defined the performance metric as

$$\Delta = \frac{\min \hat{\mathbf{x}}_{\mathcal{R}}}{\max \hat{\mathbf{x}}_{\mathcal{R}}}. \quad (6.82)$$

We would like Δ to be as high as possible. $\Delta > 1$ assures exact reconstruction of the target delays and Dopplers. The exact value of Δ gives the accuracy in the estimates of the target RCS values. We observe that for all SNR, the adaptive amplitude design provides significant improvement in performance. This improvement is a result of maximizing the minimum target returns.

Now, we will demonstrate the improvement due to the adaptive design for a completely different choice of attenuations for the 3 targets:

$$\mathbf{a}^1 = [0.2, 0.9, 0.3, 0.4, 0.1, 0.7, 0.6], \quad (6.83)$$

$$\mathbf{a}^2 = [0.7, 0.8, 0.2, 0.6, 0.7, 0.3, 0.1], \quad (6.84)$$

$$\mathbf{a}^3 = [0.4, 0.7, 0.8, 0.1, 0.5, 0.1, 0.9]. \quad (6.85)$$

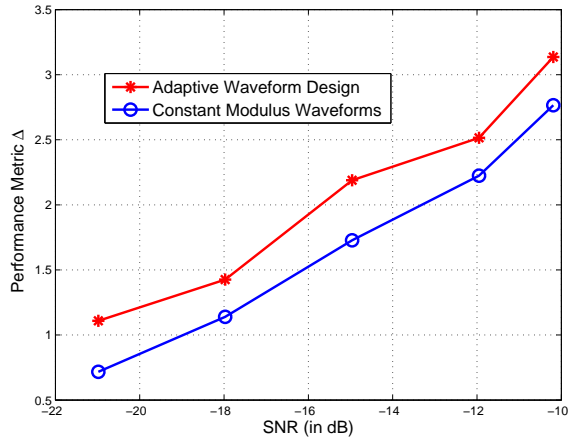


Figure 6.8: Curves demonstrating the improvement in performance due to adaptive amplitude design in the low SNR region.

Note that these attenuations are used only for the results in Figs. 8, 9, and 10. We perform the sparse support recovery under this scenario and plot the performance metric as a function of the SNR in Fig. 6.8. In this example, we demonstrate the performance at very low SNR to investigate the situation when the sparse reconstruction fails to estimate all the target parameters correctly.

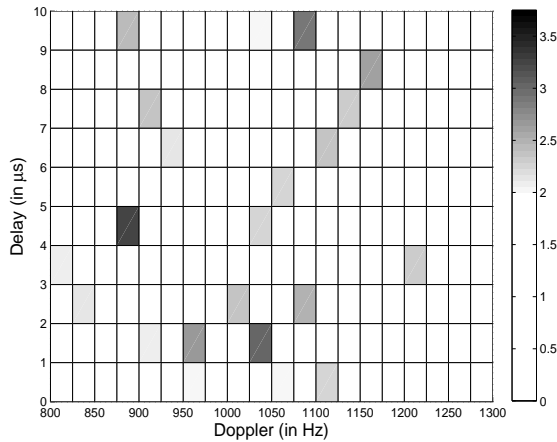


Figure 6.9: Target estimates using BMP at an SNR of -21dB .

We observe clearly from Fig. 6.8 that the adaptive amplitude design outperforms constant modulus waveforms even under this scenario. More specifically, we observe that the value of Δ falls below 1 for constant modulus waveform approximately at an SNR 2.5dB higher than for adaptive amplitude design. Therefore, constant modulus waveforms fail to estimate the true target parameters at an SNR of -21 dB whereas employing adaptive design enables exact reconstruction even at this low SNR.

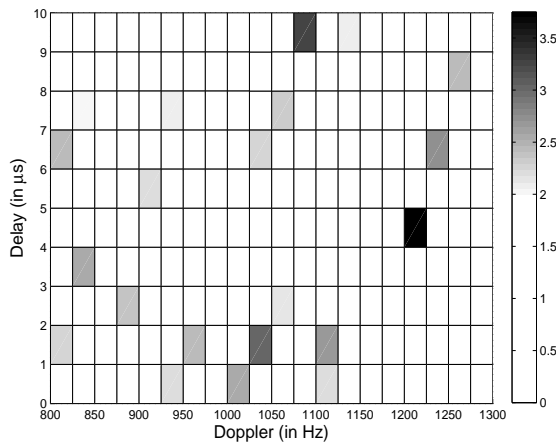


Figure 6.10: Target estimates using BMP at an SNR of -21 dB while employing adaptive amplitude design.

In Fig. 6.9, we plot the reconstructed estimates while using constant modulus waveform at an SNR of -21 dB. Note that we plotted on a 2-D plane and used the color map to represent the intensity for better understanding of these results. The darker the intensity, the higher the reconstruction energy corresponding to that grid point. We observe that constant modulus waveform fails to estimate the locations of all the targets correctly. More specifically, the target that has a Doppler of 1200Hz is wrongly estimated. However, at the same SNR, we observe from Fig. 6.10 that the adaptive amplitude design manages to distribute the highest reconstruction energy among the three actual targets. The three grid points that have the highest intensity

correspond to the three targets. Therefore, this example clearly demonstrates the motivation for employing the adaptive design scheme.

6.9.4 Compressive Sensing

We employ compressive sensing to observe the performance of the system while using far fewer samples when compared with the Nyquist rate. In Fig. 6.11, we plot the reconstructed vector at an SNR of 2.6574dB when the percentage of compression is only $\delta = 20\%$. We can clearly see a degradation in performance when compared with Fig. 6.5, since a lot of energy in the reconstructed vector is now distributed among the incorrect grid points. However, the three most significant components of the estimated vector still correspond to the true target grid points, thereby leading to exact reconstruction of the delay and Doppler.

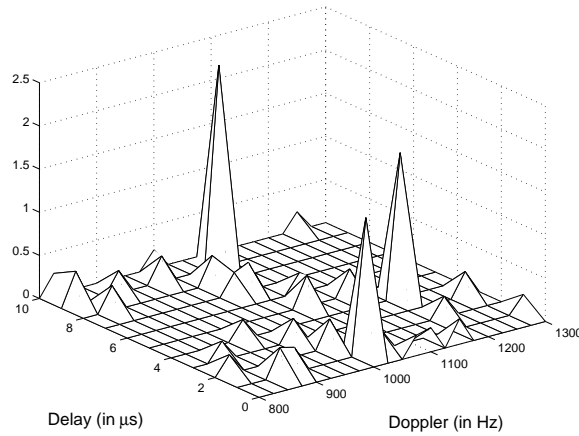


Figure 6.11: Target estimates using BMP at an SNR of 2.6574dB with $\delta = 20\%$.

In Fig. 6.12, we plot the performance metric Δ for different values of SNR while employing different levels of compression. We notice the decline in performance with the increase in the level of compression. However, even at a low SNR of -3.08 dB,

with a $\delta = 10\%$ percentage of compression, the value of the performance metric $\Delta = 1.59$. Since $\Delta > 1$, we can exactly estimate the delay and Doppler of all three targets. However, there will be a reduction in the estimation accuracy of the target RCS values. This reduction shows up in the actual value of Δ in the curves in Fig. 6.12.

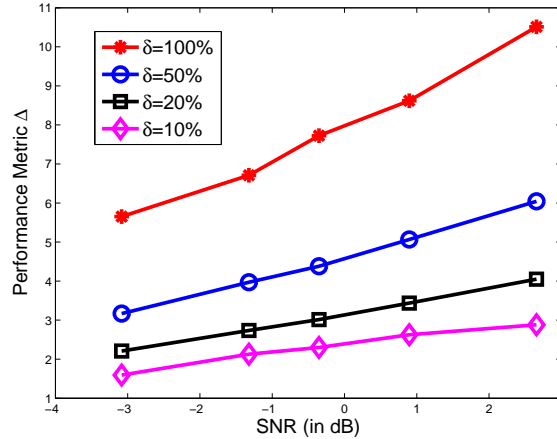


Figure 6.12: Performance metric Δ as a function of SNR for different levels of compression.

As we mentioned earlier, the adaptive amplitude design is applicable even when employing compressive sensing. Therefore, in Fig. 6.13 we show the performance improvement due to the adaptive amplitude design. We notice that even while $\delta = 10\%$, the adaptive design improves the performance.

6.10 Summary

We proposed a sparsity-based colocated MIMO radar system using frequency-hopping waveforms. We estimated the unknown target parameters using sparse support recovery algorithm. We derived an analytical expression for the block coherence measure

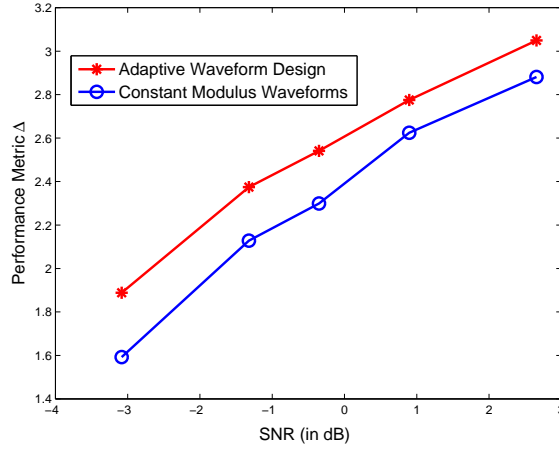


Figure 6.13: Curves demonstrating the improvement in performance due to adaptive amplitude design when $\delta = 10\%$.

of the dictionary matrix and, hence, studied the problem of selecting the hopping frequencies. We presented an iterative algorithm for designing an optimal code matrix. Further, we proposed an approach to optimally design the amplitudes of the transmitted waveforms during each hopping interval using the estimates of the target returns. We demonstrated the performance improvement due to the optimal design using numerical examples. Further, we showed that accurate estimation can be performed from far fewer samples than the Nyquist rate by employing compressive sensing.

In future work, we will consider non-uniform grid spacing to reduce the computational complexity. In addition, we will include the presence of clutter and jammer in the measurement model. We will consider polarized antennas. We will develop more efficient algorithms for solving (6.53) using the theory of combinatorial optimization. We will use multi-objective optimization techniques to jointly solve for the optimal code frequencies and amplitudes. We will incorporate other performance measures like mutual information and entropy into the design problem. We aim to validate our results using real radar data.

Chapter 7

Sparsity-based MIMO Noise Radar for Multiple Target Estimation⁶

7.1 Introduction

In this chapter, we consider colocated MIMO radar with ultra wideband (UWB) noise waveforms from each transmitter, to obtain good resolution during estimation [86]. Noise waveforms are very important in radar applications since they provide a low probability of intercept (LPI) [87]. While using UWB waveforms, the target can no longer be treated as point like because of the enhanced resolution offered by these waveforms. It has a frequency dependent response that cannot be obtained while using conventional narrowband waveforms. Noise waveforms have a flat frequency spectrum, and may not always provide the best match to the target response. Further, even though different transmitters emit independent noise sequences, the cross correlation between them is small but not exactly zero even for zero-lag. We will overcome these problems by covering the noise waveforms by codes that are inspired

⁶Based on S. Gogineni and A. Nehorai, “Sparsity-based MIMO noise radar for multiple target estimation,” *Proc. 7th IEEE Sensor Array and Multichannel Signal Processing Workshop*, Jun. 2012. ©[2012] IEEE.

from code division multiple access (CDMA) [88], [89]. Since these codes have a non-flat frequency response, target responses vary for different codes. Therefore, we will completely exploit the code diversity by selecting waveforms that match the target responses. Further, we will allocate different orthogonal codes for each transmitter to ensure zero cross correlation at zero-lag (see also [90]).

7.2 Signal Model

We assume the radar operates in monostatic configuration. Let M_T and M_R denote the number of transmitters and receivers, respectively. These antennas are arranged in colocated arrays with inter-element spacings given by d_T and d_R , respectively. We assume the targets are located in the far-field. Let the antenna arrays make an angle θ with the group of targets (see Fig. 7.1). Since the targets are far away from the radar arrays, the angular separation between them with respect to the arrays will be negligible. Therefore, we chose the same angle θ for all the targets.

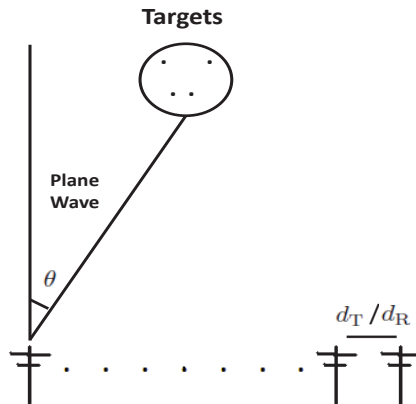


Figure 7.1: Transmit/Receive antenna array used in monostatic configuration.

First, we shall present the measurement model for a single target and later extend it to multiple targets. Let the i^{th} transmitter emit the noise waveform $u_i(t)$ covered by

the code $w_i(t)$. We construct these waveforms and codes as

$$u_i(t) = \sum_{c=0}^{C-1} u_{i,c} \text{rec}(t - c\Delta t), \quad (7.1)$$

and

$$w_i(t) = \sum_{c=0}^{C-1} w_{i,c} \text{rec}(t - c\Delta t), \quad (7.2)$$

where

$$\text{rec}(t) = \begin{cases} 1, & \text{if } 0 < t < \Delta t, \\ 0, & \text{otherwise.} \end{cases} \quad (7.3)$$

Δt denotes the chip interval.

All the covering waveforms are mutually orthogonal [88]. Historically, Walsh functions have been used as covering waveforms in IS-95 systems [91]. In this chapter, we will use Walsh functions of order 64. We express the i^{th} transmitted waveform as $s_i(t) = u_i(t)w_i(t)$. These waveforms travel in space and reflect off the surface of the target before reaching the receive array. In this process, the waveform is attenuated and delay-Doppler shifted. These signals can resolve the paths emanating from different scattering centers of the target. Let there be a total of C' scattering centers with $a_{c'}$ being the attenuation corresponding to the c'^{th} scattering center. We assume C' is known.

The received signal at each receiver is a linear combination of the target-reflected waveforms from all the transmitters. Therefore, the demodulated received signal at the k^{th} receiver can be expressed as [45]

$$\begin{aligned}
y_k(t) &\approx \sum_{i=1}^{M_T} \sum_{c'=0}^{C'-1} a_{c'} \sqrt{1 + \frac{\nu}{f_c}} s_i \left(\left(1 + \frac{\nu}{f_c}\right) (t - \tau - c' \Delta t) \right) \\
&\times e^{j2\pi\nu t} e^{j2\pi\left(1 + \frac{\nu}{f_c}\right) f(\gamma i + k)} + e_k(t),
\end{aligned}$$

where τ and ν denote the delay and Doppler shift, respectively. $e_k(t)$ denotes the additive noise at the k^{th} receiver. f_c is the carrier frequency and

$$f = \frac{d_R \sin(\theta)}{\lambda}, \quad (7.4)$$

$$\gamma = \frac{d_T}{d_R}, \quad (7.5)$$

where $\lambda = \frac{v}{f_c + \nu}$, v is the speed of wave propagation in the medium.

So far, we assumed a single target. Now, consider R targets in the scene illuminated by the radar. Let τ^r , ν^r , and $a_{c'}^r$ denote the delay, Doppler, and attenuations corresponding to the r^{th} target, respectively. After sampling, we can express the measurements as

$$\begin{aligned}
y_k(n) &\approx \sum_{i=1}^{M_T} \sum_{c'=0}^{C'-1} \sum_{r=1}^R a_{c'}^r \sqrt{1 + \frac{\nu^r}{f_c}} \\
&\times s_i \left(\left(1 + \frac{\nu^r}{f_c}\right) (nT_S - \tau^r - c' \Delta t) \right) \\
&\times e^{j2\pi\nu^r n} e^{j2\pi\left(1 + \frac{\nu^r}{f_c}\right) f(\gamma i + k)} + e_k(t),
\end{aligned}$$

where T_S denotes the sampling interval.

7.3 Sparse Representation

In this section, we will express the measurement model presented in the previous section using sparse signal representation. We discretize the target delay-Doppler space into V grid points. Only R of them correspond to the actual targets. Let (τ_v, ν_v) represent the delay and Doppler corresponding to the v^{th} grid point. Define

$$\begin{aligned} \psi_{i,k,c'}(n, v) &= \sqrt{1 + \frac{\nu_v}{f_c}} s_i \left(\left(1 + \frac{\nu_v}{f_c}\right) (nT_s - \tau_v - c'\Delta t) \right) \\ &\times e^{j2\pi\nu_v t} e^{j2\pi\left(1 + \frac{\nu_v}{f_c}\right)f(\gamma i + k)}. \end{aligned}$$

Let there be N samples in a processing interval. Then, we stack $\{\psi_{i,k,c'}(n, v)\}_{n=1}^N$ into a column vector $\boldsymbol{\psi}_{i,k,c'}(v)$. Next, we arrange $\{\boldsymbol{\psi}_{i,k,c'}(v)\}_{k=1}^{M_R}$ into a longer column vector $\boldsymbol{\psi}_{i,c'}(v)$. Each of these columns forms a basis function in our sparse representation. We stack these columns corresponding to different transmitters and paths into a block of columns $\boldsymbol{\Psi}(v)$. Each block corresponds to a different grid point. We have V such blocks that we can concatenate to obtain the dictionary matrix $\boldsymbol{\Psi}$.

Now, we arrange the attenuations $a_{c'}^r$ corresponding to different paths into a C' dimensional vector $\mathbf{a}''^r = [a_0^r, \dots, a_{C'-1}^r]^T$. Since \mathbf{a}''^r is independent of the transmitter index, we define a $M_T C'$ dimensional vector $\mathbf{a}^r = [\mathbf{a}''^{rT}, \dots, \mathbf{a}''^{rT}]^T$. Further, we define a sparse vector $\mathbf{a}(v)$

$$\mathbf{a}(v) = \begin{cases} \mathbf{a}^r, & \text{if } (\tau_v, \nu_v) = (\tau^r, \nu^r), \\ \mathbf{0}, & \text{otherwise.} \end{cases} \quad (7.6)$$

Arranging the vectors $\mathbf{a}(v)$ corresponding to all the grid points, we obtain a $VM_{\text{T}}C'$ dimensional block-sparse vector

$$\mathbf{a} = \left[\mathbf{a}(1)^T, \dots, \mathbf{a}(V)^T \right]^T. \quad (7.7)$$

Stack the measurements and the noise samples at each receiver, we obtain

$$\mathbf{y}_k = [y_k(1), \dots, y_k(N)]^T, \quad (7.8)$$

$$\mathbf{e}_k = [e_k(1), \dots, e_k(N)]^T. \quad (7.9)$$

Additionally, we arrange

$$\mathbf{y} = [\mathbf{y}_1^T, \dots, \mathbf{y}_{M_{\text{R}}}^T]^T, \quad (7.10)$$

$$\mathbf{e} = [\mathbf{e}_1^T, \dots, \mathbf{e}_{M_{\text{R}}}^T]^T. \quad (7.11)$$

Therefore, the measurement model

$$\mathbf{y} = \Psi \mathbf{a} + \mathbf{e}. \quad (7.12)$$

7.4 Sparse Reconstruction

We observed from the previous section that the non-zero entries of the sparse vector appear in blocks. Therefore, we will exploit the block-sparsity while recovering the sparse vector \mathbf{a} . More specifically, we will use the block orthogonal matching pursuit (BOMP) algorithm for sparse recovery [75]. We initialize the residual vector $\mathbf{r}^{(0)} = \mathbf{y}$

and the estimate vector $\mathbf{a}^{(0)} = \mathbf{0}$. In each subsequent iteration, we project the residual from the previous iteration onto all the blocks of columns of $\mathbf{\Psi}$ and pick the block that gives the largest projection energy. Let $v^{(k')}$ be the block selected in the k'^{th} iteration. Further, define $\mathcal{V}^{(k')}$ as the set containing the indices of all the blocks selected in the previous iterations.

We update the corresponding entries of the estimate vector by solving

$$\operatorname{argmin}_{\{\mathbf{a}(v)\}_{v \in \mathcal{V}^{(k')}}} \|\mathbf{y} - \sum_{v \in \mathcal{V}^{(k')}} \mathbf{\Psi}(v) \mathbf{a}(v)\|. \quad (7.13)$$

Denote $\mathbf{a}^{(k')}$ as the updated estimate vector. Next, we update the residue as

$$\mathbf{r}^{(k')} = \mathbf{y} - \sum_{v \in \mathcal{V}^{(k')}} \mathbf{\Psi} \mathbf{a}^{(k')}(v). \quad (7.14)$$

Assume that we terminate the algorithm after K' iterations. Therefore, $\mathbf{a}^{(K')}$ denotes the final estimate of the sparse vector \mathbf{a} containing information about the unknown target parameters.

7.5 Numerical Simulations

We consider an x-band radar system with carrier frequency of 10GHz. Further, we assume the signal bandwidth to be 2GHz. Therefore, the chip interval $\Delta t = 0.5\text{nS}$. Let the number of chips in a pulse $C = 6400$. We consider illumination of the target scene using a single pulse. We simulate a radar system consisting of 3 transmit antennas and 3 receive antennas. Choose $\theta = 30^\circ$ and $d_T = d_R = \frac{\lambda}{2}$. Further, assume there are 3 targets in the illuminated area. Considering $C' = 3$, we define the

attenuations corresponding to the targets $\mathbf{a}'^1 = [0.5, 0.2, 0.8]^T$, $\mathbf{a}'^2 = [0.3, 0.6, 0.7]^T$, and $\mathbf{a}'^3 = [0.2, 0.4, 0.1]^T$.

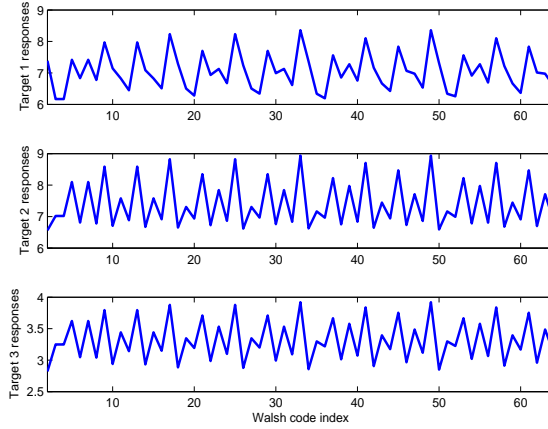


Figure 7.2: ℓ_2 norms of the target returns as a function of the Walsh code index.

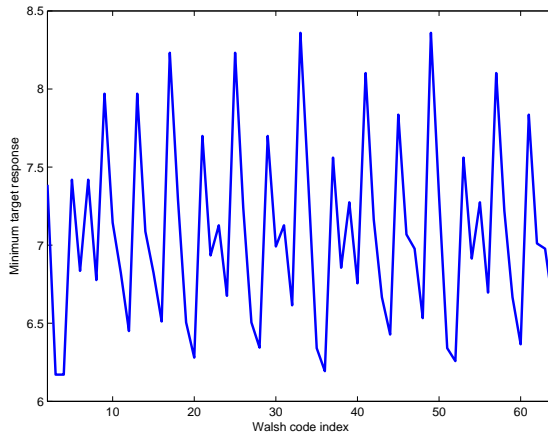


Figure 7.3: ℓ_2 norm of the minimum target returns as a function of the Walsh code index.

As mentioned earlier, we generate Walsh codes of the order 64. Assuming we have accurate estimates of the attenuations from the previous processing intervals, we will select the Walsh codes for the current iteration. We compute the ℓ_2 norm of the signals reflected from the targets. In Fig. 7.2, we plot these norms as a function of the Walsh code indices. We notice that the signal returns are highly dependent on the choice

of Walsh codes. Therefore, we need to match the codes to the target responses in order to improve the system performance. Since, we have multiple targets, the codes giving the optimal response for one target need not provide the optimal response for the other targets. Therefore, we select the code that maximizes the minimum target returns. We plot the minimum target returns in Fig. 7.3. Note here that the weakest target is not fixed a priori. It varies depending on the choice of the code. We observe that the codes with indices 33, 49, and 17 are best matched to the target responses. We assign these codes to the three transmit antennas respectively.

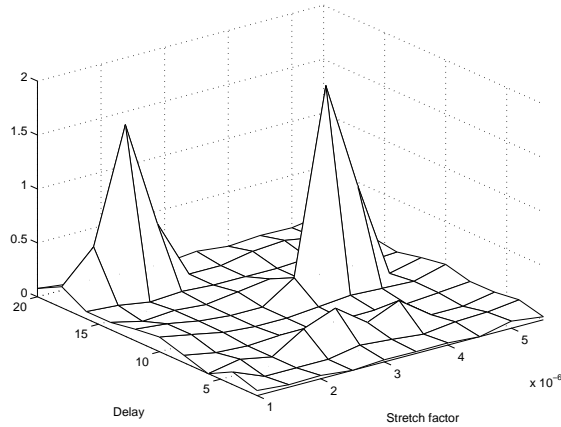


Figure 7.4: Reconstructed sparse vector using optimal Walsh codes.

We discretize the target delay-Doppler space. Assume the true target delays lie in the interval $[2\text{nS}, 20\text{nS}]$. The spacing between these grid points is 2nS . Further, assume that the stretch factor $\left(\frac{\nu_D}{f_c}\right)$ (due to the Doppler) lies in the interval $[0.000001, 0.0000055]$. Let the delays corresponding to the three targets be 12nS , 18nS , and 6nS respectively. Similarly, let the corresponding stretch factors be 0.000004 , 0.000002 , and 0.000003 respectively. In Fig. 7.4, we plot the reconstructed vector at an SNR of -19.8983dB . We can clearly observe that the parameters of the three targets

have been accurately reconstructed. The three largest peaks correspond to the three targets.

7.6 Summary

We used a colocated MIMO noise radar system to solve the multiple target estimation problem. We covered the transmitted noise waveforms using Walsh codes to ensure orthogonality between different transmitters and to match the transmitted waveforms to the target responses. We developed a signal model using sparse signal representation. We used a sparse reconstruction algorithm to estimate the target parameters. We used numerical simulations to demonstrate the performance of the proposed system.

In future work, we will analyze the performance in the presence of jamming signals. We will investigate the robustness of the system to modeling errors. Further, we will validate our results using real radar data.

Chapter 8

Conclusions

8.1 Summary

In this dissertation, we developed and analyzed signal processing algorithms to detect, estimate, and track targets using distributed and colocated MIMO radar systems.

We proposed a radar system that combines the advantages of MIMO radar with distributed antennas and polarimetric radar at the same time. After designing the optimal Neyman-Pearson detector for this system, we analyzed the performance of this detector and designed the optimal transmit polarizations to obtain significant improvement in detection performance. We demonstrated this improvement using numerical simulations. Further, we also addressed the same problem using a game theoretic approach, formulating it in the form of a two player zero-sum game played between an opponent and the radar design engineer. Unlike conventional methods, this approach makes use of the knowledge of the goal of the target and does not require estimation from the training data.

We presented a distributed MIMO radar system capable of monopulse processing at the receivers, developed a tracking algorithm for this system, and simulated a realistic scenario to analyze the performance of the proposed system. We demonstrated the advantages offered by this system over conventional single antenna monopulse tracking radar. We also showed that the proposed system keeps track of a rapidly maneuvering airborne target, even in the presence of an intentional jamming signal. We demonstrated that the monopulse MIMO tracker follows a maneuvering ground target that changes its directions at sharp angles.

We developed a novel approach to estimate the positions and velocities of multiple moving targets using MIMO radar systems with widely separated antennas by employing sparse modeling and compressive sensing. After proposing a new metric to analyze the performance of these systems, we then developed an adaptive optimal energy allocation mechanism to get significant improvement in performance. We used numerical simulations to demonstrate this improvement. We demonstrated that by employing compressive sensing, we can accurately reconstruct the target properties from very few samples. Finally, we showed that the proposed system is robust to modeling errors that may arise due to the discretization of the target state space.

We proposed a sparsity-based colocated MIMO radar system using frequency-hopping waveforms. We estimated the unknown target parameters using sparse support recovery algorithm. We derived an analytical expression for the block coherence measure of the dictionary matrix and, hence, studied the problem of selecting the hopping frequencies. We presented an iterative algorithm for designing an optimal code matrix. Further, we proposed an approach to optimally design the amplitudes of the transmitted waveforms during each hopping interval using the estimates of the target returns.

We demonstrated the performance improvement due to the optimal design using numerical examples. Further, we showed that accurate estimation can be performed from far fewer samples than the Nyquist rate by employing compressive sensing.

Finally, we used a colocated MIMO noise radar system to solve the multiple target estimation problem. We covered the transmitted noise waveforms using Walsh codes to ensure orthogonality between different transmitters and to match the transmitted waveforms to the target responses. We developed a signal model using sparse signal representation. We used a sparse reconstruction algorithm to estimate the target parameters. We used numerical simulations to demonstrate the performance of the proposed system.

8.2 Future Work

In our future work, we will include the effect of clutter in our measurement models. We will extend our game theoretic radar design approach to other problems, including selection of optimal waveform shapes for colocated MIMO radar and optimal radar scheduling. We will extend our analysis to continuous-strategy games. Next, we will perform an asymptotic error analysis and develop performance bounds for the proposed monopulse MIMO tracking algorithm.

We will extend our results on sparsity-based MIMO radar to the case of extended targets. Further, we will model the grid mismatch error using scaled von Mises distribution and analyze the estimation performance. Uniform distribution is a special case of von Mises distribution. Von Mises distribution is commonly used for modeling phase errors in radar problems since the phase is bounded between $[-\pi, \pi]$. Since the

grid error is bounded by half the grid size, scaled von Mises distribution fits this problem well. Additionally, we will consider non-uniform grid spacing to reduce the computational complexity.

Using the theory of combinatorial optimization, we will develop more efficient algorithms for solving the optimal frequency-hopping code selection problem. Then, we will use multi-objective optimization techniques to jointly solve for the optimal code frequencies and amplitudes. We aim to validate our analytical results in this dissertation using real radar data.

References

- [1] J. Li and P. Stoica, *MIMO radar signal processing*. Hoboken, NJ: John Wiley & Sons, Inc., 2009.
- [2] A. M. Haimovich, R. S. Blum, and L. J. Cimini, “MIMO radar with widely separated antennas,” *IEEE Signal Process. Mag.*, vol. 25, pp. 116–129, Jan. 2008.
- [3] J. Li and P. Stoica, “MIMO radar with colocated antennas,” *IEEE Signal Process. Mag.*, vol. 24, pp. 106–114, Sep. 2007.
- [4] J. Li, P. Stoica, L. Xu, and W. Roberts, “On parameter identifiability of MIMO radar,” *IEEE Signal Process. Lett.*, vol. 14, pp. 968–971, Dec. 2007.
- [5] W. M. Boerner, W. L. Yan, A. Q. Xi, and Y. Yamaguchi, “On the basic principles of radar polarimetry: The target characteristic polarization state theory of Kennaugh, Huynen’s polarization fork concept, and its extension to the partially polarized case,” *Proc. IEEE*, vol. 79, pp. 1538–1550, Oct. 1991.
- [6] D. Giuli, “Polarization diversity in radars,” *Proc. IEEE*, vol. 74, pp. 245–269, Feb. 1986.
- [7] M. Hurtado, J. J. Xiao, and A. Nehorai, “Target estimation, detection, and tracking: A look at adaptive polarimetric design,” *IEEE Signal Process. Mag.*, vol. 26, pp. 42–52, Jan. 2009.
- [8] D. Pastina, P. Lombardo, and T. Bucciarelli, “Adaptive polarimetric target detection with coherent radar. i. Detection against Gaussian background,” *IEEE Trans. Aerosp. and Electron. Syst.*, vol. 37, pp. 1194–1206, Oct. 2001.
- [9] P. Lombardo, D. Pastina, and T. Bucciarelli, “Adaptive polarimetric target detection with coherent radar. ii. Detection against non-Gaussian background,” *IEEE Trans. Aerosp. and Electron. Syst.*, vol. 37, pp. 1207–1220, Oct. 2001.
- [10] J. Wang and A. Nehorai, “Adaptive polarimetry design for a target in compound-Gaussian clutter,” in *Proc. Int. Waveform Diversity and Design (WDD) Conf.*, Lihue, Hawaii, Jan. 2006.
- [11] L. M. Novak, M. B. Sechtin, and M. J. Cardullo, “Studies of target detection algorithms that use polarimetric radar data,” *IEEE Trans. Aerosp. and Electron. Syst.*, vol. AES-25, pp. 150–165, Mar. 1989.

- [12] A. R. Calderbank, S. D. Howard, W. Moran, A. Pezeshki, and M. Zoltowski, "Instantaneous radar polarimetry with multiple dually-polarized antennas," in *Fortieth Asilomar Conference on Signals, Systems and Computers*, Pacific Grove, CA, Oct. 2006.
- [13] S. Gogineni and A. Nehorai, "Polarimetric MIMO radar with distributed antennas for target detection," *IEEE Trans. Signal Process.*, vol. 58, pp. 1689–1697, Mar. 2010.
- [14] —, "Polarimetric MIMO radar with distributed antennas for target detection," in *Proc. 43rd Asilomar Conf. Signals, Syst. Comput.*, Pacific Grove, CA, Nov. 2009, pp. 1144–1148.
- [15] J.-J. Xiao and A. Nehorai, "Joint transmitter and receiver polarization optimization for scattering estimation in clutter," *IEEE Trans. Signal Process.*, vol. 57, pp. 4142–4147, Oct. 2009.
- [16] R. Touzi, W. M. Boerner, J. S. Lee, and E. Lueneburg, "A review of polarimetry in the context of synthetic aperture radar: Concepts and information extraction," *Can. J. Remote Sensing*, vol. 30, no. 3, pp. 380–407, 2004.
- [17] M. Hurtado and A. Nehorai, "Polarimetric detection of targets in heavy inhomogeneous clutter," *IEEE Trans. Signal Process.*, vol. 56, pp. 1349–1361, Apr. 2008.
- [18] J. A. Gubner, *Probability and Random Processes for Electrical and Computer Engineers*. New York: Cambridge University Press, 2006.
- [19] L. L. Scharf, *Statistical Signal Processing: Detection, Estimation, and Time Series Analysis*. Addison-Wesley Publishing Company, Inc, 1991.
- [20] E. J. Kelly, "An adaptive detection algorithm," *IEEE Trans. Aerosp. and Electron. Syst.*, vol. 22, pp. 115–127, Mar. 1986.
- [21] S. R. Searle, *Linear Models*. John Wiley & Sons, Inc., 1971.
- [22] A. H. Feiveson and F. C. Delaney, "The distribution and properties of a weighted sum of Chi squares," *NASA Technical Note*, May 1968.
- [23] S. M. Kay, *Fundamentals of Statistical Signal Processing: Detection Theory*. New Jersey: Prentice-Hall, Inc., 1998.
- [24] S. Gogineni and A. Nehorai, "Polarimetric MIMO radar target detection using game theory," in *Proc. 4th IEEE Intl. Workshop on Computational Advances in Multi-Sensor Adaptive Processing (CAMSAP)*, San Juan, Puerto Rico, Dec. 2011, pp. 17–20.

- [25] —, “Game theoretic approach for polarimetric MIMO radar waveform design,” in *Proc. 6th Int. Waveform Diversity and Design (WDD) Conf.*, Kauai, Hawaii, Jan. 2012, pp. 59–62.
- [26] —, “Game theoretic design for polarimetric MIMO radar target detection,” *Signal Processing*, to appear in.
- [27] D. Fudenberg and J. Tirole, *Game theory*. Cambridge, Massachusetts: The MIT Press, 1991.
- [28] D. Blackwell and M. A. Girshick, *Theory of games and statistical decisions*. New York, NY: John Wiley & Sons, Inc., 1954.
- [29] J. F. Nash, “Equilibrium points in n-person games,” *Proceedings of the National Academy of Sciences of the United States of America*, vol. 36, pp. 48–49, Jan. 1950.
- [30] J. V. Neumann and O. Morgenstern, *The theory of games and economic behaviour*. Princeton: Princeton University Press, 1947.
- [31] X. Chen and X. Deng, “Settling the complexity of two-player Nash equilibrium,” in *Proc. 47th Annual IEEE Symposium on Foundations of Computer Science*, Berkeley, CA, Oct. 2006, pp. 261–272.
- [32] L. Khachian, “A polynomial algorithm in linear programming,” *Soviet Math. Dokl.*, vol. 20, pp. 191–194, 1979.
- [33] R. D. McKelvey, A. M. McLennan, and T. L. Turocy. Gambit: Software Tools for Game Theory, Version 0.2010.09.01. [Online]. Available: <http://www.gambit-project.org>
- [34] M. Skolnik, *Radar handbook*. McGraw Hill Companies, 2008.
- [35] D. R. Rhodes, *Introduction to Monopulse*. New York: McGraw-Hill Book Co., 1959.
- [36] S. M. Sherman, *Monopulse principles and techniques*. Dedham, MA: Artech House, Inc., 1985.
- [37] S. Gogineni and A. Nehorai, “Monopulse MIMO radar for target tracking,” *IEEE Trans. Aerosp. and Electron. Syst.*, vol. 47, pp. 755–768, Jan. 2011.
- [38] —, “Target tracking using monopulse MIMO radar with distributed antennas,” in *Proc. 2010 IEEE Int. Radar Conf.*, Washington, DC, May 2010, pp. 194–199.
- [39] P. Swerling, “Probability of detection for fluctuating targets,” *IRE Trans. Inf. Theory*, vol. 2, pp. 269–308, Apr. 1960.

- [40] F. Mcnolty and E. Hansen, "Some aspects of Swerling models for fluctuating radar cross section," *IEEE Trans. Aerosp. and Electron. Syst.*, vol. 10, pp. 281–285, Mar. 1974.
- [41] D. A. Shnidman, "Expanded Swerling target models," *IEEE Trans. Aerosp. and Electron. Syst.*, vol. 39, pp. 1059–1069, Jul. 2003.
- [42] E. J. Kelly, "The radar measurement of range, velocity and acceleration," *IRE Trans. on Military Electronics*, vol. 5, pp. 51–57, Apr. 1961.
- [43] E. J. Kelly and R. P. Wishner, "Matched-filter theory for high-velocity accelerating targets," *IEEE Trans. Mil. Electron.*, vol. 9, pp. 56–69, Jan. 1965.
- [44] A. Rihaczek, "Radar resolution of moving targets," *IEEE Trans. Inf. Theory*, vol. 13, pp. 51–56, Jan. 1967.
- [45] ———, "Delay-Doppler ambiguity functions for wideband signals," *IEEE Trans. Aerosp. and Electron. Syst.*, vol. 3, pp. 705–711, Jul. 1967.
- [46] J. Capon, "High-resolution frequency-wavenumber spectrum analysis," *Proc. IEEE*, vol. 57, pp. 1408–1418, Aug. 1969.
- [47] H. Krim and M. Viberg, "Two decades of array signal processing research," *IEEE Signal Process. Mag.*, vol. 13, pp. 67–94, Jul. 1996.
- [48] M. Hawkes and A. Nehorai, "Wideband source localization using a distributed acoustic vector-sensor array," *IEEE Trans. Signal Process.*, vol. 5, pp. 1479–1491, Jun. 2003.
- [49] G. Mao, B. Fidan, and B. Anderson, "Wireless sensor network localization techniques," *Computer Networks*, vol. 51, pp. 2529–2553, Jul. 2007.
- [50] I. Kanter, "Varieties of average monopulse responses to multiple targets," *IEEE Trans. Aerosp. and Electron. Syst.*, vol. 17, p. 25, Jan. 1981.
- [51] J. M. Howell, "Tracking performance of a monopulse radar in the presence of multiple targets," *IEEE Trans. Aerosp. and Electron. Syst.*, vol. 17, p. 718, Sep. 1970.
- [52] W. D. Blair and M. Brandt-Pearce, "Monopulse DOA estimation of two unresolved rayleigh targets," *IEEE Trans. Aerosp. and Electron. Syst.*, vol. 37, pp. 452–469, Apr. 2001.
- [53] X. Zhang, P. K. Willett, and Y. Bar-Shalom, "Monopulse radar detection and localization of multiple unresolved targets via joint bin processing," *IEEE Trans. Signal Process.*, vol. 53, pp. 1225–1236, Apr. 2005.

- [54] I. E. Kliger and C. F. Olenberger, "Multiple target effects on monopulse signal processing," *IEEE Trans. Aerosp. and Electron. Syst.*, vol. 11, pp. 795–804, Sep. 1975.
- [55] F. Gini, M. Greco, and A. Farina, "Multiple radar targets estimation by exploiting induced amplitude modulation," *IEEE Trans. Aerosp. and Electron. Syst.*, vol. 39, pp. 1316–1332, Oct. 2003.
- [56] E. J. Candes and M. B. Wakin, "An introduction to compressive sampling," *IEEE Signal Process. Mag.*, vol. 25, pp. 21–30, Mar. 2008.
- [57] D. Donoho, "Compressed sensing," *IEEE Trans. Inf. Theory*, vol. 52, pp. 1289–1306, Apr. 2006.
- [58] E. J. Candes, J. Romberg, and T. Tao, "Robust uncertainty principles: Exact signal reconstruction from highly incomplete frequency information," *IEEE Trans. Inf. Theory*, vol. 52, pp. 489–509, Feb. 2006.
- [59] E. J. Candes and T. Tao, "Near-optimal signal recovery from random projections: Universal encoding strategies?" *IEEE Trans. Inf. Theory*, vol. 52, pp. 5406–5425, Dec. 2006.
- [60] J. Trzasko, C. Haider, and A. Manduca, "Practical nonconvex compressive sensing reconstruction of highly-accelerated 3D parallel MR angiograms," in *IEEE International Symposium on Biomedical Imaging: From Nano to Micro*, Boston, MA, Jun. 2009, pp. 274–277.
- [61] R. Chartrand, "Fast algorithms for nonconvex compressive sensing: MRI reconstruction from very few data," in *IEEE International Symposium on Biomedical Imaging: From Nano to Micro*, Boston, MA, Jun. 2009, pp. 262–265.
- [62] R. Baraniuk and P. Steeghs, "Compressive radar imaging," in *IEEE Radar Conference*, Boston, MA, Apr. 2007, pp. 128–133.
- [63] M. Herman and T. Strohmer, "Compressed sensing radar," in *IEEE Radar Conference*, Rome, May 2008, pp. 1–6.
- [64] C.-Y. Chen and P. P. Vaidyanathan, "Compressed sensing in MIMO radar," in *42nd Asilomar Conference on Signals, Systems and Computers*, Pacific Grove, CA, Oct. 2008, pp. 41–44.
- [65] Y. Yao, A. P. Petropulu, and H. V. Poor, "Compressive sensing for MIMO radar," in *IEEE International Conference on Acoustics, Speech and Signal Processing*, Taipei, Apr. 2009, pp. 3017–3020.

- [66] Y. Yu, A. P. Petropulu, and H. V. Poor, “MIMO radar using compressive sampling,” *IEEE Jour. of Selected Topics in Signal Proc.*, vol. 4, pp. 146–163, Feb. 2010.
- [67] S. Gogineni and A. Nehorai, “Target estimation using sparse modeling for distributed MIMO radar,” *IEEE Trans. Signal Process.*, vol. 59, pp. 5315–5325, Nov. 2011.
- [68] —, “Target estimation using compressive sensing for distributed MIMO radar,” in *Proc. 44th Asilomar Conf. Signals, Syst. Comput.*, Pacific Grove, CA, Nov. 2010, pp. 793–797.
- [69] —, “Adaptive design for distributed MIMO radar using sparse modeling,” in *Proc. Int. Waveform Diversity and Design (WDD) Conf.*, Niagara Falls, Canada, Aug. 2010, pp. 23–27.
- [70] M. Akcakaya, M. Hurtado, and A. Nehorai, “MIMO radar detection of targets in compound-gaussian clutter,” in *Proc. 42nd Asilomar Conf. Signals, Syst. Comput.*, Pacific Grove, CA, Oct. 2008, pp. 208–212.
- [71] M. I. Skolnik, *Introduction to Radar Systems*. New York, NY: McGraw-Hill, 2001.
- [72] H. Godrich, V. M. Chiriach, A. M. Haimovich, and R. S. Blum, “Target tracking in MIMO radar systems: Techniques and performance analysis,” in *IEEE Radar Conference*, Washington, DC, May 2010, pp. 1111–1116.
- [73] S. S. Chen, D. L. Donoho, and M. A. Saunders, “Atomic decomposition by basis pursuit,” *SIAM Review*, vol. 43, pp. 129–159, Mar. 2001.
- [74] S. G. Mallat and Z. Zhang, “Matching pursuits with time-frequency dictionaries,” *IEEE Trans. Signal Process.*, vol. 41, pp. 3397–3415, Dec. 1993.
- [75] Y. C. Eldar, P. Kuppinger, and H. Bolcskei, “Block-sparse signals: Uncertainty relations and efficient recovery,” *IEEE Trans. Signal Process.*, vol. 58, pp. 3042–3054, Jun. 2010.
- [76] M. Grant and S. Boyd. (2009, Jun.) CVX: Matlab software for disciplined convex programming (web page and software). [Online]. Available: <http://stanford.edu/~boyd/cvx>
- [77] —. (2008) Graph implementations for nonsmooth convex programs, recent advances in learning and control (a tribute to M. Vidyasagar), V. Blondel, S. Boyd, and H. Kimura, editors, pages 95-110, lecture notes in control and information sciences, Springer. [Online]. Available: http://stanford.edu/~boyd/graph_dcp.html

- [78] M. Akcakaya and A. Nehorai, “MIMO radar detection and adaptive design under a phase synchronization mismatch,” *IEEE Trans. Signal Process.*, vol. 58, pp. 4994–5005, Oct. 2010.
- [79] S. Gogineni and A. Nehorai, “Frequency-hopping code design for MIMO radar estimation using sparse modeling,” *IEEE Trans. Signal Process.*, to appear in.
- [80] —, “Adaptive waveform design for colocated MIMO radar using sparse modeling,” in *Proc. 4th IEEE Intl. Workshop on Computational Advances in Multi-Sensor Adaptive Processing (CAMSAP)*, San Juan, Puerto Rico, Dec. 2011, pp. 13–16.
- [81] —, “Frequency-hopping code design for colocated MIMO radar using sparse modeling,” in *Proc. 6th Int. Waveform Diversity and Design (WDD) Conf.*, Kauai, Hawaii, Jan. 2012, pp. 54–58.
- [82] C. Y. Chen and P. P. Vaidyanathan, “MIMO radar ambiguity properties and optimization using frequency-hopping waveforms,” *IEEE Trans. Signal Process.*, vol. 56, pp. 5926–5936, Dec. 2008.
- [83] S. Sen and A. Nehorai, “Adaptive design of OFDM signal with improved wide-band ambiguity function,” *IEEE Trans. Signal Process.*, vol. 58, pp. 928–933, Feb. 2010.
- [84] —, “Sparsity-based multi-target tracking using OFDM radar,” *IEEE Trans. Signal Process.*, vol. 59, pp. 1902–1906, Apr. 2011.
- [85] R. A. Horn and C. R. Johnson, *Matrix Analysis*. Cambridge University Press, 1985.
- [86] R. M. Narayanan, Y. Xu, P. D. Hoffmeyer, and J. O. Curtis, “Design, performance, and applications of a coherent ultra-wideband random noise radar,” *Opt. Eng.*, vol. 37, pp. 1855–1869, 1998.
- [87] L. Turner, “The evolution of featureless waveforms for LPI communications,” in *Proc. IEEE NAECON*, Dayton, OH, May 1991, pp. 1325–1331.
- [88] J. S. Lee and L. E. Miller, *CDMA Systems Engineering Handbook*. Artech House Publishers Mobile Communications Series, 1998.
- [89] A. J. Viterbi, *CDMA: Principles of Spread Spectrum Communication*. Addison-Wesley Wireless Communications Series, 1995.
- [90] S. Gogineni and A. Nehorai, “Sparsity-based MIMO noise radar for multiple target estimation,” in *Proc. 7th IEEE Sensor Array and Multichannel Signal Processing Workshop*, Hoboken, NJ, Jun. 2012.

- [91] “Mobile station-base station compatibility standard for dual-mode wideband spread spectrum cellular system,” *TIA/EIA Interim Standard 95 (IS-95) (amended as IS-95A in May 1995)*, Washington: Telecommunications Industry Association, July 1993.

Vita

Sandeep Gogineni

- Date of Birth** August 14, 1985
- Place of Birth** Hyderabad, India
- Degrees** Ph.D., Electrical Engineering,
Washington University in St. Louis, MO, USA, 2012
M.S., Electrical Engineering,
Washington University in St. Louis, MO, USA, 2009
B.Tech. (Hons), Electronics & Communications Engineering,
International Institute of Information Technology, Hyderabad,
India, 2007
- Affiliations** Student member of IEEE Signal Processing Society
- Awards** Best paper award (first prize) in the student paper competition at the *2012 Int. Waveform Diversity and Design (WDD) Conf.*
- Finalist in the student paper competition at the *2010 Int. Waveform Diversity and Design (WDD) Conf.*, the *2011 IEEE Digital Signal Processing and Signal Processing Education Workshop*, and the *2012 Int. Waveform Diversity and Design (WDD) Conf.*
- Publications** S. Gogineni and A. Nehorai, “Frequency-hopping code design for MIMO radar estimation using sparse modeling,” to appear in *IEEE Trans. on Signal Processing*.
- S. Gogineni and A. Nehorai, “Game theoretic design for polarimetric MIMO radar target detection,” to appear in *Signal Processing*, vol. 92, no. 5, pp. 1281-1289, May 2012.
- S. Gogineni and A. Nehorai, “Target estimation using sparse modeling for distributed MIMO radar,” *IEEE Trans. on Signal Processing*, vol. 59, no. 11, pp. 5315–5325, Nov. 2011.

- S. Gogineni and A. Nehorai, "Compressed LED illumination sensing," *IEEE Signal Processing Letters*, vol. 18, no. 10, pp. 5315–5325, Oct. 2011.
- S. Gogineni and A. Nehorai, "Monopulse MIMO radar for target tracking," *IEEE Trans. on Aerospace and Electronic Systems*, vol. 47, no. 1, pp. 755–768, Jan. 2011.
- S. Gogineni and A. Nehorai, "Polarimetric MIMO radar with distributed antennas for target detection," *IEEE Trans. on Signal Processing*, vol. 58, no. 3, pp. 1689–1697, Mar. 2010.
- M. Hurtado and S. Gogineni and A. Nehorai, "Adaptive polarization design for target detection and tracking," *Waveform Design and Diversity for Advanced Radar Systems*, (Ch. 16, F. Gini, A. De Maio, and L. Patton, Eds.), IET, to appear.
- S. Gogineni and A. Nehorai, "Sparsity-based MIMO noise radar for multiple target estimation," *Proc. 7th IEEE Sensor Array and Multichannel Signal Processing Workshop*, Jun. 2012.
- S. Gogineni and A. Nehorai, "Frequency-hopping code design for colocated MIMO radar using sparse modeling," *Proc. 6th Int. Waveform Diversity and Design (WDD) Conf.*, pp. 54–58, Kauai, Hawaii, USA, Jan. 2012.
- S. Gogineni and A. Nehorai, "Game theoretic approach for polarimetric MIMO radar waveform design," *Proc. 6th Int. Waveform Diversity and Design (WDD) Conf.*, pp. 59–62, Kauai, Hawaii, USA, Jan. 2012.
- S. Gogineni and A. Nehorai, "Adaptive waveform design for colocated MIMO radar using sparse modeling," *Proc. 4th IEEE Intl. Workshop on Computational Advances in Multi-Sensor Adaptive Processing (CAMSAP)*, pp. 13–16, San Juan, Puerto Rico, Dec. 2011.
- S. Gogineni and A. Nehorai, "Polarimetric MIMO radar target detection using game theory," *Proc. 4th IEEE Intl. Workshop on Computational Advances in Multi-Sensor Adaptive Processing (CAMSAP)*, pp. 17–20, San Juan, Puerto Rico, Dec. 2011.

- S. Gogineni and A. Nehorai, "Game theoretic design for polarimetric MIMO radar target detection," *Workshop on Future Trends in Sensor Diversity, Signal Processing, & Exploitation*, Vernon, NY, Apr. 2011.
- S. Gogineni and A. Nehorai, "Illumination sensing using sparse modeling," *Proc. IEEE Digital Signal Processing and Signal Processing Education Workshop*, pp. 255-258, Sedona, AZ, USA, Jan. 2011.
- S. Gogineni and A. Nehorai, "Target estimation using compressive sensing for distributed MIMO radar," *Proc. 44th Asilomar Conf. Signals, Syst. Comput.*, pp. 793-797, Pacific Grove, CA, USA, Nov. 2010.
- S. Gogineni and A. Nehorai, "Adaptive design for distributed MIMO radar using sparse modeling," *Proc. 5th Int. Waveform Diversity and Design (WDD) Conf.*, pp. 23-27, Niagara Falls, Canada, Aug. 2010.
- S. Gogineni and A. Nehorai, "Compressive sensing for MIMO radar with widely separated antennas," *Office of Naval Research Workshop on MIMO Radar and Benchmark*, Santa Barbara, CA, May. 2010.
- S. Gogineni and A. Nehorai, "Target tracking using monopulse MIMO radar with distributed antennas," *Proc. IEEE Int. Radar Conf.*, pp. 194-199, Washington, DC, USA, May. 2010.
- S. Gogineni and A. Nehorai, "Polarimetric MIMO radar with distributed antennas for target detection," *Proc. 43rd Asilomar Conf. Signals, Syst. Comput.*, pp. 1144-1148, Pacific Grove, CA, USA, Nov. 2009.
- S. Gogineni and A. Nehorai, "Polarimetric MIMO radar with distributed antennas for target detection," *Office of Naval Research Workshop on MIMO Radar and Benchmark*, San Diego, CA, Jul. 2009.
- G. Sandeep, C. Ravi Teja, G. Kalyana Krishnan and V. U. Reddy, "Low complexity decoders for combined space time

block coding and V-BLAST,” *Proc. 2007 IEEE Wireless Communications and Networking Conf.*, pp. 583-588, Kowloon, Hong Kong, Mar. 2007.

May 2012

Adaptive MIMO Radar, Gogineni, Ph.D. 2012